Nanocomposites of

Bacterial Nanocellulose and Paramagnetic Iron Oxide Nanoparticles

A Thesis

Presented in Partial Fulfillment of the Requirements for the

Degree of Master of Science

with a

Major in Materials Science and Engineering

in the

College of Graduate Studies

University of Idaho

by

Erin Lynn Cochran

June 2014

Major Professor: D. Eric Aston, Ph.D.

AUTHORIZATION TO SUBMIT THESIS

This thesis of Erin Lynn Cochran, submitted for the degree of Master of Science with a major in Materials Science and Engineering and titled "Nanocomposites of Bacterial Nanocellulose and Paramagnetic Iron Oxide Nanoparticles" has been reviewed in final form. Permission, as indicated by the signatures and dates given below, is now granted to submit final copies to the College of Graduate Studies for approval.

Major Professor   _____ Date _____
         D. Eric Aston

Committee
Members   _____ Date _____
         Peter Griffiths

    _____ Date _____
         Andrzej Paszczynski

    _____ Date _____
         Mark Roll

Department
Administrator   _____ Date _____
         Wudneh Admassu

Discipline's
College Dean   _____ Date _____
         Larry Stauffer

Final Approval and Acceptance by the College of Graduate Studies

    _____ Date _____
         Jie Chen

ABSTRACT

Nanocomposites of bacterial cellulose (BC) nanofibers and paramagnetic iron oxide nanoparticles—magnetite/maghemite (Fe_3O_4/γ-Fe_2O_3)—were created, and the materials and interactions were analyzed using Fourier transform infrared spectroscopy with attenuated total reflection (ATR-FTIR), X-ray diffraction, field emission scanning electron microscopy, transmission electron microscopy, dynamic light scattering, and energy-dispersive X-ray spectrometry.

To engineer the composites' composition, structure, and morphology, BC was combined with Fe_3O_4/γ-Fe_2O_3 nanoparticles of various types and concentrations by two methods: (1) the culture medium of *Gluconacetobacter hansenii* was augmented with Fe_3O_4/γ-Fe_2O_3 nanoparticles, which aggregated, and cellulose biosynthesis was endeavored—in some cases BC production was hindered due to *Gluconacetobacter* mutation into non-producers or iron oxide toxicity; (2) purified BC was used as a nanofiber matrix on which Fe_3O_4/γ-Fe_2O_3 nanoparticles were deposited by co-precipitation synthesis—both reverse co-precipitation and NH_3 gas-enhanced co-precipitation.

In method (1), Fe_3O_4/γ-Fe_2O_3 nanoparticles were physically entangled in the BC nanofibers, with no evidence of hydrogen bonding. In method (2), nanoparticles were coated on the nanofibers, resulting in homogeneous dispersions. ATR-FTIR revealed hydroxyl band broadening indicative of increased hydrogen bonding, which implied the surface hydroxyl groups of the iron oxide nanoparticles synthesized in the BC nanofiber matrix interacted with the hydroxyl groups located along the cellulose molecule. Reverse co-precipitation of Fe_3O_4/γ-Fe_2O_3 nanoparticles on the BC nanofibers was the best method for creating nanocomposites of bacterial cellulose nanofibers and paramagnetic iron oxide nanoparticles.

ACKNOWLEDGMENTS

TABLE OF CONTENTS

LIST OF FIGURES

LIST OF TABLES

1. INTRODUCTION

1.1 Bacterial Cellulose Materials: Properties, Structure, and Applications

1.1.1 Properties and Structure of Bacterial Cellulose Compared with Plant Cellulose

Cellulose is the most ubiquitous polymeric material in the world, and is used for the production of papers, textiles, composite and construction materials, food and drug additives, films, plastics, adhesives, binders, biofuels such as ethanol, and many other applications. Indeed, cellulose has a significant impact on the environment and the economy. Cellulose is produced by a variety of organisms, ranging from vascular plants to algae and prokaryotic organisms such as bacteria.[1] Cellulose derived from plants, known as plant cellulose (PC), is the most utilized source of cellulose. However, the cultivation of plants for cellulose entails extensive use of arable land, fertilizers, and pesticides as well as the consumption of fresh water for irrigation. Therefore, other sources of cellulose are being investigated; in particular, non-plant producers of cellulose such as some bacteria species. The bacteria genus *Gluconacetobacter* is the most prolific producer of cellulose and therefore the most researched. The cellulose generated by *Gluconacetobacter* is commonly referred to as bacterial cellulose (BC), and it is a promising alternative to PC.

Comprehensive research has revealed that BC is chemically pure cellulose, and has a high degree of polymerization, high crystallinity, high mechanical strength, high surface area, high holding capacity for materials, and the ability to be shaped and modified during synthesis.[2-5] In addition, BC is non-toxic, biocompatible, biodegradable, and renewable.[6] BC is essentially chemically identical to purified PC; however, the structure and properties of BC and PC differ. BC is pure cellulose exuded as nanofibers from the *Gluconacetobacter* cell wall into the form of a 3D fiber network whereas PC exists in a complex morphology with other co-synthesized molecules such as lignin, hemicelluloses, pectin, waxes, and proteins which must be removed to obtain pure cellulose.[2,7-10] The purification process of PC is expensive and environmentally unfriendly. For example, paper manufacture from wood cellulose involves logging, debarking, chipping, screening, mechanical and/or chemical pulping, and bleaching to obtain partially purified PC.[5,11,12]

The properties of BC fibers and composites vary depending on the culture conditions; for example, the growth media constituents and treatment, as well as the treatment of the material after growth. The properties of PC fibers depend on factors such as plant type, location, climate, soil, maturity at harvest, extraction methods, and processing of the fibers.[13,14]

BC fibers, which range in width from nanometers to micrometers, are formed from stacked nanofibers composed of chains of cellulose molecules held together with inter- and intra-chain hydrogen bonding, creating a semicrystalline structure. BC fibers have a finer structure than PC fibers; the latter must be broken down mechanically and chemically, as needed, to extract nanofibers.

The chain length of cellulose is expressed as the number of its constituent anhydroglucose units (AGU); this is also the value of the degree of polymerization (DP) which varies with the source and treatment of the cellulose material. BC has a high DP—often higher than most plant celluloses. The DP of BC usually ranges from 2,000-10,000 but can be as low as around 800 or as high as 20,000 depending on the *Gluconacetobacter* strain and the culture conditions, whereas the DP of PC varies depending on the type of PC and the treatment: 150-300 for microcrystalline cellulose derived from PC, 300-1700 for wood pulp, and 800-10,000 for cotton and other plants.[1,3,7,15-17]

The numerous hydroxyl functional groups (-OH) of BC, located at interchain and intrachain regions of the cellulose molecules and between the nanofibers, work cooperatively to resist force and dissipate energy, forming hydrogen bonds. The result is a strong material, both as a single fiber and as a sheet of fibers. Hydrogen bonding enables cellulosic materials like BC to have high mechanical strength, and to be nearly as strong as steel yet lightweight, even though the hydrogen bonds are 100 to 1,000 times weaker than the bonds in metals and ceramics.[18]

BC fibers have excellent mechanical properties when generated under standard culture conditions.[2] PC fibers have a heterogeneous structure and composition, as well as voids due to the lumen; therefore, PC fibers have variable mechanical properties.[8,19,20] The treatments of BC and PC affect the mechanical properties. Cellulose I, the crystalline cellulose form of both PC and BC fibers, has an elastic modulus of 128-134 GPa, and a tensile strength estimated around 10 GPa.[21,22] The mechanical properties of BC are similar to those of crystalline Cellulose I. BC fibers have an elastic modulus in the range of 78-114 GPa depending on the width, or diameter. [3,23-25] Single BC fibers with diameters ranging from 35 to 90 nm were found to have an elastic modulus up to 95 GPa.[24] The naturally occurring pellicle material composed of a 3D network of BC fibers was found to have an elastic modulus up to around 18 GPa across the plane of the sheet and a tensile strength up to 260 MPa. [26] PC fibers have varying mechanical properties due to the plant source, treatment, and size of the fiber. Researchers found the modulus of PC fibers to range from 39 GPa for fibers around 35 micrometers in diameter to 78 GPa for fibers about 5 micrometers in diameter, and surmise that this variation is related to the difference in the size of the lumen (the void inside the fiber).[13] For

example, single flax fibers were found to have an average modulus of 54 GPa and typical wood fibers have a modulus of around 10-13 GPa; furthermore, fibers separated from wood by a chemical pulping process were found to have a modulus up to 40 GPa, and when subdivided into even smaller fibers, a modulus of around 70 GPa was achieved.[13,27]

Indeed, extracted PC nanofibers have better mechanical properties than the original PC fiber. Such PC nanofibers were found to have an elastic modulus ranging from 120 to 270 GPa and a tensile strength in the 1-6 GPa range.[8,27-32] Other researchers found that a PC nanocellulose spun fiber had a modulus of 22.5 GPa and a tensile strength of 275 MPa.[33] Sheets of fibrillated nanocellulose from wood pulp have an elastic modulus up to 15 GPa and a tensile strength up to 240 MPa.[30] A nanocellulose paper has a modulus of about 14 GPa and a tensile strength of about 214 MPa.[34] Microcrystalline cellulose derived from PC has an elastic modulus of 25 GPa, and nanocomposite films from microcrystalline cellulose have an elastic modulus of 13 GPa and a tensile strength up to 240 MPa depending on the composition.[19,35]

Researchers who fabricated heat-pressed paper from both BC pulp and cotton pulp found an elastic modulus and tensile strength of 5 GPa and 85 MPa for BC and 0.085 MPa and 0.83 MPa for cotton.[36] BC composites with transparent thermosetting resins had an elastic modulus of around 20-28 GPa, and tensile strengths reaching 325 MPa [37,38] whereas wood nanofiber composites showed an elastic modulus of about 13-16 GPa and tensile strength of about 216-280 MPa.[30] Fibrillated wood pulp composites have an elastic modulus around 19 GPa, and random-oriented PC fiber-reinforced composites have an elastic modulus of 1-13 GPa and a tensile strength of 15-140 MPa.[19,38] All-cellulose composites from filter paper showed an elastic modulus of 8.2 GPa and a tensile strength of 211 MPa, whereas other types of all-cellulose composites including those from BC showed an elastic modulus of 28 GPa and a tensile strength of 910 MPa.[39]

Because of its unique structure, BC has higher crystallinity and higher hydrophilicity than most PC.[40] The crystallinity of BC has been found to range between 53-90% depending on culture conditions, treatment, and XRD method used whereas the crystallinity of PC was found to be in the 37-63% range depending on the source, treatment, and XRD method used.[3,7,41,42] Other researchers found BC and cotton linters to be similar in crystallinity, around 63%, whereas softwoods, paper pulp, and other PC fibers such as Ramie had lower crystallinity, between the range 42-55%.[43]

BC fibers have a high aspect ratio and a very high surface area per unit mass, and combined with its high hydrophilicity, BC has a very high water holding capacity.[5,44] The surface area of BC is greater than PC. Researchers found that it was more than 200 times greater than the surface area of

cellulose fibers isolated from softwoods.[45] BC is highly absorbent, and has a water holding capacity ranging around 100-150 times its dry weight.[5,46]

The properties of BC as well as the physical and chemical structure can be engineered and tuned at the nano-, micro-, and macroscales by modifying the culture medium and the fiber surface by physical and chemical methods.[38,47] The size and shape of BC materials can also be engineered. A planar sheet of intertwined BC fibers is formed naturally by *Gluconacetobacter* and can be engineered into nearly any shape, size, and thickness.[5,13] In order to engineer BC into nearly any form, BC biosynthesis can be directed to cause oriented epitaxial deposition by using templates with designed molecular surfaces; such novel methodologies can be used to innovate BC materials with desired forms and functions.[4,48-50] The abundance of researched and developed BC-based materials and devices places this versatile material on the forefront of applied science.

1.1.2 Applications of Bacterial Cellulose Materials

The properties and structure of BC including a high surface area and nanoscale network of fibers, high material holding capacity, high hydrophilicity, high crystallinity, high mechanical strength, and high degree of polymerization enable a variety of product applications.[2] BC's properties and nanoscale structure is particularly useful for engineering composite materials. BC can be used as both a matrix and a reinforcement material.

The porous structure of intertwined BC nanofibers enables incorporation of many different kinds of materials for the creation of novel composites with a wide range of applications, from biomedicine, to remediation of ground and waste water, to electronics.[51-56]

Currently, BC is consumed worldwide as food products such as nata de coco and nata de pina.[5,57-60] BC nanofibers have been used as a reinforcing material for optically transparent composite materials.[37,61,62] BC has also been utilized for specialty membranes and filters and applied in the pulp, paper, and mining industries.[55,63-65] Various products composed of BC are commercially available, for example the biomedical products Dermafill[TM], Nanoskin®, and Celmat®, and the suspension and thickening product Cellulon®.[66-69]

BC is researched and developed for biomedical applications because of its biocompatibility, biodegradability, and unique properties and structure.[51,70-72] Furthermore, BC exhibits more favorable properties than PC for biomedical applications.[73,74] Biomedical products require materials of high quality which are generally expensive; therefore, BC products made from high-cost ingredients are economically viable for biomedical applications. BC materials can be applied in a wide range of biomedical technologies: for implants, stents, and grafts in skin, bone, dental, vascular,

and other body tissues, for a scaffold or substrate for tissue engineering and reconstruction, for wound dressings, medical pads, supersorbers, skin healing, and for drug delivery technologies.[70,75-95]

1.1.3 Composites of Bacterial Cellulose and Iron Oxide: Properties and Applications

Other materials can be incorporated with BC for the engineering of novel composites. For example, multifunctional and magnetically-responsive composite materials can be created from BC and paramagnetic iron oxide NPs: BC provides a strong and flexible structure, and iron oxide NPs provide magnetic and adsorbant properties, and both materials can be coated with other substances or linked to molecules to achieve a wide range of properties and applications.[96,97] Both BC fibers and iron oxide NPs have large surface areas which enables the attachment of molecules that functionalize the materials.[98-100] Various molecules have been used to functionalize composites of BC fibers and iron oxides; for example, chemicals that act as biological agents or catalysts.[56,97,98]

Magnetic NPs have several features which are useful for engineering composites. An important characteristic of paramagnetic iron oxides such as magnetite (Fe_3O_4) and γ-maghemite (Fe_2O_3) is magnetic susceptibility which imparts mobility to a composite material composed of these iron oxides; that is, the ability to be manipulated by an external magnetic field gradient.[101] Magnetite is the most favorable iron oxide NP for making composite materials as it exhibits the strongest magnetism of the transition metal oxides as well as the highest magnetization of the iron oxides—higher than both maghemite and hematite.[102]

Another important aspect of iron oxides is their high adsorption capacity due to Fe–OH groups at the surface, which enables them to form surface complexes with a range of cations, especially heavy metal-hydroxy cations (MOH^+), and oxyanions; for example, toxic chemicals and heavy metals.[103-105] Iron oxide NPs have excellent reduction capabilities and high reactivity with a broad spectrum of toxic substances, thus they are widely used for remediation.[106] Bacterial cellulose and iron oxide composite is both porous and adsorbent which makes it especially useful for applications such as toxic heavy metal removal from water.[56,101,107]

Both cellulose and iron oxides are biocompatible; therefore, a composite of these materials is particularly suitable for biomedical applications.[6,108] Composites employing cellulose and paramagnetic iron oxide have potential application in drug delivery, filtration, catalysis, enzyme immobilization, electromagnetic shielding, microfluidics, actuator, information storage, security, anti-counterfeiting, and remediation (especially ground- and wastewater treatment) technologies.[56,109-114]

1.2 Bacterial Cellulose from *Gluconacetobacter*

1.2.1 Background of Bacterial Cellulose from Gluconacetobacter

Several types of bacteria produce cellulose, a beta-glucan polysaccharide, in metabolic processes. The most prolific bacterial producers of cellulose are members of the genus *Gluconacetobacter.* The taxonomy for the *Gluconacetobacter* genus and species has changed several times in the past, and continues to be adjusted; for example, *Gluconacetobacter* was formerly classified as *Acetobacter* because many species of this genus produce acetic acid, and many species of *Gluconacetobacter* have been named and renamed. *Gluconacetobacter* species reported in research include *G. xylinus, G. hansenii, G. sucrofermentans, G. europaeus, G. oboediens*, *G. intermedius, G. nataicola, G. persimmonis*, and *G. entani,* just to name a few.[115-119] The most prolific cellulose producers include both *Gluconacetobacter hansenii* (previously known as *Acetobacter hansenii*, *Acetobacter xylinus*, and as a strain of *Gluconacetobacter xylinum*), for example, the common laboratory strains ATCC® 23769™ (isolated from vinegar and beer) and ATCC® 53582™ (isolated from sugarcane exudate), and *Gluconacetobacter sucrofermentans*, also known as *Gluconacetobacter xylinus* (or *Acetobacter xylinum) subsp. sucrofermentans*, which was isolated from cherries.[118,120-122]

Gluconacetobacter is a gram-negative, aerobic, rod-shaped bacterium naturally found in the flesh and juice of fruits, vegetables, and other plants especially those high in saccharides such as sugarcane, as well as in liquids such as vinegar and alcoholic beverages containing saccharides that the bacteria consume as a carbon source and transform into the polysaccharide cellulose.[120,123,124]

Synthesis of the exopolysaccharide by *Gluconacetobacter* was first reported in 1886 by Brown.[2,125] Research on bacterial cellulose biosynthesis using *Gluconacetobacter* as a model bacterium began in the 1940s when Hestrin and Schramm proved that *Gluconacetobacter* synthesized cellulose in the presence of glucose and oxygen; furthermore, they developed the inoculation medium known as the Hestrin-Schramm (HS) medium which is the basis of most culture mediums used for BC production, albeit often modified with additives such as buffers to affect pH or other substances to achieve desired outcomes and to create novel BC-based materials.[126-131] According to experimental studies on BC production, the optimal culture conditions for maximum BC production for most *Gluconacetobacter* species is a temperature between 28 and 30°C, and pH range from 3.5 to 6.0.[123,129,132] In addition, *Gluconacetobacter* produces cellulose most prolifically under static (stationary) culture conditions, in other words, BC yield is greater in stationary rather than

agitated cultures for many reasons. However, the topic of yield and optimization of BC production and procedures goes beyond the scope of this research.

Only a few *Gluconacetobacter* species and strains have been found to withstand the cell mutation that occurs under agitated culture conditions and which results in reduced BC production; therefore, these strains are used in agitated bioreactors, including *Gluconacetobacter hansenii* ATCC® 53582[TM] which may produce rounded masses of BC, also referred to as spheroids, under agitation.[133] *Gluconacetobacter hansenii* ATCC® 23769[TM] was utilized in this research.

Gluconacetobacter produces cellulose fibers in the form of an interwoven matrix. Under static liquid culture medium conditions, *Gluconacetobacter* species produce a cellulose sheet or mat, known as a pellicle, at the air-liquid interface. The BC pellicle is known colloquially as a "mother" or "mushroom", or as "vinegar plant," and is often mistaken as the cause of the production of vinegar and fermented beverages such as kombucha; however, it is the *Gluconacetobacter* in the culture medium and inside the pellicle that are responsible for consuming saccharides and producing cellulose and other substances such as acetic acid.

1.2.2 Cellulose Function for Gluconacetobacter

Most bacteria synthesize extracellular polysaccharides, long carbohydrate molecules of repeated monomer units joined together by glycosidic bonds, which form envelopes or environments such as biofilms around the cells.[134] The morphology and properties of BC enable several functions. The cellulose matrix of interwoven nanofibers allows water-borne nutrients to be supplied easily by diffusion to the *Gluconacetobacter* cells inside the matrix, thus enabling high cell concentrations, propagating the population which moves toward the nutrient source and continues to secrete cellulose.[1,134,135] The cellulose matrix naturally floats on the surface the nutrient medium, but it can also be suspended inside; BC can also adhere to advantageous surfaces near nutrient sources.[76,136] The cellulose matrix also provides a protective habitat against unfavorable environmental changes such as decreases in water and nutrient content, variations in pH, UV radiation, and appearances of toxic substances and pathogenic organisms.[25,55,135,137,138] BC can also become a nutrient source when regular nutrients are depleted, for cellulose decomposition is catalyzed by exo- and endoglucanases, which have been detected in the culture media of some *Gluconacetobacter* strains.[139]

1.2.3 Bacterial Cellulose Production

The two methods to synthesize BC are a stationary (static) culture, which results in a mat or pellicle formation at the air-liquid interface near the media surface, and an agitated culture in which cellulose is synthesized under the media surface in the form of stringy, stellate, irregular and spherical fibrous masses.[3,16] Under certain agitated culture conditions, some *Gluconacetobacter* strains form isolated spherical masses, which are called granules or pellets.[133] Most strains produce higher yields of cellulose in static cultures, whereas agitated cultures result in lower yields due to many factors, such as strain instability—the bacteria mutates into non-cellulose producing strains, which may be caused by non-Newtonian behavior of media during mixing or improper oxygen supply.[10,17,55,137,140,141] Despite these problems and lower BC yields, many researchers believe that agitated and aerated cultivation is more applicable for economical large-scale industrial production of BC than static cultivation.[17,142-144]

To scale-up BC production, some researchers have employed stirred-tank reactors with high agitation or other reactors such as the internal-loop airlift reactor with success which indicates that the problems associated with agitated culture conditions are a result of the type or method of agitation.[143,145-149] Most researchers endeavoring to produce BC under agitated conditions have used the rotary horizontal shakers which are ubiquitous in their laboratories yet problematic for BC production. The system mechanics (including the fluid mechanics) of the rotary shaker method for producing of BC are often either overlooked or not understood.[150] In this study, rotary shakers were used to endeavor to produce BC and BC composites in agitated experiments without previous knowledge of the effects of system mechanics on BC production; however, a better understanding of the problematic method of rotary shaker bioreactors was gained.

Researchers have worked to maximize the yield of BC through experimental design, including nutritional, genetic, and technological bioprocess improvements in order to achieve the economical, efficient production of BC on the industrial scale; however, BC production generally is not cost effective due to the high cost of culture growth materials, with the exception of production for biomedical applications.[10,17,141,151,152] Another approach is to use low-cost feedstocks and to make BC production a "green" technology involving reduction, reuse, and recycling by generating BC from agricultural and industrial by-products and waste streams such as effluents and residuals.[153-156] While waste streams can be utilized, the conventional method of BC production still requires a feedstock.

Recent advancements may enable BC production on an industrial scale. Researchers successfully transferred *Gluconacetobacter xylinus* cellulose synthase genes into the cyanobacterium

Synechococcus leopoliensis and subsequently produced BC without a feedstock from sunlight, water, and the genetically engineered autotrophic cyanobacterium; currently, however, this type of cellulose production has low yield and needs improvement in order to become economically viable.[157,158] A mass-manufacturing method to produce cellulose via an organism which produces cellulose by creating its own food source would be vastly more efficient and more environmentally friendly than methods of producing cellulose from PC sources.

1.3 Research Objectives

The goal of this research is to demonstrate that nanocomposites of bacterial cellulose and iron oxide nanoparticles can be engineered, and to examine the interaction of the two materials. In particular, this research examines the chemical bonding that may occur between the BC nanofibers and iron oxide nanoparticles (NPs).To engineer the composition, structure, and morphology of the composites, BC will be combined with iron oxide NPs of various types and concentrations by two methods: First, the culture media of *Gluconacetobacter hansenii* will be augmented with iron oxide NPs and cellulose biosynthesis will occur in incubated static and agitated culture media. Second, BC will be produced and purified BC and used as a nanofiber matrix on which iron oxide nanoparticles will be deposited by co-precipitation synthesis. Engineering of the nanocomposites will be achieved by varying the type or the amount of iron oxide either added to the medium in the first method for the first method, or precipitated on the nanofibers in the BC matrix.

The compositions, structures, and morphologies of the nanocomposites should be diverse depending on the fabrication method, that is, depending on the amount of iron oxide NPs in the growth media and static or agitated treatment, or the concentration of precursor ions in solution available for iron oxide synthesis and precipitation; as a result, the properties of the nanocomposites should vary. To engineer tunable composites, it is important to understand the interactions between iron oxide NPs and BC.

To examine the nanocomposites and the interaction between the BC nanofibers and the iron oxide NPs, several characterization and analysis methods will be used: field-emitting scanning electron microscopy (FESEM) and transmission electron microscopy (TEM) for physical imaging and morphology analysis, dynamic light scattering (DLS) for morphology analysis, and attenuated total reflection Fourier-transform infrared spectroscopy (ATR-FTIR), X-ray diffraction (XRD), and energy dispersive X-ray spectroscopy (EDX) for compositional and molecular interaction analysis.

2. MATERIALS AND METHODS

2.1 Cellulose Standards: Bacterial Cellulose and Microcrystalline Cellulose

The material used as the basis of this research was bacterial cellulose (BC), which was produced in the laboratory. Purified BC was used as a standard to compare with the composites composed of BC and iron oxide NPs. The other cellulosic material used as a standard for comparison to BC was the plant-derived cellulose microcrystalline cellulose (MC); specifically, the commercial MC product Sigmacell 20 (Sigma-Aldrich), which has an average size of 20 μm. Subsequent methodology sections discuss these materials.

2.2 *Gluconacetobacter* Cultures and Culture Medium

2.2.1 Culture Medium Preparation and Gluconacetobacter Propagation

The bacterial cellulose used in this study was prepared from *Gluconacetobacter hansenii* cells located inside BC pellicles received from Dr. Marie Laborie who originally purchased the bacteria from the American Type Culture Collection (ATCC) as *Gluconacetobacter hansenii* strain ATCC® 23769™.[121]

The bacteria in the as-received BC pellicles were sampled and propagated in a modified Hestrin-Schramm (HS) medium composed of 20 grams glucose (ICN Biomedicals Anhydrous D(+)-Glucose, or Dextrose), 5 grams of peptone (Difco Bactopeptone), 5 grams of yeast extract (Becton Dickinson Bacto™ Extract of Autolysed Yeast Cells), 2.75 grams disodium phosphate (Fisher anhydrous dibasic sodium phosphate) and 1.15 grams of citric acid (J.T. Baker anhydrous citric acid powder) in 1 liter deionized (DI) water for an average pH of 6.0.[129] Optimum pH of the culture medium depends on the strain, varying between 4.0 and 7.0 pH. Bielecki, 2005 #26} The medium was autoclaved at 120°C for 20 min.

This culture medium was used for all BC production and was also combined with agar in the process of streaking to isolate the bacteria and for making reference cultures. The solution was magnetically stirred until all components were dissolved, then 75 mL aliquots of this medium were poured into 250 mL Erlenmeyer (conical) flasks capped with foam stoppers and aluminum foil, and then sterilized in an autoclave at 250°F or 121°C for 25 minutes.

Initial propagation of *Gluconacetobacter hansenii* was achieved by transferring one of the as-received pellicles with a sterilized loop into 75 mL of HS medium using aseptic techniques in a

laminar flow hood and incubating at 30°C and for 5 days in a VWR water-jacketed Model 2450 incubator. All procedures involving contact with the bacteria were conducted using aseptic techniques in a laminar flow hood to eliminate contamination.

2.2.2 Preparation of Reference Cultures

Once a homogeneous pellicle had formed at the surface of the medium a test for purity of the bacterial culture was conducted (to confirm that the as-received samples had not been contaminated by other organisms even though the as-received bacteria originated from the *Gluconacetobacter hansenii* strain ATCC® 23769™ cultivated and stored in a laminar flow hood) by sampling the bacteria, sub-culturing by streaking for isolation on media in agar plates, incubating until colonies formed, and then checking the colonies for morphological and cultural characteristics on the agar plate and with optical microscopy.

The test for culture purity was conducted on agar plates made from the culture medium mixed with 2.5 g/100 mL or 1.5 % agar (BD Difco granulated agar). 100mL aliquots of the agar-enriched medium was poured into bottles and autoclaved at 121°C for 25 minutes, cooled to room temperature, and then melted in a microwave and poured into plastic petri dishes (sterilized under 5 minutes of UV light) in the laminar flow hood.

Streaking for isolation, which was conducted in a laminar flow hood, entailed scraping the pellicle with a sterile wire loop and inoculating the agar plate by streaking three times, sterilizing the loop between each streak. The inoculated agar plates were incubated at 30°C and circular colony formations began to appear visible to the human eye three days later. Reference cultures on the agar plates were maintained at 4°C. Colonies on agar plates were examined by optical microscopy and strain purity was confirmed.

2.2.3 Preparation of Gluconacetobacter Culture Stocks and Inoculation Cultures

After strain purity was determined, 1-5 mL aliquots of liquid beneath a pellicle was inoculated into 50-75 mL of HS media in 125 mL Erlenmeyer flasks, or 100 mL in 250 mL flasks, and statically cultivated at 30°C for approximately 7 days until a pellicle had formed at the air-liquid interface. The cellulose pellicle that formed on the surface of the culture broth was removed, blended, and filtered to obtain a cell suspension.

For inoculating growth media, cell suspensions and frozen cell stocks were prepared. All materials and tools used in this process were sterilized in an autoclave for 30 min at 121°C including the stainless steel blender chamber, filter, tweezers, funnel, jar, glycerine solution, and cryovials. For collecting the *Gluconacetobacter* cells via blending and filtering, a buffer solution of potassium

dihydrogen phosphate (KH_2PO_4) of pH 6.0 was made by slowly adding aliquots of dibasic KH_2PO_4 to monobasic KH_2PO_4 under magnetic stirring then sterilized in an autoclave for 25 minutes at 121°C.

The cellulose pellicle was placed in the stainless steel chamber of a Waring commercial blender with tweezers and blended with 25 mL of the buffer solution to remove bacterial cells. The pellicle was blended for 30 second intervals six times and then filtered through a sterilized MiraCloth (EMD Millapore) filter inside a funnel into a 200 mL glass jar. Four 25 mL aliquots totaling 100 mL of buffer were utilized to wash away any remaining material in the blender and were poured into the filter to wash cells into the jar.

This jar was placed in a shaker for 10-15 minutes to suspend bacteria above any BC fragments that might be present. 30 mL aliquots of the cell and buffer solution were pipetted into 50 mL tubes and centrifuged at 8670xg or 7,422 RPM at 4°C for 10 minutes in a Beckman Coulter JS-13.1 Avanti HP-30I centrifuge to pellet the cellulose. The supernatant was removed with a pipette and the bulk of the bacteria pipetted into one centrifuge tube.

This cell suspension was used to create frozen stock cultures as well as to directly inoculate HS media to generate precultivation inoculums. For frozen stock cultures, the emptied tubes were filled with 2 mL aliquots of a 25% glycerol solution and vortexed for 5 seconds and this liquid was pipetted into the tube containing the cells. The glycerol solution was added to the tube for a total glycerol volume of 15 mL. 1 mL aliquots of the mixture were pipetted into cryovials and stored at -80°C as stock cultures for future use.

The cells used as the inoculum for all experiments and for propagating new generations of *Gluconacetobacter hansenii* were precultivated at 30°C for a minimum of one week under static conditions. Fresh or frozen cell suspensions were used to inoculate this precultivation media. The cryotubes containing frozen cell suspensions were thawed at room temperature before use. For precultivation, 1-5 mL aliquots of the stock cell suspension were added to 50-75 mL of HS media in 125 mL Erlenmeyer flasks, or 100 mL HS in 250 mL flasks, and cultivated statically in an incubator at 30°C for approximately 7 days until a pellicle had formed at the air-liquid interface. For use in experiments, after a minimum of 5 days of static incubation, 1-5 mL aliquots of the culture medium were collected under the pellicle to use as the inoculum; this preculture method is commonly used by other researchers.[26,55]

2.3 Iron Oxide Nanoparticles

Three types of iron oxide nanoparticles (IO NPs) were used in this research to fabricate composites with bacterial cellulose. The two types of IO NPs used for experiments inside the growth media along with bacterial cells were obtained from Nano Iron, s.r.o. products: one commercially available as the product STAR, the other a modification of the product Nanofer 25 by a silica-coating procedure, which was conducted at the University of Idaho. The third type of iron oxide NP was synthesized in the laboratory as part of this research. Synthesized iron oxide NPs were produced for two purposes: as part of the composite with BC in which the NPs were synthesized in the BC matrix (which is described in a separate methodology section), and as a freestanding standard with which to compare to the NPs synthesized in BC matrices.

2.3.1 Iron Oxide NPs Derived from Nanofer STAR and Silica-coated Nanofer 25

The two types of iron oxide NPs used in the BC growth media were derived from NanoIron products reported as nanoscale Zero-Valent Iron (nZVI), or Fe^o. One type is the dry nanopowder Nanofer STAR—named after an acronym of its characteristics: "Surface stabilized, Transportable, Air-stable, and Reactive"—which NanoIron reports is composed of a reactive nZVI core with a ~2 nm non-reactive iron oxide shell; specifically, a wüstite (FeO)-magnetite (Fe_3O_4), double shell that provides surface stabilization and slows oxidation in air; Nanofer STAR has a composition by weight of 60-80% nZVI and 20-40% iron oxides.[159,160]   Nanofer STAR was used as the iron oxide NP for experiments in the growth media because for several reasons. Nanofer STAR particles (STAR IO NPs) are coated with an iron oxide shell to reduce their oxidation, allowing in-situ preparation of the suspensions, and Nanofer STAR is an easily transportable powder commercially available in bulk which is advantageous for scaling up production.

The other type of iron oxide NP is a powdered silica-coated iron oxide NP fabricated via a sol-gel coating procedure of NanoIron's Nanofer 25 at the University of Idaho by postgraduate researchers in the lab of Dr. Andrzej Paszczynski.[99,161] The inert silica coating on the surface stabilizes iron oxide NPs, improves chemical stability, reduces aggregation in liquid, and provides better protection against toxicity. The silica coating on the iron oxide NPs enables molecules to be attached for surface functionalization and for incorporation of other substances, either before or after combination with the BC nanofibers; therefore, a variety of other composites with unique forms, functions, and applications can be created.[97]

Nanofer 25 is a slurry product composed initially of 16% (± 2%) Fe^o, 4% (± 2%) magnetite, 0-1% (± 2%) carbon, and 80% (± 2%) water as shown in Table 2.1 derived from NanoIron's Material

Safety Data Sheet (MSDS).[162] NanoIron reports that the Fe^o portion of STAR and Nanofer 25 is extremely reactive and intensively oxidizes, transforming to magnetite in the presence of oxygen in water and air.[159,163,164] This process occurs rapidly at room temperature as depicted in Figure 2.1, adapted and extrapolated from NanoIron's Nanofer 25 data and graphs.[163] NanoIron also reports that the amount of magnetite Fe_3O_4 in the core of the silica-coated Nanofer 25 varies depending on the concentrations at the time of coating, the age of the slurry, and heat treatment.[163]

Table 2.1: Constituents and composition of Nanofer 25 at production outset, from NanoIron's Material Safety Data Sheet.				
Constituents:	Fe^o	Fe_3O_4	C	H_2O
Composition:	14-18%	2-6%	0-1%	80%

Figure 2.1: Concentration versus time plot of Fe^o, or nanoscale Zero-Valent Iron (nZVI), showing decrease of Fe^o concentration in Nanofer 25 over time as oxidation occurs at room temperature, as derived from Nano Iron data and graph, with data extrapolation via trendline.
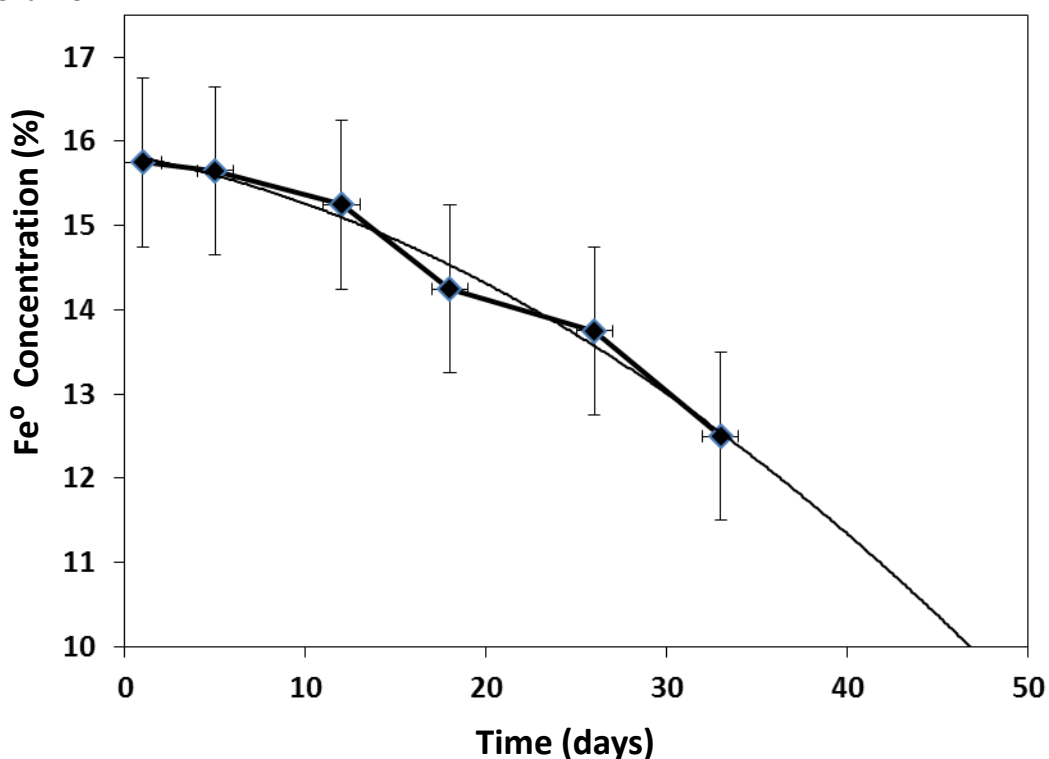
The silica-coated Nanofer 25 was fabricated via a two-step coating process, starting with a sol-gel process to obtain a porous silica coating, followed by a dense-liquid process that hydrolyzed

and closed the residual ethoxy groups in the pores with additional silica. The NPs were cleaned with a series of washes (in ethanol or DI water) with separations by magnetic decantation and then either oven-dried at 110°C for 24 hours, or freeze-dried for at least 8 hours.[99,105]

As a result of heating Nanofer 25 in air during the silica-coating process (which enables oxygen diffusion into the material), Fe^o and magnetite are likely transformed into maghemite because magnetite (Fe_3O_4) oxidizes, transforming into maghemite (γ-Fe_2O_3) over time in the presence of oxygen, even at room temperatures.[102]

X-ray Diffraction (XRD) analysis of the silica-coated Nanofer 25 (SiO_2 IO NPs) and dried Nanofer 25 slurry (without the silica coating) oven-dried at 110°C for 24 hours indicates that both NP samples may be composed of Fe_3O_4 or γ-Fe_2O_3, or both, as shown in Figure 2.2 and Table 2.2. Note that the peak at 37.3° in SiO_2 IO NPs and Nanofer 25 indicates Fe_3O_4. In contrast, the pattern of the STAR displays the diffraction peaks for Fe^o which indicates the material is not oxidized, that is unreacted. Table 2.2 lists the XRD d-spacings (peak values) of the Nanofer 25, SiO_2-coated Nanofer 25, and STAR IO NPs tested and the d-spacings characteristic of Fe_3O_4 and Fe^o reported in the International Centre for Diffraction Data (ICDD) database via EVA software as synthesized magnetite designated as "magnetite, syn" and synthesized iron designated as iron, syn or Fe.

Figure 2.2: XRD diffractograms of silica-coated Nanofer 25 and oven-dried Nanofer 25 with d-spacing peaks of magnetite, and STAR with d-spacings of elemental iron, Fe^o.
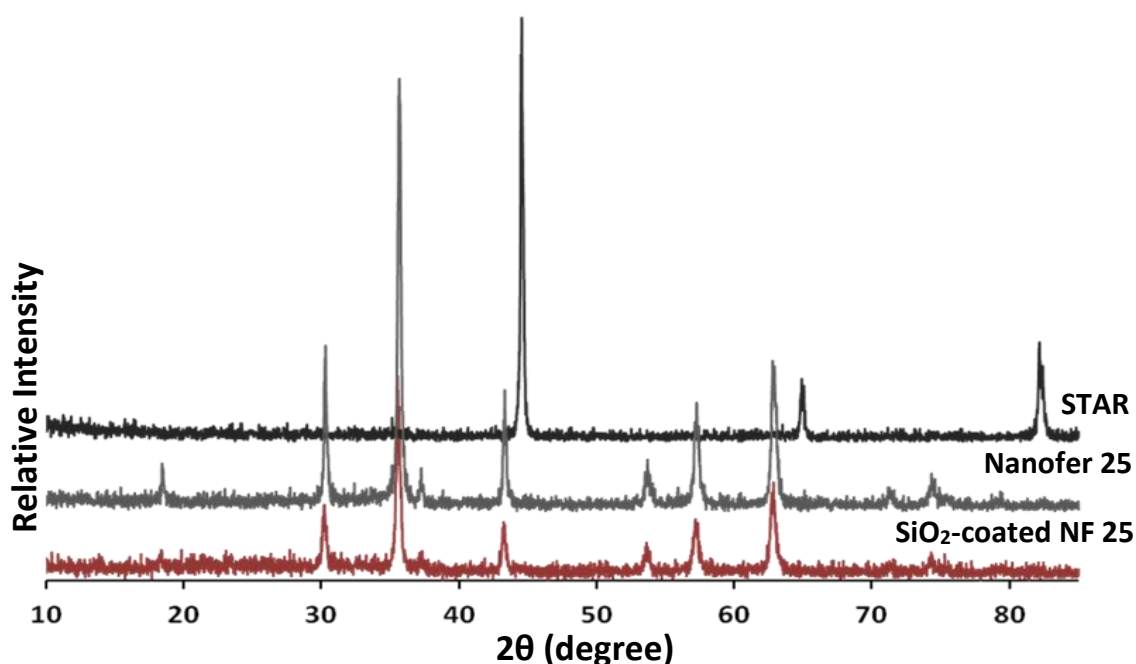
Table 2.2: XRD d-spacings for silica-coated Nanofer 25, Nanofer 25 and STAR and ICDD standards Fe_3O_4, γ-Fe_2O_3 and iron Fe^o. 2θ values for SiO_2 IO NPs or STAR IO NPs at far left.

angle	d-spacing values (in Angstrom, A)					
2θ	SiO_2-coated Nanofer 25	Nanofer 25	Fe_3O_4 ICDD	γ-Fe_2O_3 ICDD	STAR	Fe^o ICDD
18.3	4.85	4.85	4.84	4.84		
30.1	2.97	2.97	2.97	2.95		
35.5	2.53	2.53	2.52	2.51		
43.2	2.09	2.09	2.10	2.09		
37.3	2.40	2.40	2.42			
44.5					2.035	2.024 (2θ=44.7)
57.2	1.61	1.61	1.62	1.61		
62.7	1.48	1.48	1.49	1.40		
64.8					1.437	1.433 (2θ =65)
82.4					1.169	1.169

Nano Iron reports that Nanofer 25 has an average particle size of 50 nm with a size distribution of 20-100 nm.[165] The Nanofer 25 and STAR IO NPs appear to be ~80-200 nm in size according to the electron microscope TEM images of in Figure 2.3. The silica-coated iron oxide nanoparticles (SiO_2 IO NPs) have a silica layer on the Nanofer 25 NPs, which increases their size. The size data of the NPs utilized in this research is discussed in the dynamic light scattering (DLS) results section.

Figure 2.3: Transmission Electron Microscopy images of Nano Iron zero-valent iron oxide products (a) Nanofer 25 composed of 14-18% Fe^o nanoparticles with a Fe_3O_4 shell, and (b) STAR, Fe^o stabilized by a Fe_3O_4 shell. Photographs courtesy of Nano Iron, Inc.
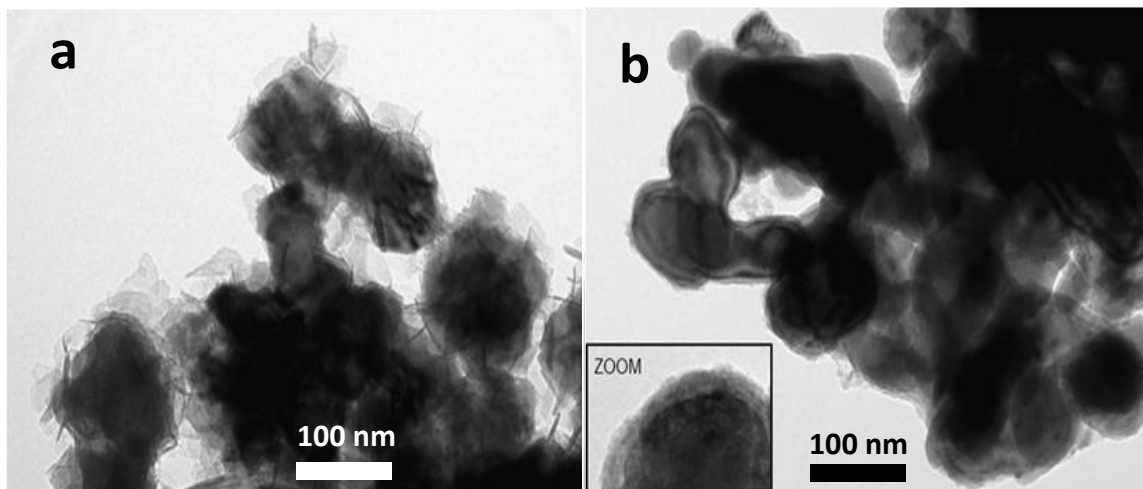
2.3.2 Synthesized Iron Oxide Nanoparticles

The co-precipitation method is widely used to synthesize iron oxide NPs such as magnetite and maghemite NPs as it is simple and economical; in addition, the surface of the NPs produced by this method can be treated easily with other materials for a wide range of applications. There are two types of co-precipitation methods, normal co-precipitation (in which the alkaline solution is added to the iron salt solution, and pH increases gradually to about pH 3 which causes Fe^{3+} ions to precipitate as ferrihydrite, $(Fe^{3+})_2O_3$, which reacts with Fe^{2+} ions to form magnetite), and reverse co-precipitation in which the solution of iron salts is added to the alkaline solution containing either ammonia (NH_3) or sodium hydroxide (NaOH).[166,167] Ammonia is widely used by researchers in co-precipitation methods to facilitate synthesis of magnetite.[168] Ammonia has an advantage over NaOH as a precipitant of iron oxide, for several reasons. Ammonia can be used in room temperature (RT) reactions as either a liquid or a gas whereas NaOH solutions usually require heating and stirring which can cause oxygenation.[102,168-170]

To synthesize magnetite NPs by the co-precipitation method, a solution containing ferrous and ferric salts—such as ferrous sulfate, $FeSO_4$, and ferric sulfate, $Fe_2(SO_4)_3$, or ferrous chloride, $FeCl_2$, and ferric chloride, $FeCl_3$—in specific proportions to achieve a 2:1 molar ratio of ferric (Fe^{3+}) to ferrous (Fe^{2+}) ions, is combined with a concentrated solution of an alkaline reducing agent: either ammonium hydroxide, (as ammonia, NH_3(aq), dissolved in water), or sodium hydroxide (NaOH).[171-174]

In this research, iron oxide NPs were synthesized to verify that magnetite NPs could be fabricated by the co-precipitation method and to create a NP standard with which to compare the composites of BC and iron oxide NPs that were fabricated from the same precursor solutions. Magnetite NPs were synthesized by a reverse co-precipitation method, using aqueous iron salt solutions containing ferric sulfate and ferrous sulfate precursors at a fixed 2:1 molar ratio of Fe^{3+} to Fe^{2+} ions, respectively, which were mixed separately in DI water under continuous stirring at RT, combined, and then reacted with ammonia, NH_3(aq), to precipitate magnetite (Fe_3O_4 or iron (II,III) oxide) according to the chemical reaction (1);[166] with a 2:1 stoichiometric ratio of Fe^{3+} : Fe^{2+}, complete precipitation of Fe_3O_4 is expected at a pH between 8 and 14 in a non-oxidizing oxygen environment; however, Fe_3O_4 is sensitive to oxidation and can transform into maghemite (γ-Fe_2O_3 or gamma phase iron (III) oxide) in the presence of oxygen according to the chemical reaction (2)

$$Fe^{2+} + 2\,Fe^{3+} + 8\,OH^- \rightarrow Fe_3O_4 + 8\,NH_4^+ + 4\,H_2O \qquad (1)$$

$$Fe_3O_4 + 2H^+ \rightarrow Fe_2O_3 + Fe^{2+} + H_2O \qquad (2)$$
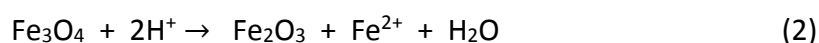
Ferric sulfate, $Fe_2(SO_4)_3$, (JT Baker), and ferrous sulfate, $FeSO_4$, (Fisher) were dissolved separately into DI water in glass beakers under ambient conditions and magnetically stirred until the solid salts dissolved. To enhance dissolution of the solid iron salts, 3 mol/L sulfuric acid H_2SO_4 (95-98% Fisher) was added in 1 μL aliquots for a total amount varied from 1-2000 μL depending on solute concentration and solution amount.

To produce iron oxide NPs, a 0.05 mol/L iron salt solution containing a 2:1 ratio of Fe^{3+} and Fe^{2+} ions was poured into an excess of 28-30% ammonia, $NH_3(aq)$, (Sigma-Aldrich) dissolved in water and mixed by magnetic stirring. The reaction mixture turned black instantaneously as magnetite precipitated. The black magnetite precipitate was magnetically separated with an external magnet, decanted, and washed three times in a process involving sonication in DI water and magnetic decantation to remove non-magnetic, unreacted chemicals. The magnetite NPs were collected by magnetic separation, and subsequently freeze-dried prior to characterization.

2.4 Production of BC and BC-Iron Oxide Nanocomposites in Culture Media

2.4.1 Static and Agitated Culture Conditions for BC and Nanocomposite Production

The main set of experiments for this research involved the production of various BC materials, including pure BC and composites of BC and iron oxide NPs, in 50 mL Erlenmeyer flasks containing 10 mL HS media inoculated with 2 mL aliquots of culture media containing pre-cultured cells, and then incubated under either static or agitated conditions. Static growth experiments were conducted in incubators (VWR and Conviron) at 30°C for a minimum of 7 days. Agitated growth experiments were conducted in a rotary planar shaker (Controlled Environment Incubator Shaker Model G25 or Series 25, New Brunswick Scientific Co. Inc.), also known as an orbital or horizontal shaker, operating at a 160 rpm rotational speed at 30°C for a minimum of 7 days.

Many tests were conducted to develop methods for producing BC and composites of BC and iron oxide NPs before the main experiments were performed. Several generations of *Gluconacetobacter* were propagated under various static and agitated culture conditions in the process of generating BC materials. BC production under static culture conditions was successful; however, production of BC under agitated conditions in rotary shakers proved to be difficult. In the Results and Discussion section, this investigation of static and agitated culture media growth is presented.

2.4.2 Production of Pure BC

Pure BC samples, free of NPs, were also generated as standards for each experiment. were produced and processed for use both as the standards in material characterization for experimental analysis, and as the matrix material for experiments involving the synthesis of iron oxide NPs in the BC matrix, which is described in a subsequent methods section.

2.4.3 Production of Nanocomposites via BC Growth Media Modified with Iron Oxide NPs

Iron oxide NPs in varied concentrations were added to the BC growth media which was inoculated with *Gluconacetobacter* and incubated under both static and agitated conditions in order to determine if nanocomposite production could be achieved by the different methods and materials, and to study the materials' interactions. Experiments using Silica-coated iron oxide NPs (SiO_2 - IO NPs) and STAR IO NPs were conducted for the production of nanocomposites of BC- SiO_2 IO NPs and BC-STAR IO NPs.

SiO_2 - IO NPs and STAR IO NPs in aliquots of 5 mg, 10 mg, 20 mg, and 40 mg were added to 50 mL Erlenmeyer flasks containing 10 mL HS medium and 2mL inoculum from pre-cultures and incubated at 30°C under both static and agitated culture conditions. Production lasted 5 days. Starting one day after inoculation, the BC pellicles in the static experiments and the BC masses in the agitated experiments, along with iron oxide NPs, whether incorporated into the BC matrix or not, were photographed in the culture media each day. After 5 days, the BC-iron oxide composites—the pellicles from the static cultures and masses from the agitated cultures that had developed—were removed, lightly washed with DI water to remove HS media, and photographed. Samples were cleaned by a series of washes involving sonication in DI water, dried, and characterized, as described in subsequent methods sections.

2.5 BC-Iron Oxide Nanocomposites via Synthesis of Iron Oxide NPs in BC Matrix

To fabricate BC-iron oxide nanocomposites by synthesizing iron oxide NPs in the BC nanofiber matrix, two co-precipitation techniques were used: a reverse co-precipitation technique and a gas-enhanced in situ co-precipitation technique. All materials were stored and all experiments were conducted at normal air and RT conditions. In both techniques, BC was treated with ferric/ferrous sulfate solutions containing a 2:1 molar ratio of Fe^{3+} to Fe^{2+} ions prior to reaction with ammonia to precipitate magnetite. The concentrations of the Fe^{3+}/Fe^{2+} solutions were varied to examine the effect of ion concentration on iron oxide NP formation in the BC fiber network. Three different concentrations of Fe^{3+}/Fe^{2+} solutions were used—0.01, 0.1, and 1 mol/L—to affect the

amount of iron oxide deposited in the BC matrices, and mass loading at each concentration was examined.

2.5.1 Reverse co-precipitation of BC-Iron Oxide NP Composites

BC-iron oxide nanocomposites were produced using reverse co-precipitation to synthesize magnetite NPs in the BC matrix. This version of the reverse co-precipitation technique is similar to the one used to synthesize magnetite NPs, with some modifications. Iron oxide NPs were synthesized in BC nanofiber networks, in both whole and ground BC membranes.

To produce BC-iron oxide NP composites, freeze-dried BC membranes were immersed for 24 hours in aqueous ferric/ferrous sulfate solutions so that Fe^{3+} and Fe^{2+} ions could diffuse into the nanofiber matrices. For each sample, after the solution diffused into the BC membrane, the loaded BC matrix was submerged immediately in 28-30% aqueous ammonia to precipitate iron oxide NPs inside the BC nanofiber network. After the reaction, the BC-iron oxide composite samples were washed to remove unattached iron oxide NPs that formed from excess Fe^{3+}/Fe^{2+} solution or that were loosely bound to the BC; samples were placed into DI water and sonicated for 5 minutes for a minimum of 3 sets in which the water was changed with each set, until the water became clear. After washing, the samples were lyophilized for approximately 8 hours. Upon removal from the freeze-dryer, the membranes were immediately weighed to determine the percentage of mass loading depending on the concentration of the Fe^{3+}/Fe^{2+} solution. The membranes exhibited a range of colors depending on the concentrations of Fe^{3+}/Fe^{2+} solutions used, 0.01, 0.1, and 1 mol/L, from yellow-brown to brown.

The reverse co-precipitation method was also used to synthesize iron oxide NPs in nanofiber networks from ground BC membranes to produce BC-iron oxide composites. BC membranes were ground in a shaker ball mill (SPEX 8000M), the material was sifted in a ASTM testing sieve [in a ASTM testing sieve 250 micron mesh [250 µm] U.S.A. Standard sieve ASTM] , and 250 micron mesh samples were collected for the experiments. BC-iron oxide composites were produced, washed, and dried using procedures similar to those used for the BC membranes, with some modifications. The ground BC material was immersed in 15 ml of the Fe^{3+}/Fe^{2+} solution for 24 hours and then centrifuged to remove the supernatant liquid and pellet the loaded BC nanofibers. The samples were submerged immediately in 28-30% aqueous ammonia to precipitate iron oxide NPs inside the networks of short BC nanofibers. A centrifugation step was added after each wash cycle to remove the water. Therefore, unattached iron oxide NPs could not be separated because the samples were centrifuged,

which pelleted both the composites and any freestanding NPs. After washing, the samples were also lyophilized.

The composites of iron oxide NPs synthesized in the BC membranes by the reverse co-precipitation method were characterized with XRD, FESEM, and EDS; in addition, the composites produced from ground BC membranes were characterized by TEM.

2.5.2 Ammonia gas-enhanced in situ co-precipitation of BC-Iron Oxide NP Composites

An ammonia gas-enhanced in situ co-precipitation technique was used for this project because researchers reported that ammonia gas more easily penetrated the porous structure of BC than aqueous NaOH solutions, and resulted in homogeneous dispersions of iron oxide NPs in BC membranes; furthermore, ammonia slightly increased pH which assisted the production of magnetite.[102,169]

BC membranes were freeze-dried and stored under ambient conditions, and then immersed for 12-24 hours in aqueous iron salt solutions containing iron oxide precursor ions Fe^{3+} and Fe^{2+} in a fixed 2:1 molar ratio obtained by combining aqueous solutions of ferric sulfate, $Fe_2(SO_4)_3$, (JT Baker) and ferrous sulfate, $FeSO_4$ (Fisher) which had been dissolved separately in DI water under ambient conditions and magnetically stirred. To enhance dissolution of the solid iron salts, 3M sulfuric acid H_2SO_4 (95-98% Fisher) was added in 1 μL aliquots for a total amount varied from 1-2000 μL depending on solute concentration and solution amount.

Three different concentrations of iron ion precursor solutions were used—0.01, 0.1, and 1 mol/L —to affect the amount of iron oxide deposited in the BC matrices. After immersion, the samples were removed and placed onto a cellulose filter paper (Whatman) on tissues (Kimtech, VWR) to wick away excess solution. A sample enclosed in the reaction chamber was exposed to ammonia gas, which was generated by heating a 28-30% ammonia solution to its boiling point of 36-38°C and pulled through the reaction chamber by a simple vacuum while air was simultaneously bubbled through the ammonia solution as depicted in Figure 2.4.

After the reactions, to remove any loosely bound or excess iron oxide particles, the BC-iron oxide nanocomposites were washed: samples were placed into DI water and sonicated for 5 minutes for a minimum of 3 sets in which the water was changed with each set, for a total of 15 minutes or until the water became clear. After washing, the samples were lyophilized for approximately 8 hours. Upon removal from the freeze-dryer, the samples were immediately weighed to determine the percentage of mass loading depending on the molar concentration of the iron ions precursor solution

and then stored at ambient conditions. The synthesis of iron oxide NPs in the BC matrix was confirmed via characterization with XRD and FESEM.

Figure 2.4: Ammonia gas-enhanced in situ co-precipitation method for synthesizing iron oxide nanoparticles on bacterial cellulose nanofibers.
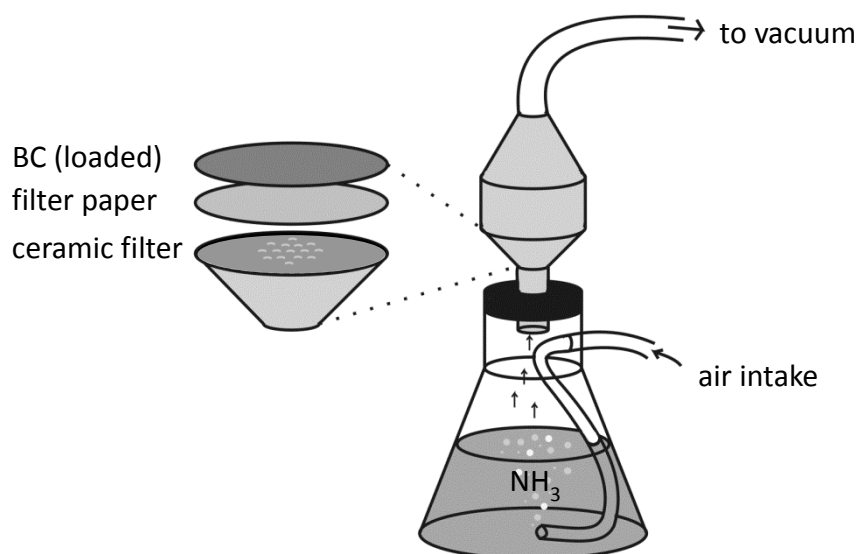
2.6 Processing of BC and BC-Iron Oxide Composites

2.6.1 Washing Procedures for BC and BC Composites

For pure BC samples, to remove bacterial cells and media from the cellulose matrix to achieve pure cellulose samples, BC was boiled in a 1 molar (1mol/L, or 1 M) solution of sodium hydroxide, or NaOH (Fisher) for 1-2 hours in an autoclave at 121°C depending on sample thickness. The pellicles were then washed with distilled H_2O for 5 minutes until neutral pH 7 was reached. Pellicles were used in subsequent processes; for example, co-precipitation synthesis reactions for coating iron oxide NPs.

BC composite samples were washed by sonication in DI H_2O three times to remove the impurities present depending on the production process, and in specific cases decanted magnetically.

2.6.2 Blending to Homogenize Samples

Select pellicles were blended in a Waring commercial blender or Brinkmann homogenizer for three minutes and poured or pipetted into 40 mL centrifuge tubes and centrifuged at 10,000 rpm at -4°C for 10 minutes. To remove NaOH and cell and media debris, the supernatant was removed by pipetting, and a wash cycle, which entailed adding 30 mL Milli-Q (Millipore™) water, vortexing 15 seconds, and re-centrifuging, was conducted a total of three times until neutral pH 7 was reached.

The supernatant was removed by pipetting, and the samples were frozen at -80°C for a minimum of 15 minutes to prepare for lypophilization.

2.6.3 Magnetic Separation Wash for Composite Samples Produced in Growth Media

Composite samples of BC grown in situ with iron oxide nanoparticles in the media were processed with magnetic separation or by the standard wash cycle described previously if not possible to separate the material with a magnet. Aside from magnetic separation, no other procedure was specifically undertaken to remove the bacterial cells that remained in preparation for all characterizations. Composites were blended in a Brinkmann homogenizer at 6 setting for three minutes in 40 mL centrifuge tubes. The tubes were placed in a magnet for 3 minutes, and then the supernatant was pipetted away. For the wash cycle, 30 mL aliquots of Milli-Q water were added, the samples were vortexed 15 seconds, and the samples were re-separated magnetically. The wash with magnetic separation was conducted a minimum of three times until the liquid turned clear.

2.6.4 Centrifugation

The centrifuge tubes containing washed materials were centrifuged at 7,422-10,000 rpm at -4°C for 10 minutes in Beckman Coulter JS-13.1 Avanti HP-30I centrifuge to pellet the sample, the supernatant pipetted away, and the tube frozen at -80°C for a minimum of 15 minutes to prepare for lypophilization.

2.6.5 Lypophilization (Freeze-drying)

The samples to be lypophilized were cryofrozen at -80C for a minimum of 15 minutes then placed under vacuum in a glass jar (and as needed, maintained in an ice bath) for up to 24 hours until dry. The lyophilization method for drying BC material (in the case of this research: used as matrix for precipitating NPs) is an important factor for effective deposition of iron oxide because it influences the fibrous structure of cellulose. Research has demonstrated that lyophilization (freeze-drying)   is generally an efficient method for drying bacterial cellulose material and has advantages over either oven-drying or alcohol substitution methods.

2.6.6 Grinding Bacterial Cellulose into Powders

To make BC-iron oxide nanocomposites for analysis by TEM, purified BC was powdered by grinding in a SPEX 8000M high-impact ball mill. Powders were sieved with a Dual Manufacturing Standard Testing Sieve size No. 60 (250 μm mesh).

2.7 Optical Microscopy

An optical microscope (Nikon) utilizing 10X, 40X, and 100X magnification was used to examine the morphology of *Gluconacetobacter* in static and agitated cultures and colonies from agar plates and to observe the bacteria in conjunction with its cellulose. Aliquots of liquid from static and agitated cultures were placed on a glass slide and examined. Clear gelatinous cellulose samples were collected on a wire loop from the pellicle and were examined. Colony morphology was examined with an optical microscope to determine if the colonies morphologies were homogeneous; in other words, to check if one strain of bacteria existed or if other bacteria or other organisms might be present, exhibiting different colony morphologies.

2.8 Field Emission Scanning Electron Microscopy (FESEM)

To investigate the morphologies of the materials, the samples were characterized by electron microscopy which was conducted with a high-resolution Supra 35 variable-pressure field emission gun scanning electron microscope (Zeiss), commonly referred to as a field-emitting scanning electron microscope (FESEM), operated at an accelerating voltage of 5-20kV. Samples were first mounted on carbon tape and coated with carbon in an evaporator coater (company). The measurement conditions for all samples were 5 kV gun voltage (EHT), 20 µm aperture size, 3-6mm working distance. Both the In-lens and SE 2 detector were employed. Prior to characterization by FESEM, the samples were either freeze-dried following treatment at -80°C for 15 minutes, or dried under ambient conditions, and then coated with atomic layers of graphite or gold.

2.9 Transmission Electron Microscopy (TEM)

Transmission electron microscopy experiments of the BC-iron oxide nanocomposites were carried out in a JEOL JEM-2010 TEM, operating at 120 kV. The powdered samples loaded with iron oxide nanoparticles were mounted on a copper grid after suspension in alcohol.

2.10 Energy-dispersive X-ray Spectrometry (EDX)

The BC-IO NPs (syn) composite was chemically analyzed using an energy dispersive spectrometer (EDAX Inc.) which has a theoretical detection limit of about 0.08 wt%.[175] Identification of elements in the measured spectrum and spectral data processing was performed using the EDAX

NSS software (Thermo Scientific). The EDX detector was employed in the FESEM on the gold-coated samples at 20 kV accelerating voltage.

2.11 Dynamic Light Scattering (DLS)

To determine the size of the synthesized iron oxide NPs, silica-coated iron oxide NPs, and iron oxide-coated Fe^o NPs, dynamic light scattering (DLS) measurements were conducted utilizing a ZetaPALS instrument with ZetaPlus Particle Sizing Software (Brookhaven Instruments Corp.) at 25°C, an angle of 90°, and a wavelength of 660nm for a total of 9 runs at 1 minute each per sample.

Aliquots of the IO NPs (syn), SiO_2 IO NPs, and STAR IO NPs were placed in 95% ethanol, and sonicated for 10 minutes. The solutions were held statically for 5 hours and the larger particles settled out, leaving the solution clear, and a 3 µL aliquot of the supernatant containing suspended NPs was pipetted into a cuvette and allowed to settle for 24 hours prior to measurement for all samples. Prior to DLS analysis, the NP samples were sonicated for 10 minutes in 95% ethanol. For all samples, 3 µL aliquot of the suspended NPs was pipetted into a cuvette and allowed to settle for 24 hours prior to measurement.

2.12 X-ray Diffraction (XRD)

X-ray diffraction (XRD) was used to verify the type of iron oxide comprising the SiO_2 IO NP, STAR IO NP, and presence of synthesized iron oxide nanoparticles (IO NP (syn)), in the nanostructure of bacterial cellulose and to study how the iron oxide nanoparticles affect the BC crystal structure after incorporation of the synthesized iron oxide NPs into BC to make the BC-IO NPs (syn) nanocomposite. XRD evaluates the crystallinity of the samples and identifies the chemical composition by measuring the atomic spacing in the crystal structures via the diffraction of monochromatic x-radiation.

XRD measurement data was plotted as strength (relative intensity) vs. position (angle, in 2θ) to produce a series of peaks called a diffraction pattern or spectra. From the resulting intensity versus angle plot, inferences can be made about the structure of the material. XRD diffraction spectra were generated using an X-Ray Diffractometer (Siemens D5000, Bruker) with a copper k-alpha (Cu-k_α) radiation source with a wavelength of 1.5418 Angstrom (Å) at a target voltage of 40 kV and a current of 20-30 mA. The XRD data were collected and computed using DIFFRACplus software (Bruker-Siemens) over a 2θ scan distance from 5° to either 50° (for most pure celluloses) or 85° (for iron oxides , BC-iron oxide composites, and some cellulose samples) at a continuous scanning rate, a

step size of 0.02°, and a step time of 5 seconds. The XRD diffraction spectra were analyzed with EVA software (Bruker-Siemens) to evaluate the crystallite size, the degree of crystallinity, also referred to as the crystallinity index, and to identify the presence of elemental iron Fe^o and the paramagnetic iron oxide phases Fe_3O_4 or γ-Fe_2O_3.

The crystallinity index (CI), and crystallite size (CS) were calculated based on X-ray diffraction measurements. Crystallinity of the samples was estimated by the peak height method, the simplest and most common method used to study native cellulose.[43] In the peak height method, the crystallinity of cellulose is calculated from the ratio between the intensity of the highest peak at 2θ between 22-24 degrees corresponding to the 002 plane and the intensity of the background signal, assumed to be the amorphous portion of the sample, taken at the low point between the 002 peak and the 110 peak, or at ~2θ at 18 degrees using the following equation:

$$CI = \frac{(I002 - Iam)}{I002} \times 100 \ [\%]$$

For the synthesized iron oxide nanoparticles, the crystallite size was estimated by substituting the full-width at half-maximum (FWHM) into the Scherrer equation[42] :

$$CS = \frac{K\lambda}{B\cos\theta}$$

where K is the constant 0.94, λ is the X-ray wavelength 1.5418 Å , B is FWHM in radians.[176] The contribution of the iron oxide nanoparticles in composite fibers on the crystallinity of the cellulose matrix was not taken into account.[177]

2.13 Attenuated Total Reflection Fourier Transform Infrared Spectroscopy (ATR-FTIR)

To investigate the chemical composition of the sampled materials and the specific chemical interactions developed between components in the composite materials, attenuated total reflection Fourier-transform infrared spectroscopy (ATR-FTIR) was used for evaluating the chemical groups present. Infrared spectroscopy of the samples was conducted with a Nicolet Magna-IR-760 Fourier transform infrared (FTIR) spectrometer (Thermo Fisher Scientific, Inc.) and a Harrick SplitPea™ ATR accessory with a silicon crystal internal reflection element (IRE). The IR spectra were recorded in the frequency range between 4000 and 400 cm^{-1} with an accumulation of 64-250 scans at a resolution of 2 cm^{-1} and a gain of 4 utilizing OMNIC software (Thermo Scientific). Prior to sample measurement, the spectra were corrected for ambient conditions using baseline: a background scan of the cleaned

IRE under ambient conditions was conducted to correct spectra to a baseline. The samples were prepared as detailed in the sample production section and were pretreated by lyophilization and stored under ambient conditions. All FTIR spectra were subjected to automatic baseline correction. The OMNIC Spectral Math subtraction function was used to perform the subtraction operation [A - k*B] (where A is the mixture spectrum, k is the subtraction factor and B is the single-component spectrum) on select sample spectra for analysis. Data was analyzed using Omnic and Excel software.

3. RESULTS AND DISCUSSION

This research focused on making composites of BC and iron oxide NPs and examining the interaction of these two materials; therefore, some results involving the production of BC composites by co-precipitation methods as well as the production of BC by static and agitated methods will be discussed. However, this research is not a study of production optimization. While the research and development of optimized cellulose production and processes is important, it is beyond the scope of this research. For example, BC yield and failure rate of growth of BC was not investigated in this research and will not be discussed. Some aspects of the production of BC and BC-iron oxide composites will be discussed, such as the challenges encountered during the process of producing material for this study.

3.1 Morphology of Iron Oxide NPs: SiO$_2$ IO NPs, STAR IO NPs, IO NPs (syn)

3.1.1 Dynamic Light Scattering (DLS) Results

Dynamic light scattering (DLS) measurements were conducted on the NP samples SiO$_2$ IO NPs, STAR IO NPs, and the synthesized iron oxide NPs, IO NPs (syn), for a total of 9 runs at 1 minute each per sample. An effective diameter for the NP samples was calculated for the measurement overall as well as for each run, and the mean and standard error were provided for all data. DLS results indicated that the effective average diameter of the SiO$_2$ IO NPs was 588 nm with a standard error of 23.9 nm, the effective diameter of the STAR IO NPs was 308 nm with a standard error of 29.7 nm, and the effective diameter of the synthesized iron oxide NPs was 142 nm with a standard error of 0.8 nm. The larger size of the SiO$_2$ IO NPs and STAR IO NPs may be due to aggregation; in addition, the silica coating on the SiO$_2$ IO NPs contributes to size. DLS analysis revealed the size of the NPs and provided some evidence of aggregation of the SiO$_2$ IO NPs and STAR IO NPs.

3.1.2 Morphology of SiO$_2$ IO NPs and STAR IO NPs as Powders and in Aqueous HS Media

Scanning electron microscope images confirm the clustering, or aggregation, of the SiO$_2$ IO NPs both before and after usage in the experimental aqueous culture medium as shown in Figures 3.1 and 3.2. Nano Iron reports that Nanofer 25 is an aqueous slurry characterized by agglomeration and sedimentation.[163] Other researchers report that iron oxide NPs tend to aggregate and sediment rapidly in de-ionized water.[105] In Figure 2.3 provided by Nano Iron, Inc., both STAR and Nanofer 25 appear to be aggregated. Nanoparticle aggregation has several causes. The aggregation of iron oxide NPs is reported to occur when they are powdered, heated, or placed in aqueous environments. Heat treatments and aqueous environments also cause NPs to agglomerate. NPs aggregate due to their

high surface area and interfacial energies. Researchers report that aggregation of paramagnetic iron oxide NPs may be caused by the van der Waals force between the NPs.[172] Aggregation of nZVI particles occurs due to long-range magnetic attractive forces and nZVI ionic strength in aqueous environments which increase the aggregation of nZVI particles.[178,179] STAR is declared to be a nano-scale zero-valent iron (nZVI) which has demonstrated and exhibited high reactivity in aqueous environments.[180-182]

The SiO$_2$ IO NPs used in this research were made of Nanofer 25, and they were heated in an oven-drying step after fabrication. Because the SiO$_2$ IO NPs are fabricated from Nanofer 25 which consists of aggregated NPs, they are also likely aggregated. STAR and SiO$_2$ IO NPs were used in the aqueous HS media for all experiments; therefore, they aggregated, as revealed by optical (Figure 3.2) and FESEM micrographs (Figure 3.1).

Figure 3.1: FESEM of aggregated silica-coated Nanofer 25 nanoparticles SiO$_2$ IO NPs displaying a 1 μm scale bar at 10 kx magnification and an enlargement with a 500 nm scale bar at 20 kx.
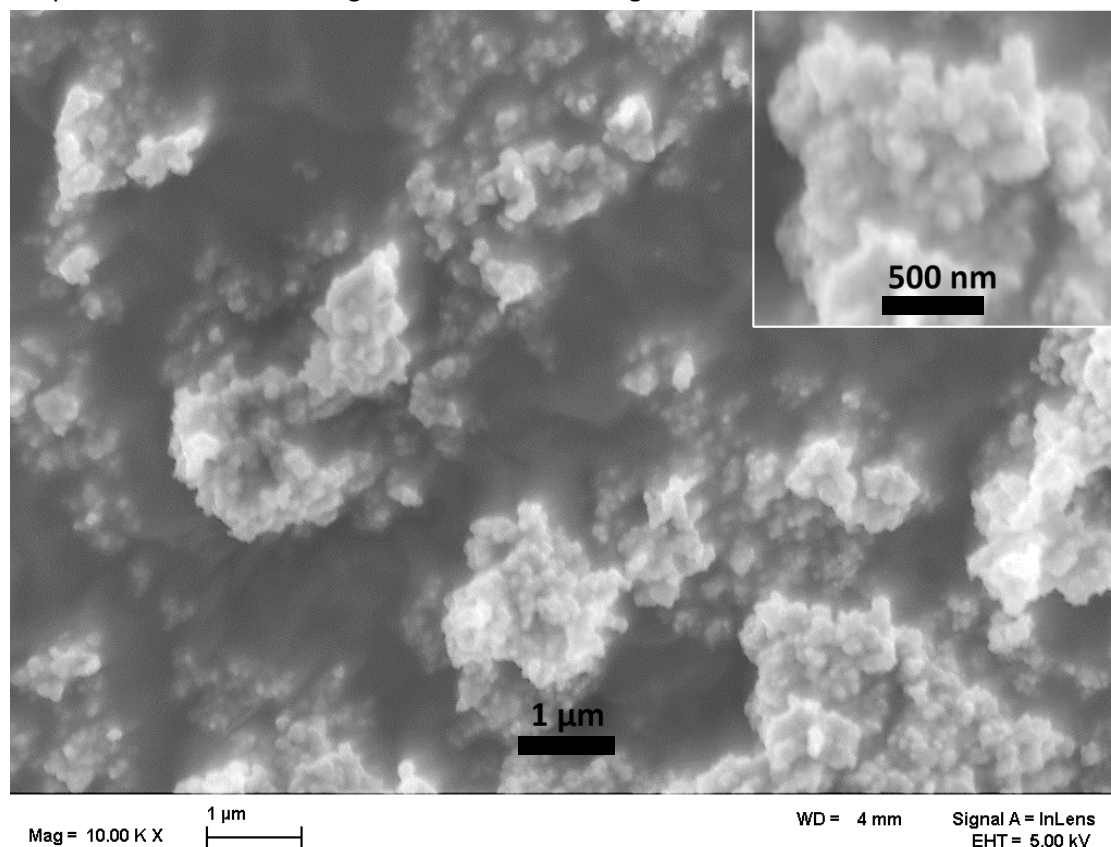
Figure 3.2: Optical micrographs of NPs in HS media (a) SiO$_2$ IO NPs at 10× and 1000× magnification and (b) STAR IO NPs at 1000× magnification showing the aggregation of these NPs in the HS Media.
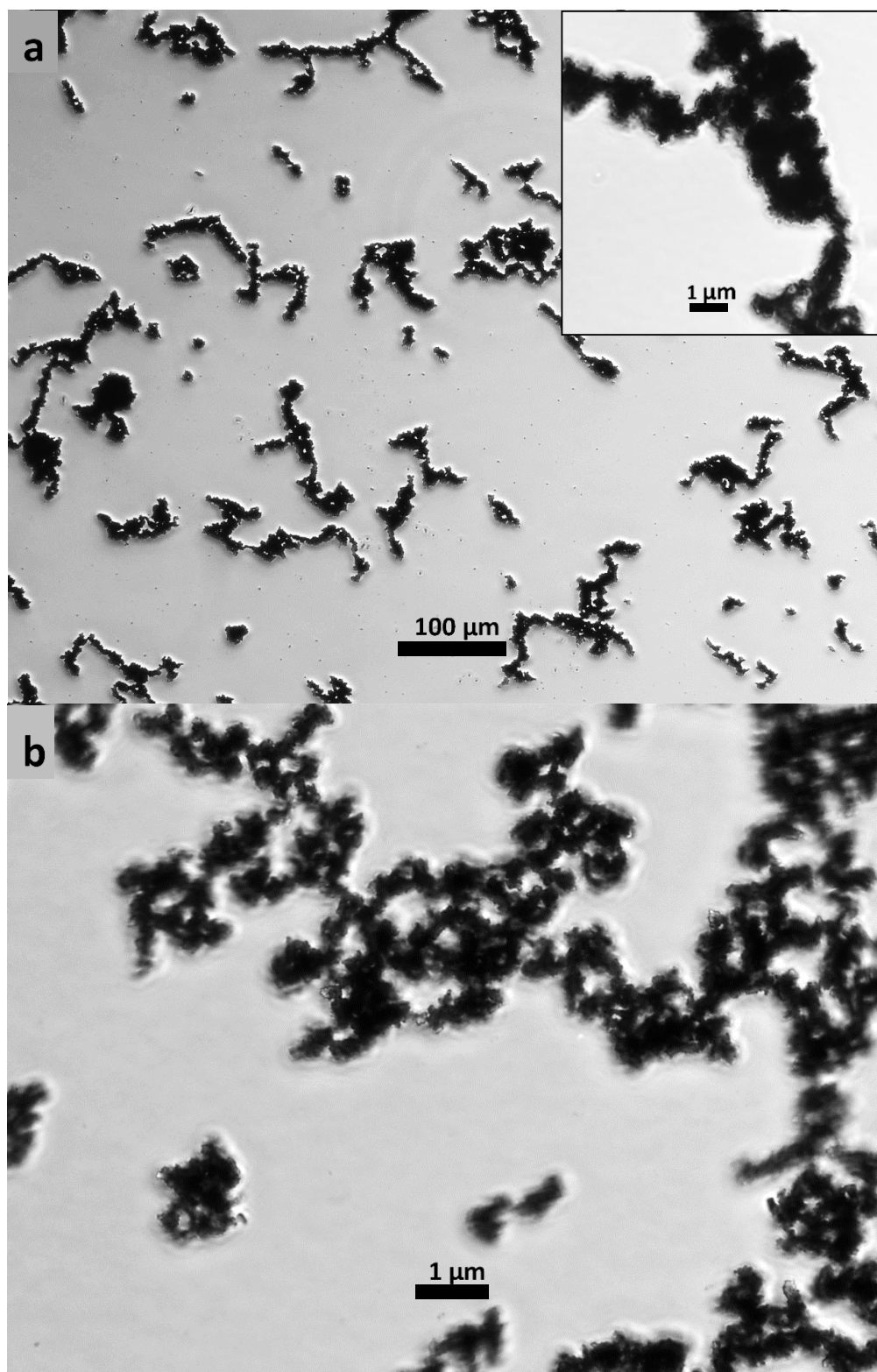
3.1.3 Color of Iron Oxide NPs for Identification: SiO₂ IO NPs, STAR IO NPs, IO NPs (syn)

One characteristic of iron oxides is their color variation depending on the type: magnetite (Fe_3O_4) is black, maghemite (γ-Fe_2O_3) is red-brown to brown. Therefore, color is one visual method to approximate the types of iron oxide NP that were acquired and synthesized for this research.

STAR and silica-coated Nanofer 25 were the iron oxide NPs used for the BC-iron oxide composites fabricated during BC biosynthesis in the growth media. STAR was black, which indicates it contained Fe_3O_4, and SiO_2-coated Nanofer 25 was dark brown which suggests it contained Fe_3O_4 or a mixture of Fe_3O_4 and γ-Fe_2O_3. The synthesized iron oxide NPs were black, which indicates it contained Fe_3O_4.

The BC-iron oxide composites prepared by the co-precipitation methods (reverse co-precipitation and ammonia gas-enhancing in situ co-precipitation) had uniform coloring across the BC membrane area of the sample which indicates a homogeneous dispersion of the precipitated magnetite and/or γ-maghemite NPs in the BC matrix.

In the reverse co-precipitation method the BC-iron oxide NP composites ranged from light yellowish-brown, or tan for the 0.01 mol/L samples to dark brown for the 1 mol/L samples. Dark brown indicates that the IO NPs (syn) in reverse co-precipitation samples are maghemite.
In the ammonia gas-enhanced in situ co-precipitation method, especially in the 1 M sample, is when ammonia gas was purged initially into the reaction vessel a notable observation was that the iron precursor-loaded BC membrane immediately became dark brown, but as the ammonia gas was quickly diluted with oxygen and dissipated, the oxygenated sample changed to orange-brown. As a result, the final state of these BC-iron oxide composites ranged from yellow (0.01 mol/L) to orange-brown (1 mol/L). This change suggests that the iron oxide NPs in the samples is maghemite after oxidizing from magnetite, as well as other phases of iron oxide.

The XRD results and color of the IO NPs indicate that there was less oxygen exposure in the IO NPs (syn) synthesized in the BC matrix by the reverse co-precipitation method than by the NH_3 gas-enhanced in situ co-precipitation method. This makes sense as the former involved submerging the composite in ammonia, therefore less exposure to air, whereas the latter involved pulling ammonia vapors through the composite in ambient air. The IO NPs (syn) samples by the NH_3 gas-enhanced in situ co-precipitation method first turned dark brown upon exposure to the NH_3 vapors, but quickly turned orange-brown which indicates an increase in the oxygen content in the system. The initial NH_3 vapors were pulled through the samples by the vacuum, but could not replenish and

therefore air was subsequently pulled through the samples, causing Fe_3O_4 to quickly turn into γ-Fe_2O_3, α- Fe_2O_3, and FeO(OH).

The coloration of the BC-iron oxide NP composites is difficult to interpret, and inconclusive in determining the type of iron oxide is present because the BC fibers affect coloration: the BC-iron oxide composite samples exhibited a range of color depending on the concentration of NPs in the BC matrix and the thickness of the BC membrane. The BC-iron oxide NP composites prepared by synthesis in the co-precipitation method varied in color in a range of tints and shades, from light yellow or yellow-brown to dark brown depending on the concentration of the ion salt precursor solutions, the thickness of the BC membrane, and the co-precipitation method used. (Note that for the co-precipitation experiments, the BC membranes were approximately the same thickness as they were produced in the same batch with the same amount of media, inoculation amount, and growth time).

3.2 Results of BC Production in Culture Media: Static and Agitated Methods

While *Gluconacetobacter* produces cellulose most prolifically under static culture conditions, agitated production is desired in industry so that BC production can occur in large bioreactors, which would be more efficient, take up less space, and allow better control over culture conditions. BC pellets formed in agitated cultures of some *Gluconacetobacter* strains are desirable as they are compact, like beads, and have many applications. Researchers found that the dominant factor influencing both the formation of BC pellets is a strain capable of producing pellets and culture media fluid dynamics, which could relate to shear forces on the surface of the forming pellets.[144] In preparation for the agitated experiments in this research, when pellets formed in test batches, the bacteria in those particular test experiments were collected for future inoculation of media. In this manner, strain selection was performed in this research.

However, cellulose production in fermentors with continuous agitation presents many problems, including the spontaneous appearance of bacterial mutants which do not produce BC (BC nonproducers, also known as Cel- mutants) which contribute to a reduction in BC production.[141] Researchers have discovered that one of the main factors causing the reduction or absence of BC production in agitated culture conditions is the fluid dynamics of the culture medium.

Researchers have had taken various positions on the issue of agitated culture media. Some insist that dissolved oxygen is the problem of reduced BC production and claim that shaken at low rpms provide best results. Others demonstrate that oxygen is necessary and not the cause of

reduced BC production. Other have found that an rpm below 100 causes all strains to stop producing cellulose, even those known to produce well in agitated conditions.[144]

The problem with rotary horizontal shakers, which were the types used in this research, is that the culture media is spun in one direction repeatedly and is not truly agitated; therefore, this spinning does not significantly increase the surface area at the air interface or aerate the media enough to cause significant levels of dissolved oxygen. Research indicates that the phenomena of cellulose mutants (cellulose negative variants) is not caused by dissolved oxygen in agitated cultures; but rather, high concentrations of the gluconic acid by-product from *Gluconacetobacter.*[183]

During this research, sometimes the agitated culture experiments resulted in the absence of cellulose, for instance, when rpms of the rotary shaker were either too high or too low, and when larger flasks with deeper levels of media were used. Different media volumes, flask sizes, and rotational speeds were tested in the process of producing BC and BC-iron oxide composites by static and agitated methods. The variation of flask sizes and media volumes resulted in different aeration and media fluid motion dynamics, which influenced the shear forces in the media as well as oxygen dissolution rate.[144]

Agitation with rotational speeds up to 250 rpm were investigated during this research in the process of selecting suitable agitated culture conditions to obtain BC growth; the 160 rpm rate was most productive, and selected so that materials could be produced for this research.

In the process of developing methods for producing BC, test experiments were conducted using various culture flask sizes and culture media amounts. The containers used for BC production experiments included a 50mL long-neck shaker culture flask (PYREX®) topped with a Morton culture tube closure with an approximately 50 mm outer diameter of the base, a 125 mL Erlenmeyer flask with a bottom outer diameter of 70 mm topped with a screw-lid or foam stopper, a 250 mL Erlenmeyer flask with an outer-diameter base of 85 mm topped with a foam stopper enclosed with aluminum foil, and a Roux culture bottle. The HS media was measured into the containers as follows: 10 mL HS into the 50mL Erlenmeyer flasks, 50 mL HS into the 125 mL Erlenmeyer flasks, and 100 mL HS into the 250 mL Erlenmeyer flasks, and 25 mL into the Roux flasks. The amount of inoculum added was 1-5 mL for the 50 mL flasks and approximately 5 mL inoculum for the 125 mL, 250 mL, and Roux bottles.

The main set of experiments of this research for the production of pure BC and composites of BC and iron oxide NPs were conducted in 50 mL Erlenmeyer flasks containing 10 mL HS media

inoculated with 2 mL aliquots of culture media containing pre-cultured cells, and then incubated under either static or agitated conditions.

The agitated cultures in this research inconsistently produced BC or BC-iron oxide composites: in some experiments, BC was produced, in others, no BC was generated by *Gluconacetobacter hansenii*; the absence of cellulose is an indication of strain mutation to become non-producers of cellulose; this was likely the case in this research. In agitated experiments, *Gluconacetobacter hansenii* demonstrated a sporadic ability to create roundish masses, or pellets. In some cases, pellets of BC or BC-SiO$_2$ NPs composites resulted, but masses were often irregularly shaped, clumped, or string-like.

3.3 Results of BC, BC-SiO$_2$ IO NP, and BC-STAR IO NP Production

3.3.1 BC, BC-SiO$_2$ IO NP, and BC-STAR IO NP Production: Static and Agitated Methods

A series of BC- SiO$_2$-IO NP and BC-STAR IO NP composites were generated by varying the concentration of iron oxide NPs (5 mg, 10 mg, 20 mg, and 40 mg in 50 mL Erlenmeyer flasks containing 10 mL HS media inoculated with 2 mL aliquots of culture media containing pre-cultured cells, and then incubating under both static and agitated incubation conditions to endeavor to produce BC in distinct culture media with differing NP concentrations for each type of iron oxide. BC samples were also produced by the same procedure to compare to the composites.

The iron oxide NPs were not uniformly distributed or dispersed in the BC-SiO$_2$ IO NP or BC-STAR IO NP composites fabricated in the culture media during BC biosynthesis. In the static and agitated growth media, only a portion of the NPs were trapped in the BC fibers. Areas of the composite material ranged from light to dark values depending on the concentration of NPs entangled in the BC fibers.

As the bacteria cells exude cellulose, the nanofibers trail from the bacterial cells and stack in ribbons and intertwine, trapping NPs in the culture media. Fiber branching occurs as the bacteria multiply and separate, which causes the nanofibers intertwine into a mesh, or network. The NPs in the culture media become entangled in the nanofiber network.

The entangled BC fibers and IO NPs were observable in the pellicles of the static experiments as shown in Figure 3.3. The bacteria cells dragged the entangled NPs behind them in the fibers, and these trailing fibers became intertwined, creating bundles of fibers. The BC fibers that trapped NPs became larger and longer as the NPs were dragged behind the bacterial cells in fibers which in turn tangled with more fibers including the nearby fibers exuding from the bacterial cell walls.

The bacteria normally move in a circular pathway, pushed forward by the backward forces of the exuding cellulose nanofibers, and as they drag the bundled fibers and entangled NPs, the bacteria spirals and the bundle becomes twisted. Large composite fibers of cellulose nanofibers and iron oxide NPs were formed. These fibers, with trapped NPs, are larger and more twisted than BC fibers without the NPs.

The silica coating caused the SiO_2-IO NPs to be inert and non-toxic, which enabled *Gluconacetobacter* to thrive and produce cellulose in both static and agitated culture media solutions.

In static growth media, the NPs settled on the bottom of the growth media flasks due to aggregation causing increased size and weight (suspended NPs were negligible). Only a portion of the NPs came in contact with the BC fibers because *Gluconacetobacter* produces BC near the media surface in static conditions. Only the NPs on the top of the settled NP layer at the bottom of the flask nearest the *GAB* cells became entangled in BC nanofibers. BC forms in sheets of intertwined nanofibers, and as *GAB* cells producing cellulose moved toward the air-liquid interface near the media surface, distinct sheets of BC formed. Nanofibers in the BC sheet in contact with the NP layer entangled some NPs, but subsequent sheets of intertwined BC nanofibers did not contain NPs, because the BC material was white in color, as shown in Figure 3.3.

Figure 3.3: Series of static culture experiments for producing BC and BC-SiO_2 IO NP composites containing *Gluconacetobacter* cells and SiO_2 IO NP in 5 mg, 10 mg, 20 mg, and 40 mg amounts in 10 mL HS Media and incubating for 7 days.

SiO_2-coated Iron Oxide Nanoparticle Amount in Media:

| **5 mg** | **10 mg** | **20 mg** | **40 mg** |
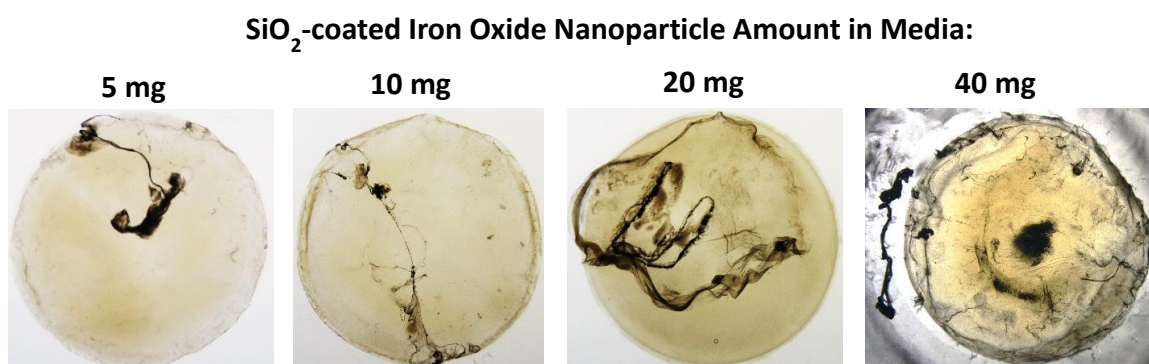
In agitated growth media, the NPs settled to the bottom of the flasks, and collected into the middle of the bottom of the flask, especially for lower amounts of NPs, by the centrifugal forces of the rotary shaker as seen in Figures 3.4 and 3.7.

For the agitated cultures, 24 hours after inoculation the pure BC samples exhibited evidence of BC growth: many tiny BC masses appearing as oval-shaped particles less than an eighth of a cm in diameter were suspended in the culture medium. 48 hrs after inoculation, the tiny BC masses in the *GAB*-only cultures had conglomerated into one clumped mass as shown in Figure 3.4, and a few flake or particle-like tiny masses were forming in the SiO_2-IO NP sample cultures.

In the BC-SiO_2 IO NPs experiments, agitated in rotary shakers, the SiO_2 IO NPs swirled in the bottom of the flask and accumulated toward the center especially for lower amounts of NPs. As BC was produced, roundish black masses, or pellets, formed 24 hours after inoculation as shown in Figure 3.4. In the 20 mg and 40 mg samples, excess NPs spread out along the flask bottom. After 48 hours, the composite pellets were larger. In BC- SiO_2 IO NP composites, a different morphology existed for the interior and the exterior of the composite pellets formed by agitation as shown in Figures 3.4 and 3.5: ATR-FTIR conducted on the outside region of the pellet revealed the characteristic cellulose spectra and the presence of *GAB* cells as indicated by the Amide I and II peaks, and ATR-FTIR conducted on the black interior region of the pellet revealed the spectra characteristic of the SiO_2IO NPs with peaks of the Si-O asymmetrical stretch, and the absence of peaks associated with cellulose and *GAB*. As the media containing *GAB* cells swirled around the clumped NPs, BC formed and encased the NPs with an exterior layer of BC, forming black pellets. The black interior of the pellets was composed of mainly SiO_2 IO NPs, whereas the transparent exterior which encased the NPs was composed of mainly BC, as confirmed by ATR-FTIR in Figure 3.5. The outer cellulose layer of the pellets is saturated with water, so it is very difficult to determine the thickness. The scale bar provides a reference to visualize the relationship of the cellulose layer to the BC-encapsulated SiO_2 IO NPs.

Figure 3.4: Series of agitated culture experiments for producing BC and BC-SiO$_2$ IO NP composites in the form of pellets using *GAB* cells and 5 mg, 10 mg, 20 mg, and 40 mg of SiO$_2$ IO NP in 10 mL HS media and agitating at 160 RPMs in a rotary shaker for about 5 days.
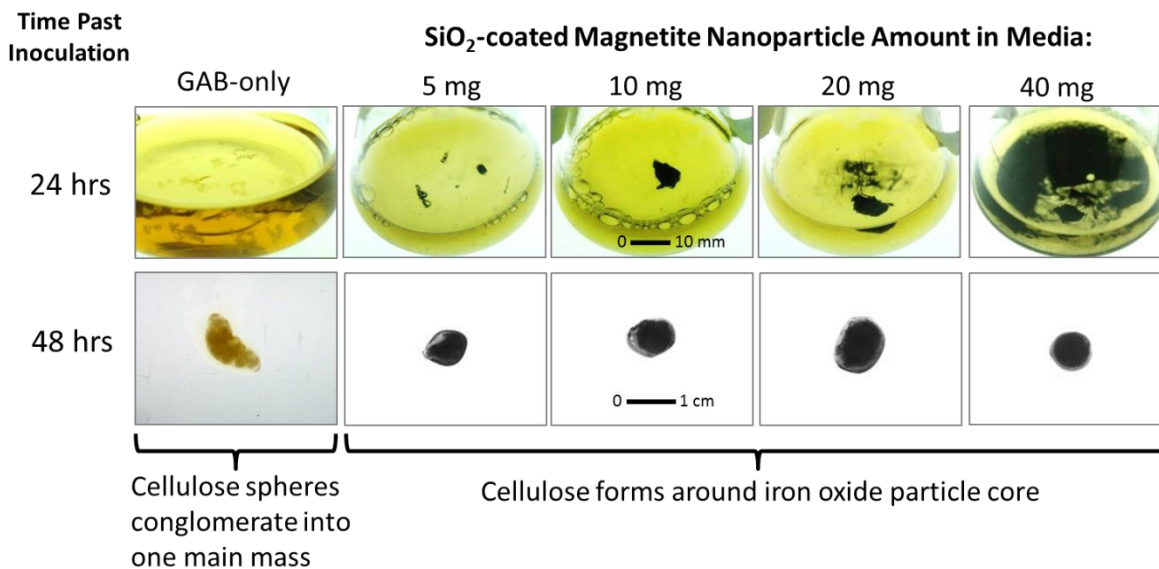
Figure 3.5: IR spectra of BC-SiO$_2$ IO NPs composites formed as pellets in agitated culture consisting of an exterior layer of bacterial cellulose and an interior of SiO$_2$ IO NPs .
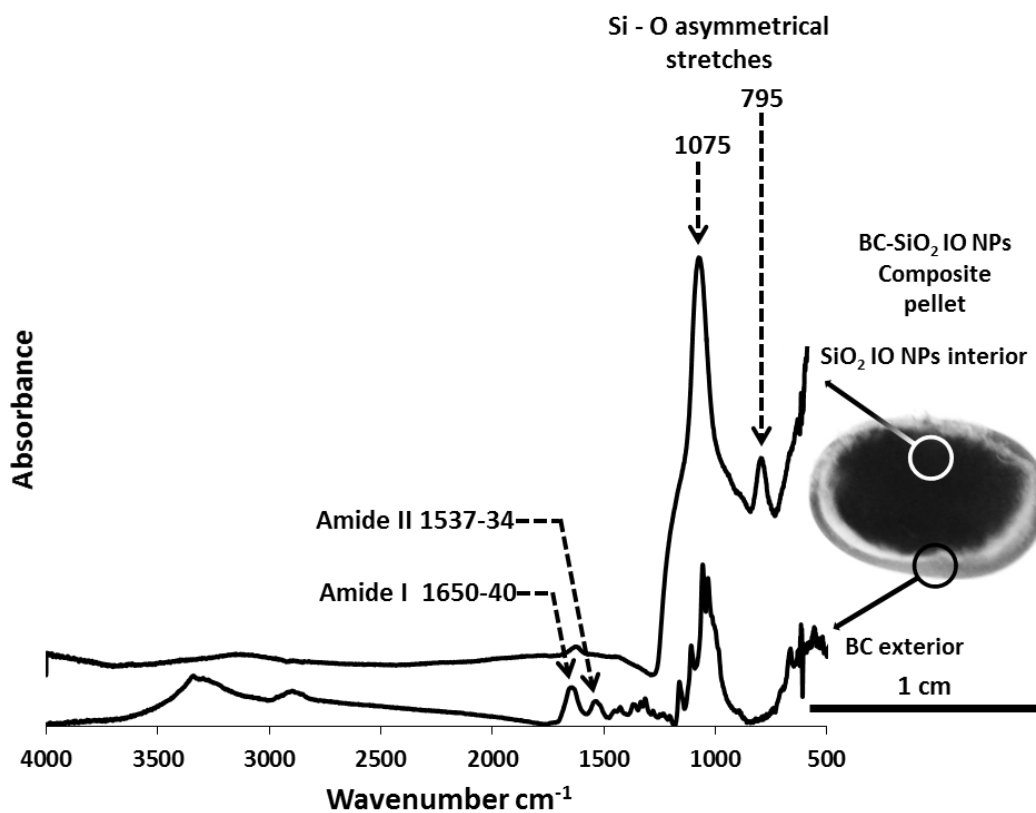
Nanofer STAR powder was used in culture media to produce BC-STAR IO NP composites primarily because it is reportedly stable in air due to the iron oxide shell over the reactive Fe^o core, and as a result it is safer and easier to handle, so the reasoning was that it would be a good iron oxide NP candidate for use in composites with BC. However, in contrast to SiO_2-IO NPs, little or no cellulose was produced in solutions containing the uncoated STAR IO NPs. Nanofer STAR is ZVI (an excellent electron donor that transforms via reduction or indirect oxidation) which can cause toxicity due to the production of reactive oxygen species (such as hydroxyl radicals and hydrogen peroxide in living cells) as well as Fe ions, which can enter the cytoplasm of cells and induce oxidative stress, damaging cell membranes leading to leakage of intracellular contents and cell death. In the static experiments, negligible amount of STAR IO NPs were entangled in BC fibers, whereas in agitated experiments essentially no BC was generated, as seen in Figures 3.6 and 3.7, most likely due to toxicity. The STAR NPs may have caused the nearby *GAB* cells to stop functioning properly (thereby inhibiting cellulose production), or die.

The 5 mg and 10 mg BC-STAR IO NP composites samples were so similar so the former was omitted; instead, the BC sample made only from *GAB* cells was presented in Figure 3.6 for contrast to the BC-SiO_2 IO NPs and BC-STAR IO NPs composites; note the dark area is HS media color in BC fibers.

Figure 3.6: Series of static culture experiments for producing BC and BC-STAR IO NP composites containing *Gluconacetobacter* cells and STAR IO NP in 5 mg, 10 mg, 20 mg, and 40 mg amounts in 10 mL HS Media and incubating for 7 days.

STAR Iron Oxide Nanoparticle Amount in Media:

BC (*GAB* Only)	10 mg	20 mg	40 mg
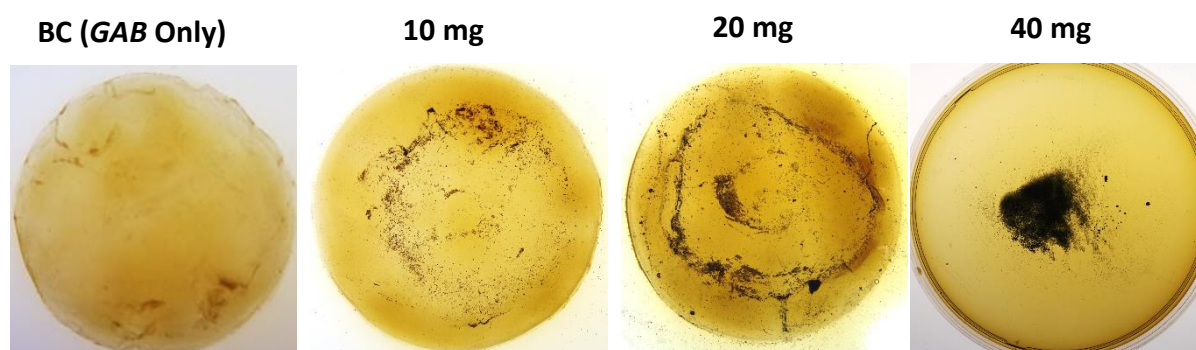
In the experiments with agitated culture media containing STAR NPs in 5 mg, 10 mg, 20 mg, and 40 mg amounts in 10 mL HS media, only the 5 mg STAR sample exhibited evidence of BC growth as shown in Figure 3.6. After 48 hours of incubation in the rotary shaker, tiny oval-shaped masses, or pellets, less than an eighth of a cm in diameter were suspended in the culture medium. However, the

amount of material produced was insignificant. The other BC-STAR IO NP samples showed no evidence of BC growth even after the standard BC growth time had passed and the experiments stopped.

The experiments incorporating iron oxide NPs in the BC growth media were conducted in water and air environments, in a temperature range from about 20°C room temperature (RT), to the culture media incubation temperature of 30°C. Therefore, the STAR NPs in the samples are expected to eventually oxidize, transforming from Fe^o to Fe_3O_4 , and eventually γ-Fe_2O_3 .[102]

Figure 3.7: Agitated culture media experiments for BC-STAR Iron Oxide Nanocomposites containing *Gluconacetobacter* inoculum and STAR IO NPs in 5 mg, 10 mg, 20 mg, and 40 mg amounts in 10 mL HS Media
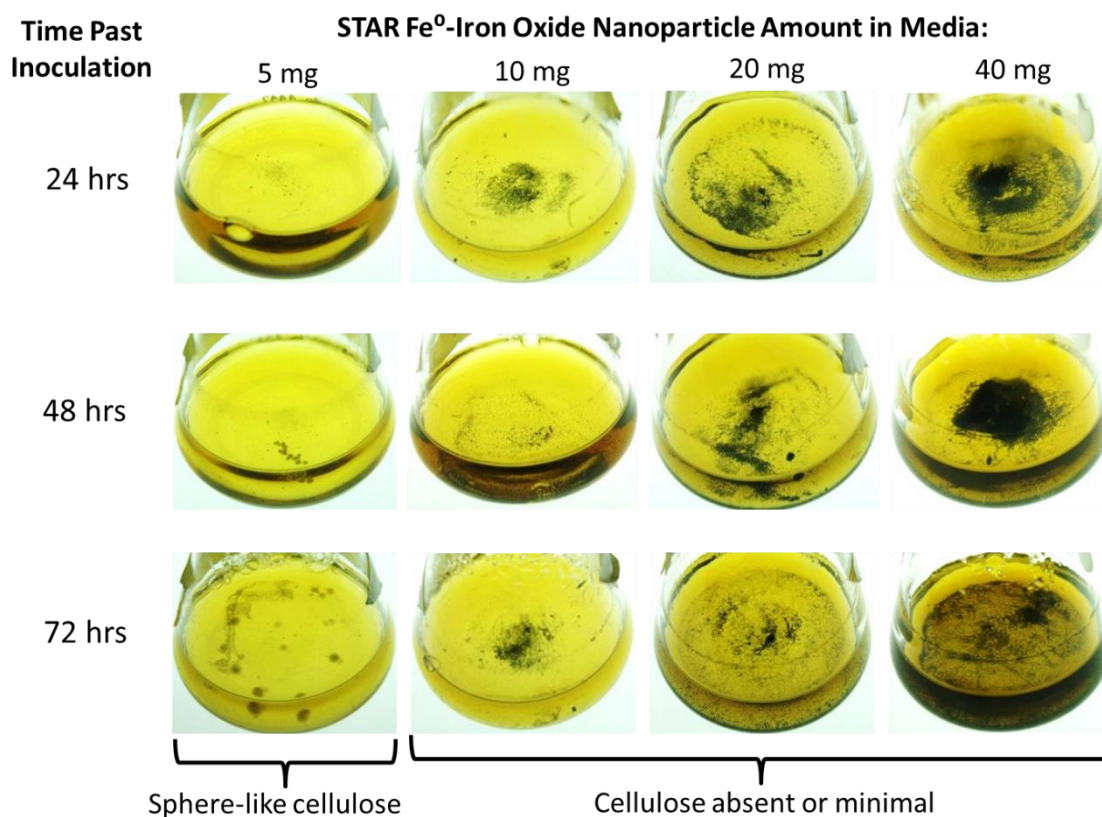
3.3.2 BC, BC-SiO$_2$ IO NP, and BC-STAR IO NP Production: Micrograph Results

The optical micrograph of the HS culture medium containing only *GAB* cells and cellulose fibers is shown in Figure 3.8. The *GAB* cells are rod-shaped; long chains of linked *GAB* cells were observed because the cells reproduce by cell division, but can stay attached. The BC nanofibers were observable as fine lines that intertwine and loop as the bacteria exude BC as they move in a circular path and divide.

The optical micrograph of the culture medium containing *GAB* cells and STAR IO NPs shows how the STAR IO NPs often had a toxic effect on the *GAB* cells and caused them to not produce cellulose (especially when the NP concentration was high) as shown in Figure 3.9. This micrograph also shows that the STAR IO NPs were aggregated in the culture media. Figure 3.10 reveals that the SiO$_2$ IO NPs were aggregated before they were used, when in a powder form (a) and after they were used in the growth media for producing BC-iron oxide composites and then processed with blending, washing with magnetic decantation, and lyophilization (b). Using SiO$_2$ IO NPs in the HS growth media results in composites with aggregated NPs that are entangled— physically trapped—in the nanofiber matrix along with the *GAB* cells that exude the nanofibers, as revealed by Figure 3.11. This morphology sporadically occurred for BC-STAR IO NPs composites depending on whether BC was produced or not. Comparison of the SEM micrographs in Figures 3.10 and Figure 3.11 shows how the SiO$_2$ IO NPs were aggregated before and after use, and how a samples produced during BC biosynthesis in growth media augmented with iron oxide NPs can be damaged by the processing steps of blending, magnetic decantation, and lyophilization.

Figure 3.8: Optical micrograph showing *Gluconacetobacter* cells and nanofibers of BC in an aliquot of the culture medium.
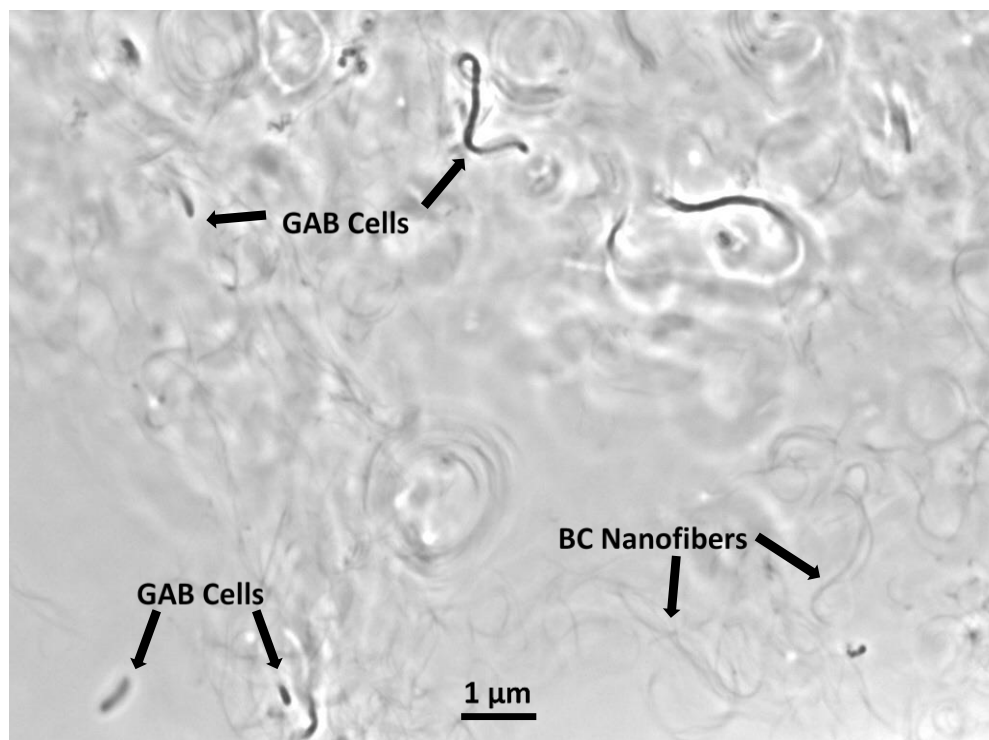
Figure 3.9: Optical micrograph showing the absence of BC in a culture medium containing *Gluconacetobacter* cell inoculum and STAR IO NPs.
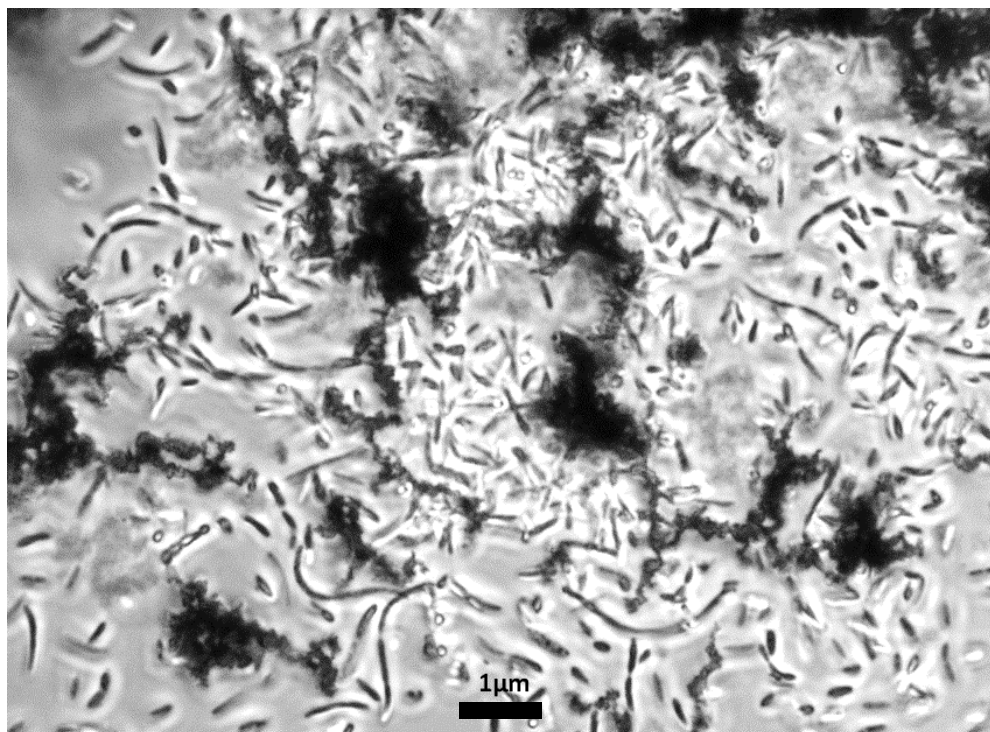
Figure 3.10: SEM images of aggregated SiO_2 IO NPs NPs (a) before usage, as a powder and (b) after used for production of BC-SiO_2 IO NPs in the aqueous growth media and processed with blending, washing with magnetic decantation, and freeze-drying.
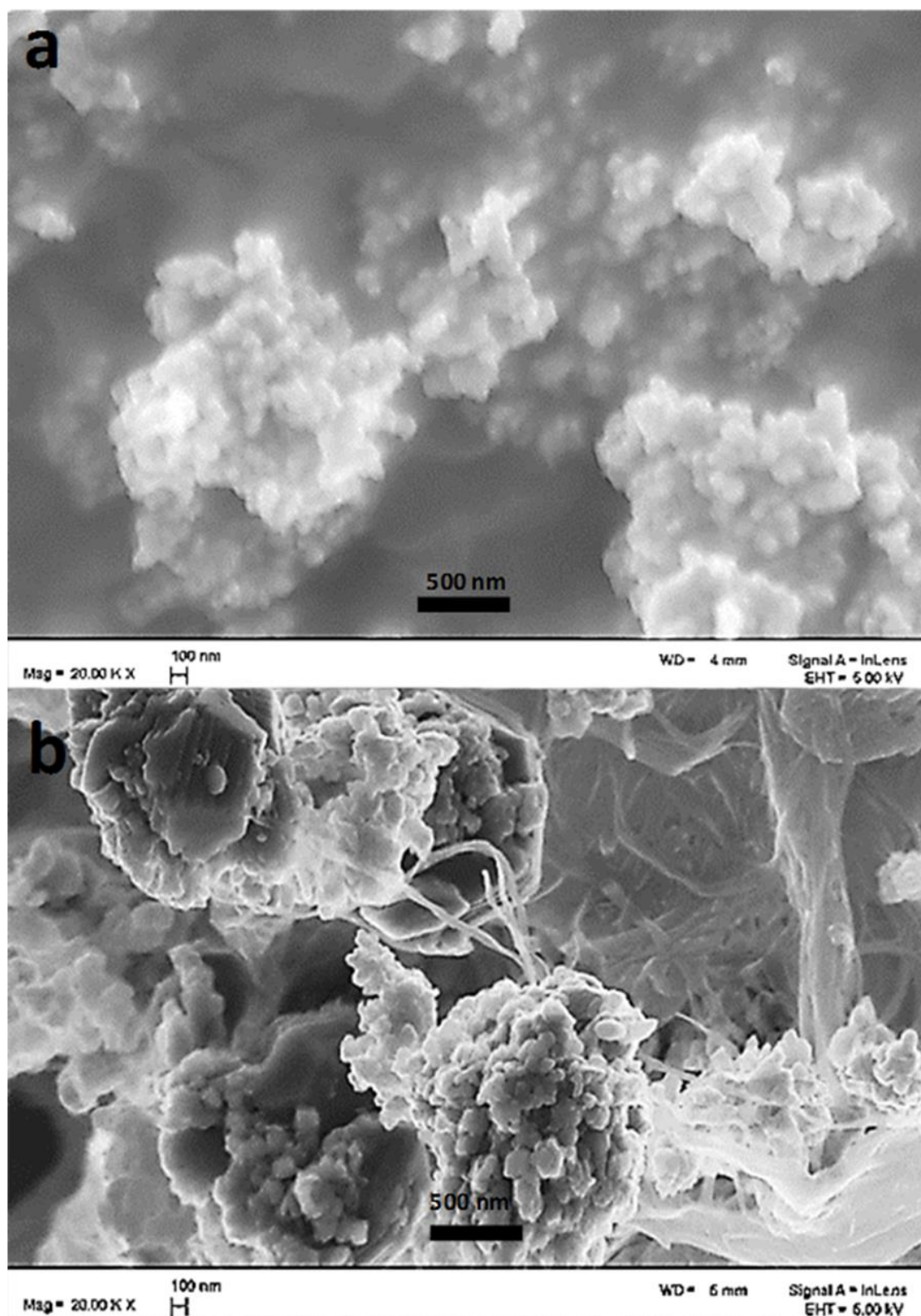
3.3.3 Evaluation of Processing BC and BC Composites BC-SiO$_2$ IO NP, BC-STAR IO NP

Although the samples were washed by sonication in DI H$_2$O to remove the HS medium and soluble by-products, *GAB* cells (and likely other entangled debris) were still present in BC-SiO$_2$ IO NPs and BC-STAR IO NPs composite samples as well as in BC samples that were only washed with DI H$_2$O; in fact, the presence of *GAB* cells was observed in ATR-FTIR spectroscopy as shown in Figure 3.5.

The BC-iron oxide NP composites formed during BC biosynthesis in the culture media, BC-SiO$_2$ IO NPs and BC-STAR IO NPs, contain *GAB* cells, by-products, and HS media. Removal of the *GAB* cells and other impurities could not be performed as this would damage the iron oxide NPs. The standard method of purifying BC is a NaOH wash; however, the silica coating on the SiO$_2$ IO NPs is damaged by NaOH solutions. Removing bacterial cells and other impurities with acidic solutions would damage the uncoated iron oxide NPs such as STAR IO NPs. Therefore, lysozyme was investigated as a possible means to remove *GAB* cells. However, lysozyme was ineffective because although lysozyme is known to digest cell walls of Gram-negative bacteria, *Gluconacetobacter* is resistant to lysozyme.

Homogenization by blending and subsequent lyophilization were problematic. The samples could not actually be homogenized because the BC fibers could not be blended to a certain length. In addition, blending separated the entangled NPs from the BC fibers. The blending process resulted in a "slurry" of irregular-sized fibers, IO NPs, and DI water, and when placed in the magnetic separator, the IO NPs were caught up in the BC fibers as they interlaced, and pulled to the magnet. Nearby fibers connected to those fibers were also pulled to the magnet and therefore separated from the supernatant; this shows how the blending process is faulty, damaging the original composition of fibers with entangled NPs, and results in unreliable samples.

Furthermore, lyophilization caused NPs to be pulled out of the nanofibers to the surface of the blended samples when the water was removed by vacuum; in Figure 3.10 of a blended and lypophilized BC-SiO$_2$ IO NPs sample (b), the NPs are no longer entangled in the nanofibers as they had been after composite production in culture media as shown in Figure 3.11. Iron oxide NPs that were physically entangled in the fibers can be removed under harsh conditions such as blending and lyophilization, and results in unreliable samples.

Figure 3.11: FESEM image of the BC nanofibers with SiO_2 IO NPs and *GAB* cells entangled inside the nanofiber network after composite production in the culture media.
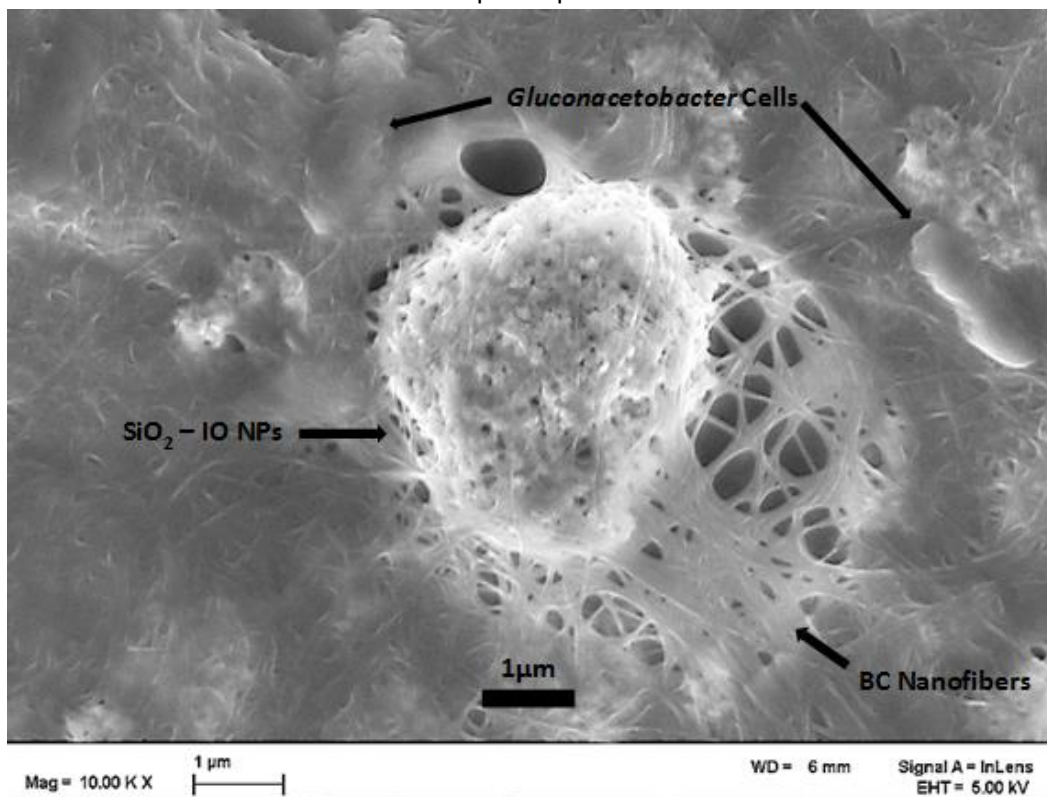
Figure 3.12: FESEM image of NaOH-cleaned BC nanofibers forming a porous matrix
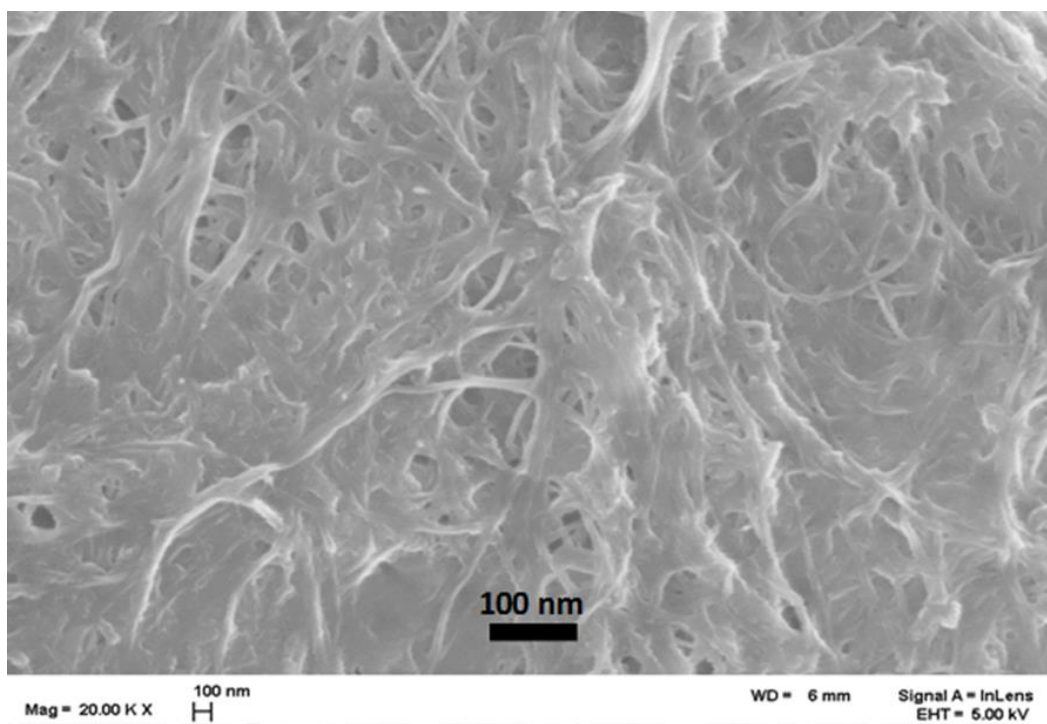
3.4 Results of Production of IO NPs (syn) and BC-IO NPs (syn) Composites

3.4.1 Results of Co-precipitation Production of BC-IO NP (syn) Composites

      Producing BC-IO NP composites in static and agitated culture media inoculated with *GAB* cells augmented with iron oxide NPs was problematic, for several reasons. Most notably, cellulose production by *GAB* was suppressed or stopped in some static and agitated samples, possibly due to the mutation of *GAB* cells into cellulose non-producers in some cases such as agitated cultures, in others, the presence of the iron NPs in the media may have caused toxicity affecting *GAB* cellulose production, or *GAB* cell death. Indeed, culture conditions during production of the BC-SiO$_2$ IO NP and BC-STAR IO NP composites affected BC growth. Agitated cultures often resulted in the absence of BC, and varying the concentration of NPs in the growth media affected BC production; for example, in too high concentrations of STAR IO NPs, BC was not produced.

      In addition, the SiO$_2$-IO NPs and STAR IO NPs were not actually nanoscale—these NPs were either already aggregated, or aggregated in the aqueous media; therefore, this method is not appropriate if nanomaterials are desired. To achieve nanomaterials, methods to prevent aggregation and maintain the nanoscale aspect of iron oxide NPs would need to be implemented.

      Furthermore, dispersion of iron oxide NPs in the growth media was poor in composites fabricated in the culture media during BC biosynthesis. If the augmented growth media method for producing BC-iron oxide composites will be used in the future, it is important to control the dispersion of NPs so that that nanocomposites can be homogeneous and the processes reproducible. Methods for preventing aggregation and evenly distributing the NPs needs to be implemented to achieve nanomaterials. Other researchers have developed methods for dispersing NPs such as sonication during BC biogenesis, which can be problematic as sonication can affect *GAB* cells; other methods for obtaining colloidal stability of NPs in aqueous solutions include dispersion materials or molecules.

      Another drawback of producing BC-IO NPs composites during BC biosynthesis in the culture media is the presence of *Gluconacetobacter* cells, by-products, and the HS media which would need to be removed in order to have a product that contains only BC and iron oxide NPs. Removal of the *GAB* cells and other impurities is impossible to accomplish without damaging the iron oxide NPs. The standard method of purifying BC is a NaOH wash; however, the silica coating on the SiO$_2$-IO NPs is damaged by NaOH solutions. Removing bacterial cells and other impurities with acidic solutions would damage iron oxide NPs such as STAR IO NPs and uncoated iron oxide NPs. While lysozyme is known to digest cell walls of Gram-negative bacteria, *Gluconacetobacter* is resistant to this

treatment. Currently, no method exists for removing impurities from the BC-IO NPs composites produced during BC biosynthesis in the culture media.

The formation of Fe_3O_4 with high crystallinity and magnetization can be enabled by conducting reverse co-precipitation synthesis at RT, using concentrated ammonia solutions, and combining the reaction precursors rapidly to minimize the oxygen present. Thus reverse co-precipitation using ammonia was used for synthesizing magnetite NPs. NH_3 gas-enhanced in situ co-precipitation was also conducted. However, oxygen was still present during the reverse co-precipitation and NH_3 gas-enhanced in situ co-precipitation methods used in this study, and as a result, γ-Fe_2O_3 formed in addition to Fe_3O_4 for the former, and γ-Fe_2O_3, α-Fe_2O_3, and FeO(OH) formed in the latter, as revealed in Figure 3.18 and Table 3.2 which discussed in section 3.5 on X-ray diffraction results. In addition, concentrated NH_3 causes cellulose to become more crystalline, as revealed by XRD, and a more crystalline material might be more brittle—NH_3 gas might be more gentle on the cellulose structure than concentrated aqueous NH_3; however, the properties of the BC-IO NP composites were not tested.

3.4.2 FESEM Results for BC-IO NP (syn) Composites

BC-Iron Oxide nanocomposites were fabricated by synthesizing and depositing iron oxide NPs on purified BC nanofibers in pellicles like the one in Figure 3.12. The BC-IO NP (syn) sample made from the 1 mol/L Fe^{3+}: Fe^{2+} solution was analyzed with FESEM which revealed that the BC nanofiber surfaces were uniformly coated with roundish IO NPs (syn) about 5-10 nm in size, as shown in Figure 3.13 with open areas between fibers, clear and unblocked by NPs. IO NPs that were not associated with the BC nanofibers aggregated into clusters; a few agglomerations of aggregated NPs appeared, but were not prevalent. The BC nanofibers prevent aggregation and effectively disperse the IO NPs (syn).

FESEM shows the localization of the IO NPs (syn) along the cellulose fibers and along smaller fibers in bundles or ribbons, which implies that the nanofibers may act as nucleation sites for crystal growth. BC fibers may limit the particle size of iron oxide and prevent aggregation, and maintain a porous structure.

Figure 3.13: FESEM image of the BC-IO NPs (syn) sample showing iron oxide NPs coating the BC fibers after co-precipitation using 1 mol/L Fe^{3+}: Fe^{2+} solution and NH_3.
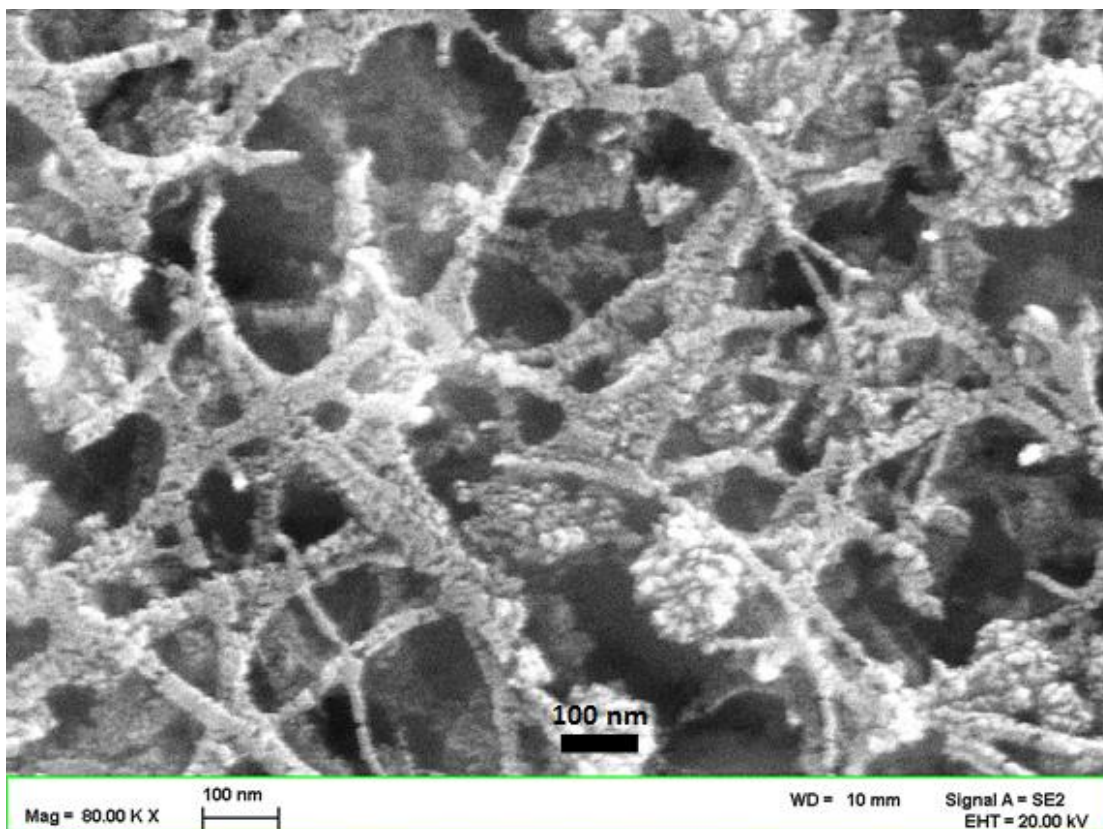
The BC-IO NPs (syn) nanocomposites were sonicated in DI H_2O for several washes. Sonication has been known to cause NP removal; however, in this case, the IO NPs remained attached to the surfaces of the BC nanofibers after the successive sonication washes. Because the NPs remain attached to the BC nanofibers, it is likely a bonding phase exists at the interface between the fibers and the IO NPs (syn). The close association of the coated IO NP (syn) with BC fibers likely enables interactions such as hydrogen bonding between the hydroxyl groups of cellulose and the hydroxyl groups on the iron oxide NP surface. The possible hydrogen bonding of the cellulose hydroxyl ions with the oxygen atoms on the surface of iron oxide nanoparticles is schematically represented in Figure 3.14. The high surface area of the BC nanofibers should provide numerous nucleation sites for the precipitation of iron oxide NPs. The iron oxide NPs are expected to be in close proximity to the hydroxyl groups on the fiber surfaces and therefore form hydrogen bonds. The surfaces of the iron oxide NPs have hydroxyl groups which may hydrogen bond with the hydroxyl groups of BC or with surrounding iron oxide NPs. The BC nanofiber network in which iron oxide is precipitated and the

hydrogen bonding between the fibers and the iron oxide NPs are expected to immobilize the NPs and thus prevent NP aggregation.

Figure 3.14: Schematic diagram showing possible hydrogen bonding of the hydroxyl (OH) groups on the cellulose molecule with surface oxygen atoms of the iron oxide nanoparticles such as Fe_3O_4 magnetite
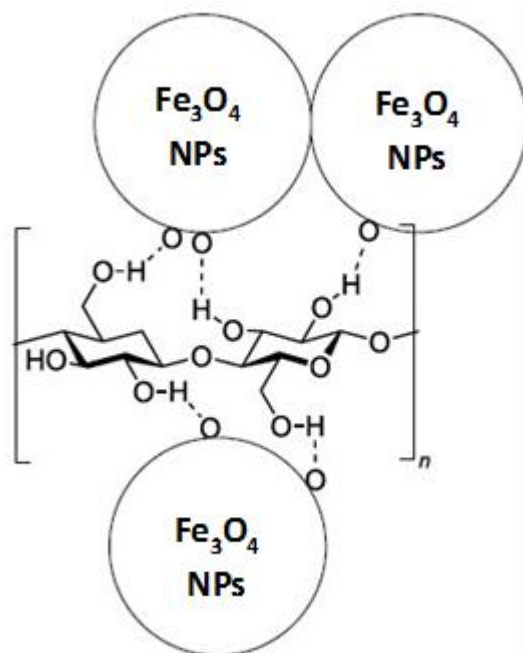
3.4.3 Transmission Electron Microscopy (TEM) Results for BC-IO NP (syn) Composite

TEM was used to try to obtain a better view of the IO NPs (syn) and their physical relationship with BC nanofibers. For TEM analysis of IO NPs (syn) synthesis on BC nanofibers, composite samples were produced from powdered BC (with a maximum size of 250 μm) soaked in 0.1M Fe^{3+}/Fe^{2+} iron ion bath for 24 hours, centrifuged, and combined with 28-30% NH_3 to try to synthesize iron oxide nanoparticles inside the cellulose and examine by TEM.

The TEM image in Figure 3.15 (a) shows that the IO NPs (syn) precipitated on the shortened BC nanofibers and also aggregated into larger masses when not associated with the BC nanofibers. This suggests that the fibers may act as nucleation sites for IO NP crystal growth, and may help prevent aggregation by providing precipitation sites. The smaller IO NPs (syn) may be around 25-50 nm in (a), and around 50-100 nm in (b); the IO NPs (syn) also appear in larger sizes.

Figure 3.15 TEM images of BC-IO NP (syn) composite—powdered BC soaked in 0.1M Fe^{3+}/Fe^{2+} showing IO NPs (syn) coating BC nanofibers and in aggregations.
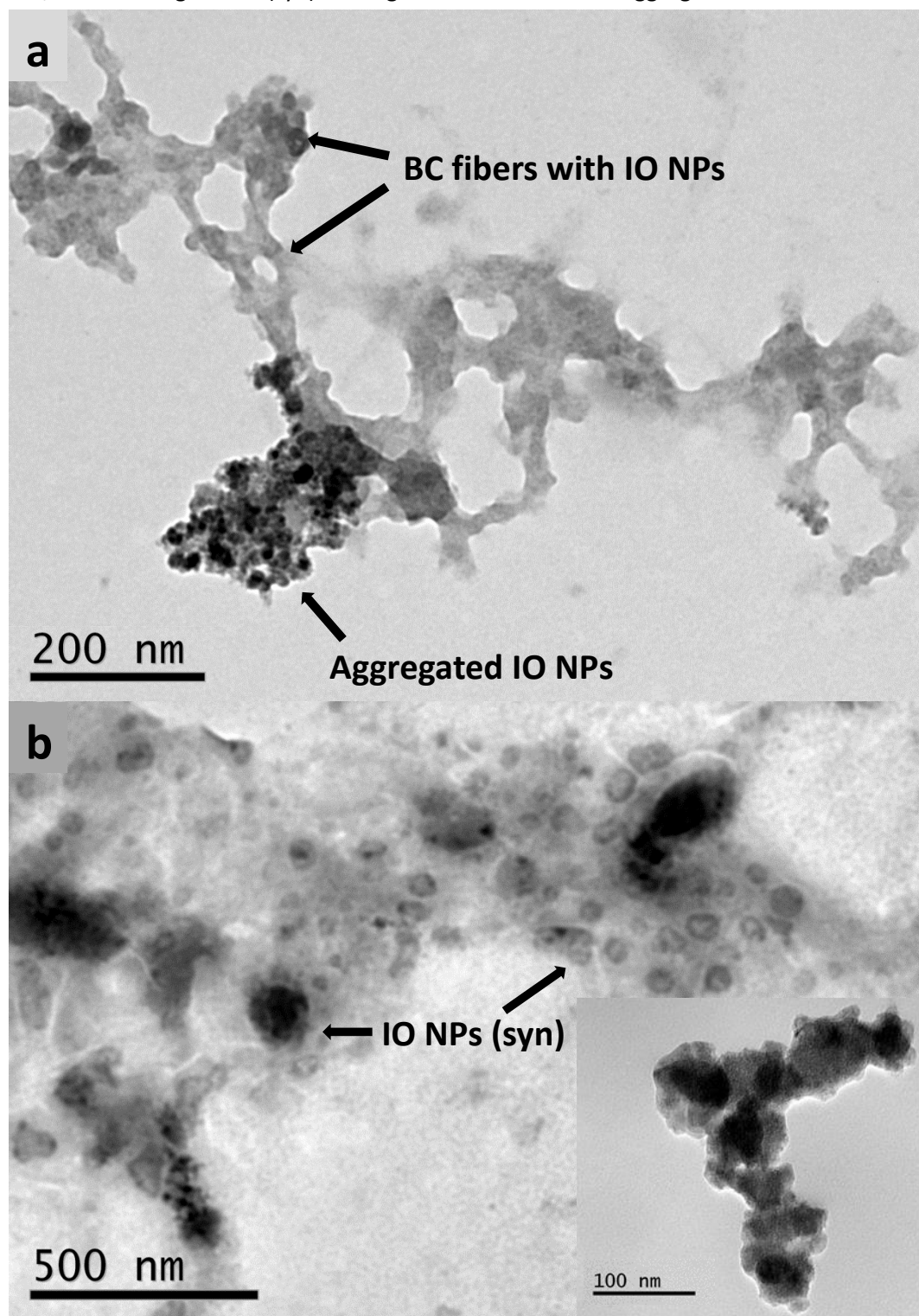
3.4.4 Energy Dispersive Spectrometry (EDX) Results for BC-IO NP (syn) composite

The energy-dispersive spectrometry (EDX) results in Figure 3.16 reveals the peaks for carbon, oxygen, and iron from the samples, and gold remaining on the samples after FESEM. EDX displayed the elements which confirmed that the NPs synthesized on the bacterial cellulose fibers were composed of iron oxides which contain iron (Fe) and oxygen (O) atoms. BC contains carbon (C) and oxygen (O) atoms.

Figure 3.16 EDX displaying the elements in both the BC- IO NP (syn) composite and the BC sample to confirm the former contains Fe, O, and C atoms and the latter contains C and O atoms.
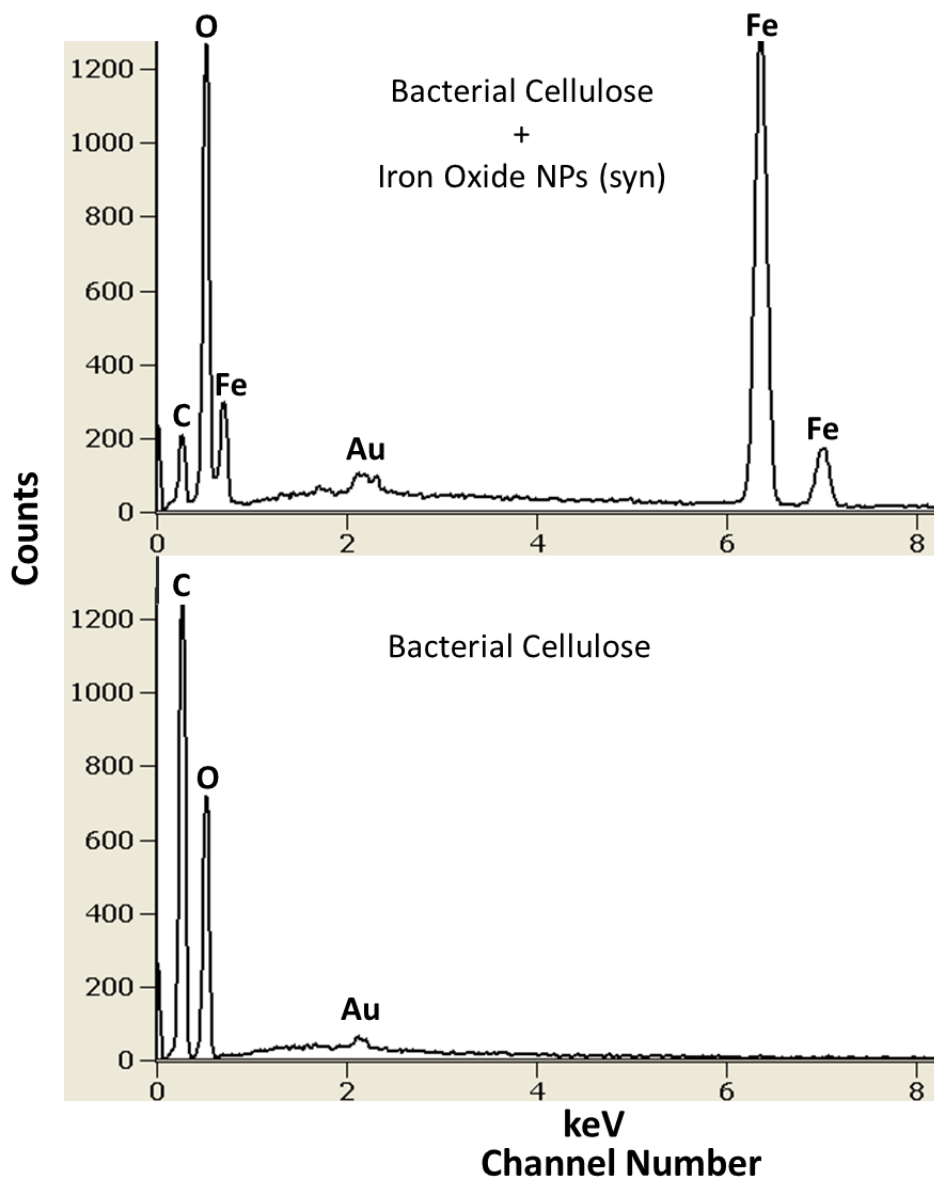
3.4.5 Mass Loading of Synthesized Iron Oxide NPs in BC-IO NP (syn) Composites

BC-IO NP (syn) composite samples with a range of IO NPs (syn) concentrations were engineered by using different Fe^{3+}/Fe^{2+} solution concentrations—0.01, 0.1, and 1 mol/L—which resulted in the percent of mass loading values of 1.1, 12.4 and 29.2 (averaged from three separate samples) respectively, as presented in Figure 3.17 and Table 3.1. Both BC-IO NPs (syn) samples (c) and (e) of Figure 3.18 used 1 mol/L concentration precursor solutions for synthesizing IO NPs and resulted in similar mass loadings 27.4% and 34.8%, respectively; the only difference was that NH_3 vapors passed through the sample (c) whereas the latter sample (e) was dipped in liquid NH_3 .

Figure 3.17 Mass loading of synthesized iron oxide NPs in BC-IO NP (syn) composites at 1 mol/L, 0.1 mol/L, and 0.01 mol/L concentrations.
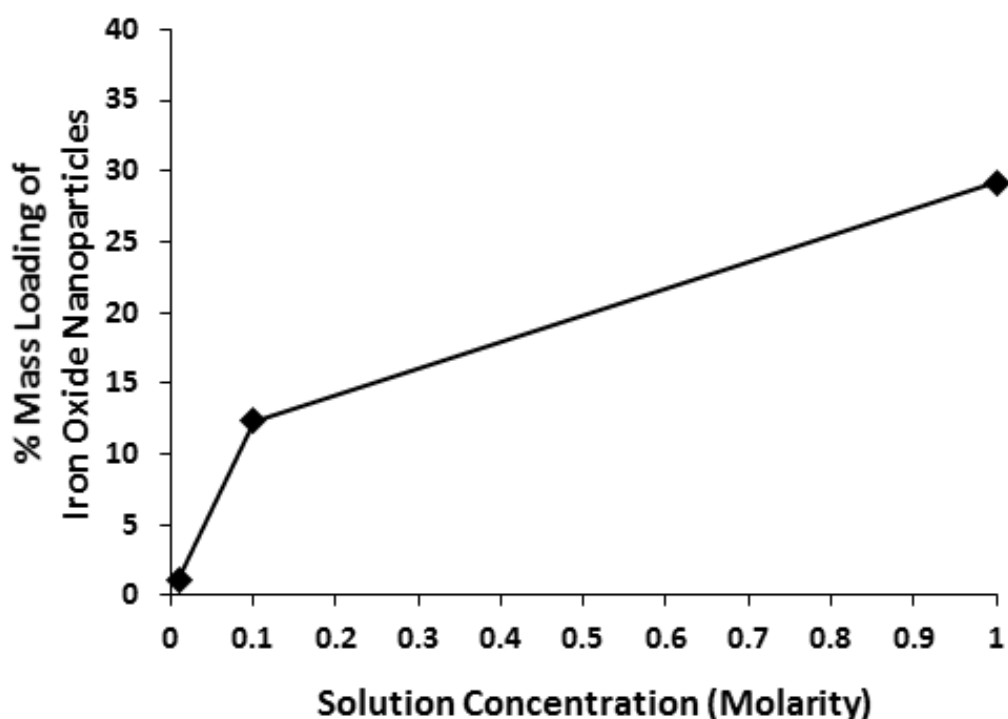
Table 3.1: Mass Loading of IO NPs (syn) in Iron Ion Concentrations 1mol/L, 0.1mol/L, and 0.01mol/L in the BC matrix of the BC-IONP(syn) Nanocomposites	
Concentration Iron Ions in Molarity M	% Mass Loading Fe_3O_4 NPs
0.01	1.1
0.1	12.4
1	29.2

3.5 X-ray Diffraction (XRD) Results

X-ray Diffraction was used to analyze select samples' crystal structures in order to identify the crystalline phases present and to investigate how the cellulose and iron oxide materials were affected by conditions and interacted as composites. The crystal structure (the unit cell and Bravais lattice parameters) and the degree of crystallinity can vary with chemical composition, treatments, and other factors which cause structural stresses. For example, XRD may reveal information about how the crystal structure of BC is affected by the presence of IO NPs.

XRD was conducted on select samples, for several reasons. In the case of the composite samples produced by addition of iron oxide NPs to static and agitated cultures, namely BC-SiO$_2$ IO NPs and BC-STAR NPs, there was not enough material produced in order to enable XRD analysis. Furthermore, the presence of GAB cells in BC materials caused interference with analysis XRD reflections and made diffraction peaks imperceptible. When preparatory test XRD runs were conducted on the BC-iron oxide composites formed by iron oxide synthesis in the BC matrix, BC-IO NPs (syn), the iron oxide components were not always observable. When XRD was conducted on the BC-IO NPs (syn) composites, the diffraction peaks of the IO NPs (syn) were discernible in the samples produced from 1 mol/L iron ion solutions, whereas iron oxide diffraction peaks were imperceptible in the samples produced from 0.1 mol/L and 0.01 mol/L iron ion solutions. These results are consistent with the findings of other researchers that IO NPs (syn) diffraction peaks only appear in BC-iron oxide composites treated with iron ion concentrations above 0.1 mol/L. For this reason, only the BC-IO NPs (syn) composites from 1 mol/L solutions were fully analyzed with XRD and used as the representative samples of BC-iron oxide composites for comparison to other samples. The XRD diffractograms suggest that the composite sample (c) may have had more IO NPs (syn) on the surface of the sample in the area penetrated by the x-rays which affected the XRD results.

The XRD diffractograms of select samples are compared in Figures 3.18 and 3.19 and Table 3.2: BC, ammonia-treated BC, synthesized iron oxide nanoparticles IO NPs (syn), and the BC-iron oxide composites BC-IO NPs (syn) fabricated using both reverse co-precipitation and NH$_3$ gas-enhanced in situ co-precipitation. The XRD patterns were evaluated using the Bragg equation to determine the d-spacings (the distance between the planes of atoms in the crystal structure) and

Figure 3.18: Normalized XRD Diffraction Patterns for the BC, NH$_3$-treated BC, IO NPs (syn), and the BC-IO NPs (syn) composites formed by both reverse co-precipitation and NH$_3$ gas-enhanced in situ co-precipitation with prominent peaks attributed to BC or iron oxide components.
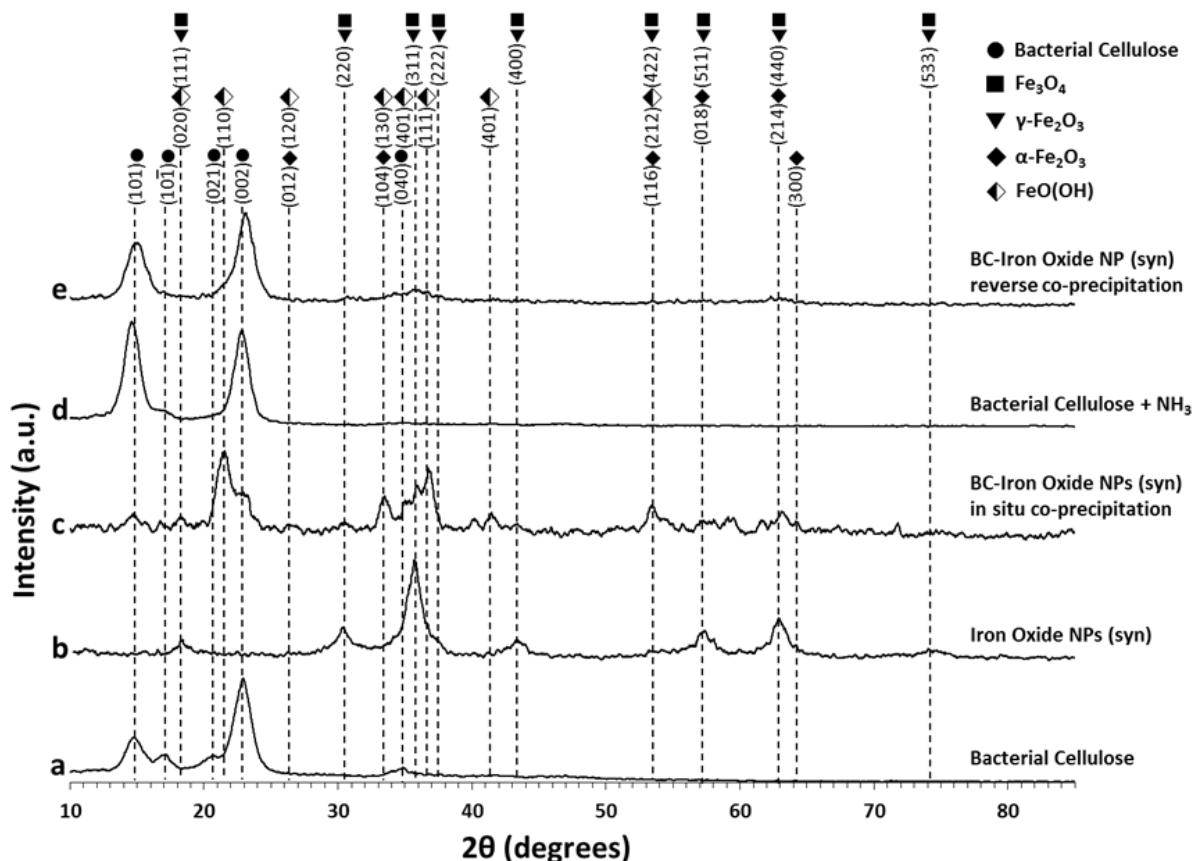
Miller *hkl* indices belonging to the most intensive diffraction peaks. The d values, calculated from the position of diffraction peaks and the corresponding Miller indices, define the crystalline phases present in the samples. Figure 3.18 notates the Miller indices of the samples' prominent diffraction peaks, which are attributed to cellulose and types of iron oxide, and 3.2 notates the prominent peaks' Miller indices, angle of diffraction 2θ, and d-spacings from the XRD diffractograms of select samples and ICDD standards.

Figure 3.18 depicts normalized XRD patterns for the BC, NH$_3$-treated BC, IO NPs (syn), and the BC-IO NPs (syn) composites formed by both reverse co-precipitation and NH$_3$ gas-enhanced in situ co-precipitation. The diffractograms of the samples were normalized in order to visualize the XRD peaks better for comparison, especially because the IO NPs in the samples produce low-intensity peaks which are difficult to perceive; for example, in the diffractograms of the composite samples in

Figure 3.19. Normalization helped improve visualization in the samples with low-intensity peaks such as the BC-IO NPs (syn) composites (b) and (c) in Figure 3.18. As a result, in the normalized XRD patterns the peaks of the iron oxide NPs (b) and (c) and the BC peaks in the composite sample (e) are exaggerated and appear much larger than they actually are—they look about the same size as the BC peaks in samples (a) and (d), but in actuality they are not, as shown in Figure 3.19. However, even with normalization the IO NPs (syn) peaks in the BC-IO NPs (syn) samples (e) are still difficult to discern in the diffractogram in Figure 3.18 because they are so small in relationship to the high-intensity BC peaks.

Figure 3.19 : XRD Diffraction Patterns for BC, NH_3-treated BC, IO NPs (syn), and the BC-IO NPs (syn) composites formed by both reverse co-precipitation and NH_3 gas-enhanced in situ co-precipitation.

Table 3.2: XRD peaks' Miller indices, 2θ, and d-spacings for select samples and ICDD standards—BC, NH$_3$-treated BC, IO NPs (syn), and BC-IO NPs (syn) composites formed by both (a) reverse co-precipitation and (b) NH$_3$ gas-enhanced in situ co-precipitation—as well as the ICDD's 2θ and d-spacings of the corresponding peaks of Fe$_3$O$_4$, γ-Fe$_2$O$_3$, α-Fe$_2$O$_3$ and FeO(OH), which may be present in some samples in this research .

Miller indices (*hkl*) of (1)(2)(3)	BC (1) 2θ	d	BC + NH$_3$ 2θ	d	IO NPs (syn) reverse co-precip 2θ	d	BC-IO NPs(syn) reverse co-precip (a) 2θ	d	BC-IO NPs(syn) in situ co-precip (b) 2θ	d	Fe$_3$O$_4$ ICDD (2) 2θ	d	γ-Fe$_2$O$_3$ ICDD (3) 2θ	d	α-Fe$_2$O$_3$ ICDD (4) (*hkl*)(4)	2θ	d	FeO(OH) ICDD (5) (*hkl*)(5)	2θ	d
(101)	14.7	6.03	14.5	6.05			14.8	5.97	14.7	6.03										
(10$\bar{1}$)	17.0	5.22	16.2	5.25																
(111)					18.2	4.85	18.3	4.85	18.1	4.90	18.3	4.84	18.4	4.84				(020)	18	4.96
(021)	20.4	4.35																		
									21.4	4.15								(110)	21.6	4.18
(002)	22.8	3.90	22.7	3.89			23.0	3.86	23.2	3.83										
									26.3	3.38			24.2	3.68	(012)	24	3.68	(120)	26.6	3.36
(220)					30.2	2.95	30.5	2.92	30.2	2.96	30.1	2.97	30.3	2.95						
									33	2.69			33.3	2.69	(104)	33	2.70	(130)	33	2.67
(040)	34.3	2.62					34.1	2.63												
(311)					35.6	2.52	35.7	2.51	35.7	2.51	35.7	2.51	35.7	2.51	(110)	36	2.59	(021)	35	2.57
(222)					37.3	2.41			36.7	2.45	37	2.42						(111)	36.7	2.45
									41.5	2.19								(401)	41.1	2.19
(400)					43.3	2.00					43.1	2.10	43.3	2.09	(113)	43	2.21			
(422)					53.1	1.72			53.5	1.72	53.3	1.72	53.6	1.72	(116)	54	1.69	(212)	53.5	1.71
(511)					57.2	1.61	57.2	1.61			56.9	1.62	57.3	1.61	(018)	57	1.59			
(440)					62.8	1.48	62.6	1.48	63.1	1.47	62.5	1.49	62.8	1.40	(214)	63	1.49			
(533)					73.9	1.28					73.9	1.28	74.3	1.28						

Iron oxides are crystalline, and cellulose has both crystalline and amorphous parts. Each crystalline substance (phase) shows a unique XRD pattern; therefore, in a mixture of substances, each produces an XRD pattern independently of the others. The crystalline phases in the materials were identified using XRD in order to determine the composition. The XRD diffraction peaks were indexed using ICDD standards. The BC XRD peaks and data aligned to the ICDD standard for native cellulose (crystalline cellulose I). The IO NPs (syn) XRD peaks aligned to those of the ICDD standards

for the iron oxides Fe_3O_4 and γ-Fe_2O_3. Thus, the XRD patterns and data for BC and the IO NPs (syn) were used as standards for comparison to the two types of BC-IO NPs (syn) composites.

Table 3.3 Crystallinity index (CI), crystallite size (CS), and interchain separation length (ISL) of BC and BC-IO NPs (sym) nanocomposites.			
Sample Types	CI (%)	CS (nm)	ISL (nm)
BC	87.6	6.4	4.3
BC + silica-coated iron oxide BC-SiO_2 IO NPs	80	6.3	4.9
BC + synthesized iron oxide BC-IO NPs (syn)	79	8	5.2

Table 3.2 lists the prominent XRD peaks and the assigned Miller indices, 2θ (in degrees) and d-spacings (in Angstroms) from the XRD diffractograms of select samples in Figure 3.18— BC, ammonia-treated BC, synthesized iron oxide nanoparticles IO NPs (syn), and BC-IO NPs (syn) composites formed by both reverse co-precip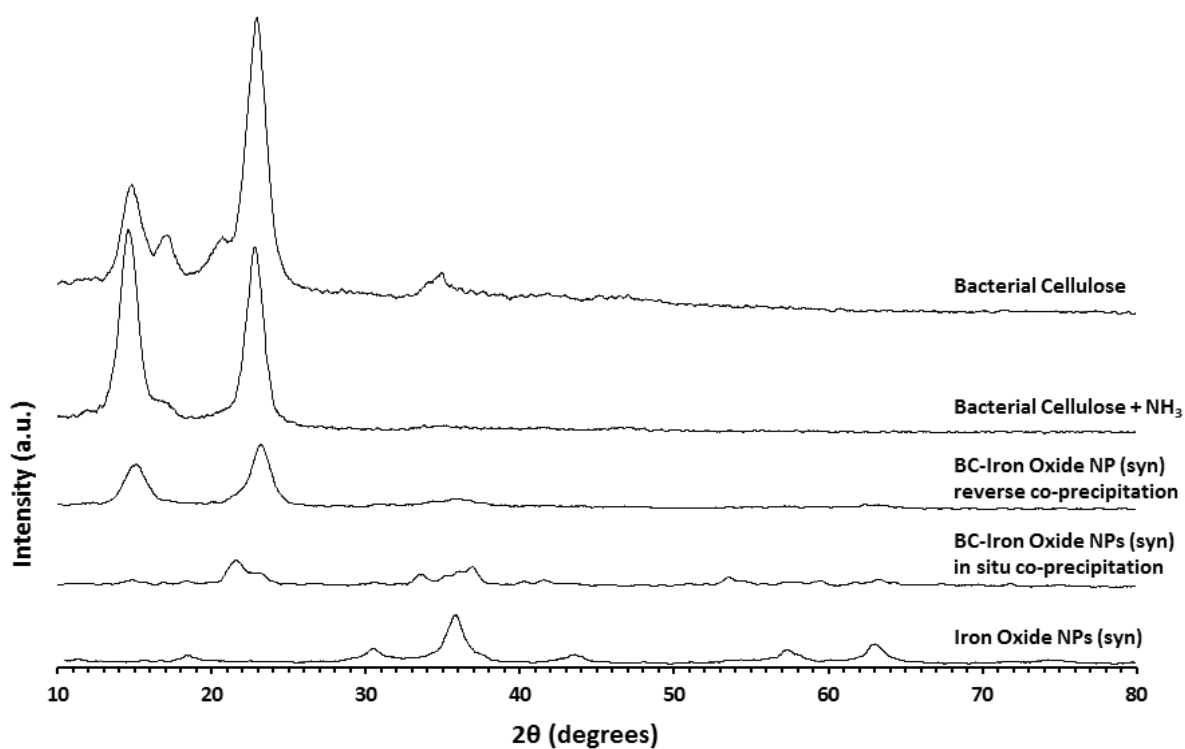itation (a) and NH_3 gas-enhanced in situ co-precipitation (b)—as well as the ICDD's 2θ and d-spacings of the corresponding peaks of the iron oxides Fe_3O_4 (2), γ-Fe_2O_3 (3), α-Fe_2O_3 (4), and FeO(OH) (5), which may be present in some of the samples in this research. In Table 3.2, the first column lists the assigned Miller indices (*hkl*) for BC (1), Fe_3O_4 (2), and γ-Fe_2O_3 (3), and the Miller indices for the XRD peaks of α-Fe_2O_3 (4), and FeO(OH) (5) are found in the leftmost sub-column of the main column for each iron oxide.

The XRD pattern for BC corresponds to the ICDD standard for native cellulose, composed of crystalline cellulose I. The five characteristic XRD peaks of crystalline cellulose I observable in BC are assigned to the Miller indices (101), ($10\bar{1}$), (021), (002) and (040) located at as notated in both Figure 3.18 and Table 3.2. The cellulose peaks with the greatest intensity are (101) and (002); these peaks were observable in all the samples containing BC, whereas the lower-intensity peaks were often indiscernible in the XRD diffractograms for BC and the BC-IO NPs (syn) composites.

Because ammonia was used in the co-precipitation of iron oxide NPs in the composites, BC was treated with ammonia for comparison to the composite samples. Treating BC with concentrated 28-30% ammonia affects the crystal structure of BC, as seen in Figure 3.18: the (021) and (040) peaks disappear in both the NH_3-treated BC sample (d) and the BC-IO NPs (syn) sample formed by reverse co-precipitation (e), and the ($10\bar{1}$) peak diminishes in intensity (or becomes more amorphous) in the NH_3-treated BC and disappears altogether in composite sample (e). The greatest change in the NH_3-treated BC is the large peak which formed in the 14.7° region of the diffractogram where the (101) peak of BC is located, as depicted in Figure 3.19; this peak could be the result of the (101) peak increasing in intensity due to more (101) crystal planes forming and thereby increasing crystallinity in

this orientation. In addition, the (002) peak decreased in intensity for the NH$_3$-treated BC sample compared to BC.

Compared to the NH$_3$-treated BC sample, the BC-IO NPs (syn) reverse co-precipitation sample's (101) and (002) peaks diminished in intensity even more. Moreover, in the BC-IO NPs (syn) NH$_3$ gas-enhanced in situ co-precipitation sample, all cellulose peaks have greatly diminished in intensity (and possibly broadened) and are nearly indistinguishable in the XRD diffractogram, as seen in Figure 3.19. Furthermore, the diminished cellulose peak at (002) is obscured by a peak attributed FeO(OH) at 41.1° and the Miller index (110) in the in situ co-precipitation composite sample (b) as notated in Table 3.2.

The synthesis of IO NPs in the BC matrix causes the XRD peaks of cellulose, noticeably (101) and (002), to decrease in height as shown in Figure 3.19. In XRD, a decrease in diffraction peak height can be related to the change in crystallinity of the samples or a change in the composition of the material. Variations in intensity are known to be related to variations in the scattering intensity of the components of the crystal structure and their arrangement in the lattice. Broadening of XRD peaks can also indicate that non-uniform strain on the crystal structure has occurred. The broadening and disappearance of cellulose peaks in the diffractograms of the BC-IO NPs (syn) samples might be a result of non-uniform strains on the crystal structure of cellulose and a reduction in cellulose crystallinity—a change in ISL and CI, respectively, as shown in Table 3.3. In addition, a decrease in peak height may mean that more x-ray absorbing material exists in the path of the x-ray beam. This may be the case in this research, because in the BC-IO NPs (syn) samples the IO NPs are visible as a coating on the BC fibers as shown in Figure 3.13; moreover, in the composite sample produced by the NH$_3$ gas-enhanced in situ co-precipitation method (c) the IO NPs (syn) are encrusted on the BC fibers at the surface of the BC pellicle, as visible to the human eye. The XRD diffractogram of the composite sample (c) in Figures 3.18 and 3.19 show either peak extinctions or extremely reduced peak intensities for the (101), (10$\bar{1}$), (021), (002) and (040) cellulose peaks. A heavy coating of IO NPs (syn) on the fibers of the in-situ co-precipitation sample (c) may have changed the composite composition so that more iron oxide was present than cellulose in the areas penetrated by x-rays, thus causing the x-rays to diffract mostly on the iron oxide lattice planes.

The XRD patterns of Fe$_3$O$_4$ and γ-Fe$_2$O$_3$ are nearly the same due to their similar cubic crystal structure with a cubic close-packed array of oxide ions. The main XRD peaks—crystal lattice reflection planes—of both Fe$_3$O$_4$ and γ-Fe$_2$O$_3$ are notated by the Miller indices (111), (220), (311), (400), (422), (511), (440), and (533). Identification of coexisting Fe$_3$O$_4$ and γ-Fe$_2$O$_3$ phases is difficult

due to their overlapping peaks. Therefore, it is difficult to conclude from XRD alone which type of iron oxide exists in the samples of this research containing IO NPs (syn). The main peaks for Fe_3O_4 and γ-Fe_2O_3 are observable in most of the XRD diffractograms of the samples containing iron oxides as presented in Figures 3.18 and 3.19 and Table 3.2.

XRD analysis indicates that the IO NPs (syn) sample is composed of Fe_3O_4, or both Fe_3O_4 and γ-Fe_2O_3, because the sample's diffraction peaks have the 2θ/d-spacing values of 18.2°/4.85 Å, 30.2°/2.95 Å, 35.6°/2.52 Å, 37.3°/2.41 Å, 43.3°/2.00 Å, 53.1°/1.72 Å, 57.2°/1.61 Å, 62.8°/1.48 Å, and 73.9°/1.28 Å which correspond to the ICDD 2θ/d-spacing values of Fe_3O_4, or both Fe_3O_4 and γ-Fe_2O_3: 18.3°/4.84 Å for (111), 30.1°/2.97 Å and 30.3°/2.95 Å for (220), 35.7°/2.51 Å for (311), 37°/2.42 Å for (422), 43.1°/2.10 Å and 43.3°/2.09 Å for (400), 53.3°/1.72 Å and 53.6°/1.72 Å for (422), 56.9°/1.62 Å and 57.3°/1.61 Å for (511), 62.5°/1.49 Å and 62.8°/1.40 Å for (440), and 73.9°/1.28 Å and 74.3°/1.28 Å for (533), as notated in Table 3.2.

In the XRD pattern of the IO NPs (syn) sample, the peaks located at 18.2°, 30.2°, 35.6°, 53.1°, 57.2°, 62.8°, and 73.9° which correspond to the seven most intense peaks of both the Fe_3O_4 and γ-Fe_2O_3 ICDD diffractograms assigned to the Miller indices (111), (220), (311), (422), (511) and (440), respectively, were observed; however, the XRD (422) peak around 37°, which is attributed to Fe_3O_4, is obscured by the wide base of the (311) peak, and the peaks around 53° for (422) and 74° for (511) were barely discernible in the diffractogram of the IO NPs (syn) sample even after normalization, as shown in Figures 3.18 and 3.19. As NPs reduce in size, their XRD peaks become broader and the intensity decreases. Broad diffraction peaks with low intensity may be a result of either the small size of grains (crystallites), or poor crystallization (crystals randomly arranged or with low degrees of periodicity). It is well known that as NPs and crystallites decrease in size, the XRD peaks broaden in width and decrease in height (the intensity decreases). The XRD peaks of the synthesized iron oxide NPs in Figure 3.19 are broad rather than narrow, and short—low in intensity.

Other types of iron oxide which may result from the iron oxide synthesis reaction such as α-Fe_2O_3 and FeO(OH) were most likely absent from the IO NPs (syn) sample because α-Fe_2O_3 lacks diffraction peaks around 18° (111), 30° (220) and 74° (533), and FeO(OH) lacks diffraction peaks around 43° (400), 57° (511), 62° (440) and 74° (533). Furthermore, the black color of the IO NPs (syn) sample supports the finding that mainly Fe_3O_4 was present because Fe_3O_4 is black in color whereas the other iron oxide types including γ-Fe_2O_3, α-Fe_2O_3, and FeO(OH) range in color from brown to reddish-brown to yellow-brown. Therefore, this reverse co-precipitation method for IO NPs (syn) caused mainly Fe_3O_4 to form rather than fully oxidizing into γ-Fe_2O_3.

XRD data indicates that the BC-IO NPs (syn) samples formed by reverse co-precipitation are composed of Fe_3O_4 and γ-Fe_2O_3 because the samples exhibited diffraction peaks which have the 2θ/d-spacing values of 18.3°/4.85 Å, 30.5°/2.92, 35.7°/2.51 Å, 57.2°/1.61 Å, and 62.6°/1.48 Å, corresponding to the Fe_3O_4 and γ-Fe_2O_3 ICDD 2θ/d-spacing values of 18.3°/4.84 Å for (111), 30.1°/2.97 Å and 30.3°/2.95 Å for (220), 35.7°/2.51 Å for (311), and 56.9°/1.62 Å and 57.3°/1.61 Å for (511), respectively, as notated in Table 3.2. The XRD peaks at approximately 43° for (400), 53° for (422), and 74° for (533) are not discernible in the diffraction pattern of the BC-IO NPs (syn) reverse co-precipitation sample. This is likely due to a low concentration of IO NPs (syn) in the BC matrix.

A difference in the XRD patterns of IO NP (syn)-containing samples can be observed when comparing the BC-IO NP (syn) diffractogram of the NH_3 gas-enhanced in situ co-precipitation sample (c) to that of the reverse co-precipitation sample IO NPs (syn) (b) and BC-IO NPs (syn) (e) shown in Figure 3.18. Some peaks disappeared and additional peaks appeared in sample (c), which indicates a change in the crystalline phases and/or crystal structure; in other words, the chemical composition of the IO NPs (syn) formed in the BC matrix by the NH_3 gas-enhanced in situ co-precipitation was different than the IO NPs (syn) formed by reverse co-precipitation in aqueous NH_3. A cluster of peaks in sample (c), including several peaks attributed to FeO(OH), occur in the peak range 32°-38°, in contrast to the IO NPs (syn) sample (b) in which the single peak corresponding to Fe_3O_4 or γ-Fe_2O_3 occurs around 35.6°, as shown in Figure 3.18. In sample (c), this γ-Fe_2O_3 peak becomes much smaller and appears obscured by peak at 36.7° attributed to FeO(OH).

XRD data indicates that the BC-IO NPs (syn) NH_3 gas-enhanced in situ co-precipitation sample is composed mostly of FeO(OH) and γ-Fe_2O_3 because the 2θ/d-spacing values of the sample align best with these iron oxide phases. The sample's 2θ/d-spacing values of 18.1°/4.90 Å, 21.4°/4.15 Å, 26.3°/3.38 Å, 33°/2.69 Å, 35.7°/2.51 Å, 36.7°/2.45 Å, 41.5°/2.19 Å, and 53.5°/1.72 Å correspond to the FeO(OH) ICDD 2θ/d-spacing values of 18°/4.96 Å for (020), 21.6°/4.18 Å for (110), 26.6°/3.36 Å for (120), 33°/2.67 Å for (130), 35°/2.57 Å for (021), 36.7°/2.45 Å for (111), 41.1°/2.19 Å for (401), and 53.5°/1.71 Å for (212), respectively. The sample's 2θ/d-spacing values of 30.2°/2.96 Å, 33°/2.69 Å, 35.7°/2.51 Å, 53.5°/1.72 Å, and 63.1°/1.47 Å correspond to the γ-Fe_2O_3 2θ/d-spacing values of 30.3°/2.95 Å for (220), 35.7°/2.51 Å for (311), 53.6°/1.72 Å for (422), and 62.8°/1.40 Å for (440), respectively. However, the γ-Fe_2O_3 ICDD diffraction patterns at 43° for (400), and 74° for (533) are not discernible in the diffraction pattern of the the BC-IO NPs (syn) NH_3 gas-enhanced in situ co-precipitation sample. The sample's 2θ/d-spacing values of 26.3°/3.38 Å, 33°/2.69 Å, 35.7°/2.51 Å, 53.5°/1.72 Å, and 63.1°/1.47 Å might also correspond to the ICDD 2θ/d-spacing values for another

iron oxide phase, α-Fe$_2$O$_3$, with 24.2°/3.68 Å for (012), 33°/2.70 Å for (104), 36°/2.59 Å for (110), 54°/1.69 Å for (116), and 63°/1.49 Å for (214); however, only the peaks at 33° and 63° for α-Fe$_2$O$_3$ correspond closely to those in the sample, and many other peaks for α-Fe$_2$O$_3$ are absent in the sample as shown in Table 3.2. The fact that the sample's 2θ/d-spacing values align best to those of FeO(OH) and the existence of peaks at 21.6°, 33°, and 36.7° which do not exist in the IO NPs (syn) sample and which are attributed to FeO(OH) as shown in Figure 3.18 and Table 3.2 indicates that the BC-IO NPs (syn) NH$_3$ gas-enhanced in situ co-precipitation sample is composed mainly of FeO(OH).

3.6 Attenuated Total Reflection Fourier Transform Infrared (ATR-FTIR) Results

The absorption spectra of the cellulose composites showed IR bands for cellulose across the whole scanning region 4000-650 cm^{-1}. The high cellulose content compared to that of iron oxide caused the composite spectra to be dominated by the cellulose bands.

3.6.1 ATR-FTIR Characteristics of Cellulose and Overview of Samples Studied

ATR-FTIR measurements were conducted to examine the molecular structure of materials produced for this research including the bacteria *Gluconacetobacter* (*GAB*) which were present in some materials, the cellulose nanofibers derived from the bacteria (BC) and microcrystalline cellulose (MC) of plant origin obtained from scientific sources, and the non-cellulose nanomaterials used to form composites with bacterial cellulose: silica-coated iron oxide and iron oxide-coated zero-valent iron nanoparticle aggregates, SiO$_2$ IO NPs and STAR IO NPs respectively, and synthesized iron oxide nanoparticles IO NPs (syn), and the nanocomposites of the cellulose and iron oxide nanomaterials BC-SiO$_2$ IO NP-STAT, BC-SiO$_2$ IO NP-AGIT, BC-STAR IO NPS-STAT, and BC-IO NPs (syn).

ATR-FTIR spectroscopy was also used to investigate the interactions between the bacterial cellulose nanofibers and the iron oxide NPs by measuring composite samples of these materials including synthesized magnetite and/or maghemite nanoparticles (IO NPs), silica-coated iron oxide nanoparticles (SiO$_2$ IO NPs), and iron oxide-coated zero-valent iron nanoparticles (STAR IO NPs). Interpretations of the IR spectral molecular group frequencies of the various materials measured— celluloses, iron oxides, and composites—in the form of assignments to identified groups and corresponding cited references of common interpretations are summarized in Table 3.2 found at the end of the ATR-FTIR section.

The samples produced in static and agitated growth media were named accordingly with the endings -STAT or -AGIT. Samples that were cleaned with NaOH prior to ATR-FTIR are labeled (NaOH) in the Figures; however, in the text these samples are simply named MC, BC-STAT, and BC-AGIT

because they are the purified standards with which to compare the other samples containing *GAB*

cells or IO NPs. Samples that were washed only with DI water prior to ATR-FTIR are labeled (DI-H_2O)

in the Figures that refer to them; these samples still contain *GAB* cells. The BC samples washed with

DI H_2O are named BC-STAT-*GAB* and BC-AGIT-*GAB* to distinguish them from the NaOH-treated

samples (the standards) that contain only cellulose- impurities such as *GAB* cells are absent. The

composite samples named BC-SiO_2 IO NP-AGIT were produced as irregular masses and pellets. For

the STAR IO NPs, BC only grew in the static culture media, so only the composite material BC-STAR IO

NP-STAT was produced and examined by ATR-FTIR.

ATR-FTIR spectra in the wavenumber range 4000-650 cm^{-1} of the following sampled materials

are displayed in Figures 3.20 and 3.21. The samples include NaOH-treated microcrystalline cellulose

(MC) and bacterial cellulose (BC)—BC-STAT and BC-AGIT—all of which were used as a references for

comparisons to the composite samples, *GAB* cells, and *GAB* cell-containing bacterial cellulose (BC-

STAT-*GAB* and BC-AGIT-*GAB*), synthesized iron oxide nanoparticles IO NP(syn), silica-coated iron

oxide nanoparticles (SiO_2 IO NP), iron oxide-coated Fe^o nanoparticles (STAR IO NPs), and bacterial

cellulose-iron oxide nanoparticle composite samples BC-SiO_2 IO NP-STAT, BC-SiO_2 IO NP-AGIT, BC-

STAR-IO NP, and BC-IO NPs (syn).

The frequencies of the bands or peaks for the materials sampled lie within experimental

error from frequencies of similar materials measured by other researchers; in addition, slight peak

shifts around ± 10% are normal.[184,185]

The ATR-FTIR spectra of the samples were analyzed and results discussed for several regions

according to the existing molecular group vibrations as listed below:

● Region I: 3600-3200 cm^{-1}, 1640 cm^{-1}, and 700-300 cm^{-1} IR Frequency Regions:

 IR vibrational modes for hydrogen-bonded OH stretching (νOH) and water bending (δHOH)

● Region II: 3000-2700 cm^{-1} IR Frequency Region:

 CH stretching (νCH) vibration bands (CH, CH_2 and CH_3 aliphatic groups)

● Region III: 1700-1200 cm^{-1} IR Frequency Region:

 Amide I (νC=O), II (δNH), and III (νC-N) bands

● Region IV: 1500-1250 cm^{-1} IR Frequency Region:

 CH deformation, or bending--δCH_2 (sym) and δCH_3 (sym)

● Region V: 1255-650 cm^{-1} IR Frequency Region:

 COH bending (δCOH), COC stretching (νCOC) CO stretch (νCO) , and Si-OH, Si-O, Fe-O, Fe-O-Fe.

Figure 3.20: IR spectra for *GAB* cells, IO NP (syn), BC- IO NP (syn), and BC and MC (NaOH treated)
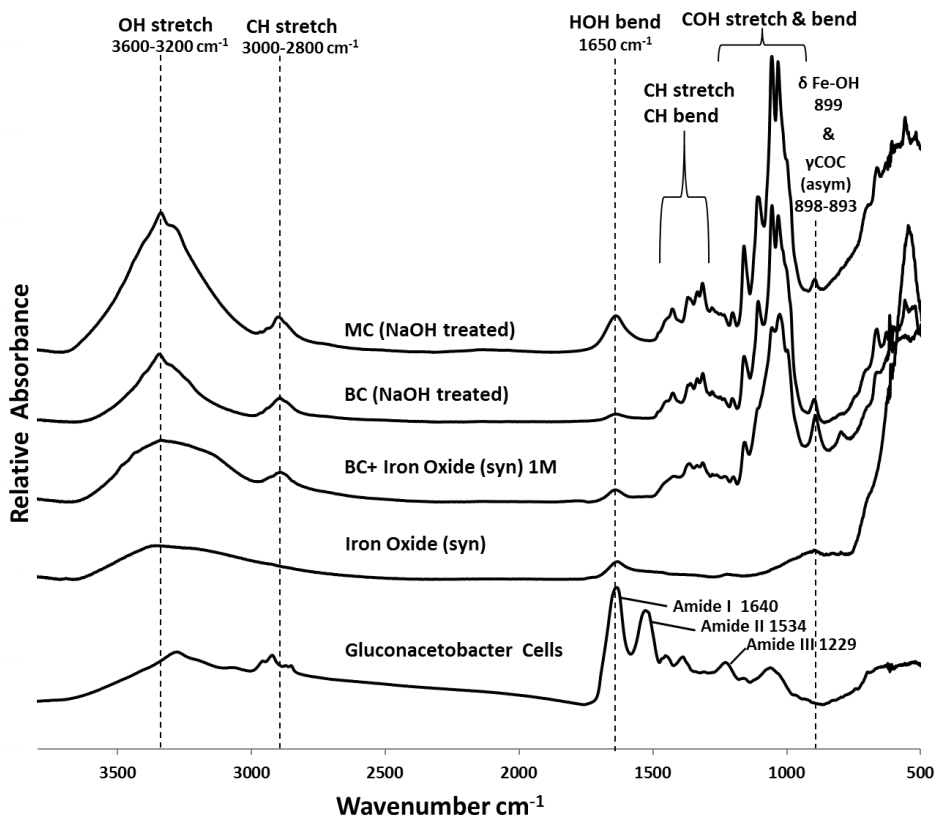
Figure 3.21: IR spectra for silica-coated Nanofer 25 (SiO_2IO NPs) and STAR IO NPs
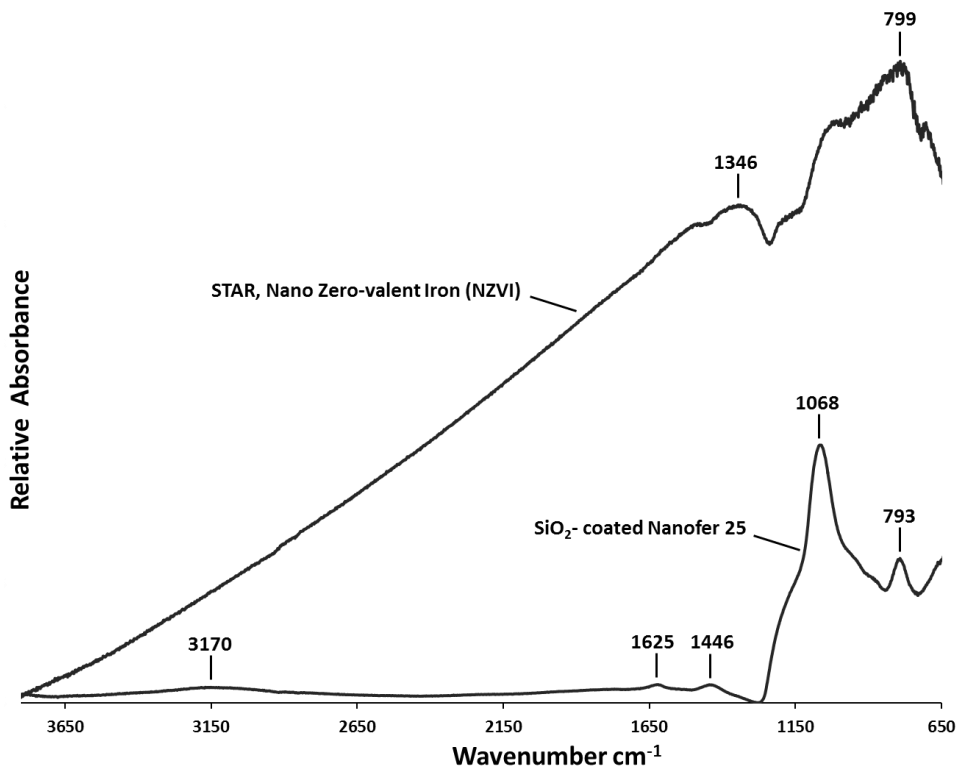
3.6.2 IR Frequency Region 3600-3200 cm^{-1}, 1640 cm^{-1}, and 700-300 cm^{-1}:

IR vibrational modes for hydrogen-bonded OH stretch (νOH) and water bend (δHOH)

The first high-frequency band in the infrared spectra of nearly all of the samples examined in this research is the very strong, very broad band occurring in the region 3342-3280 cm^{-1} which corresponds to the frequency region 3600-3200 cm^{-1} established for the stretching vibrations of hydrogen-bonded hydroxyl (OH) groups; thus, the band is known as the OH stretch (νOH) and is shown in Figure 3.22.[186,187] The νOH band can be assigned to the stretching modes of surface H$_2$O molecules or to an envelope of hydrogen-bonded surface OH groups.[188] OH groups form hydrogen bonds in condensed states (liquids or solids) of materials, resulting in broad peaks of the vibrational modes, or bands.[187]

Figure 3.22: IR spectra of the hydrogen-bonded OH stretching vibration
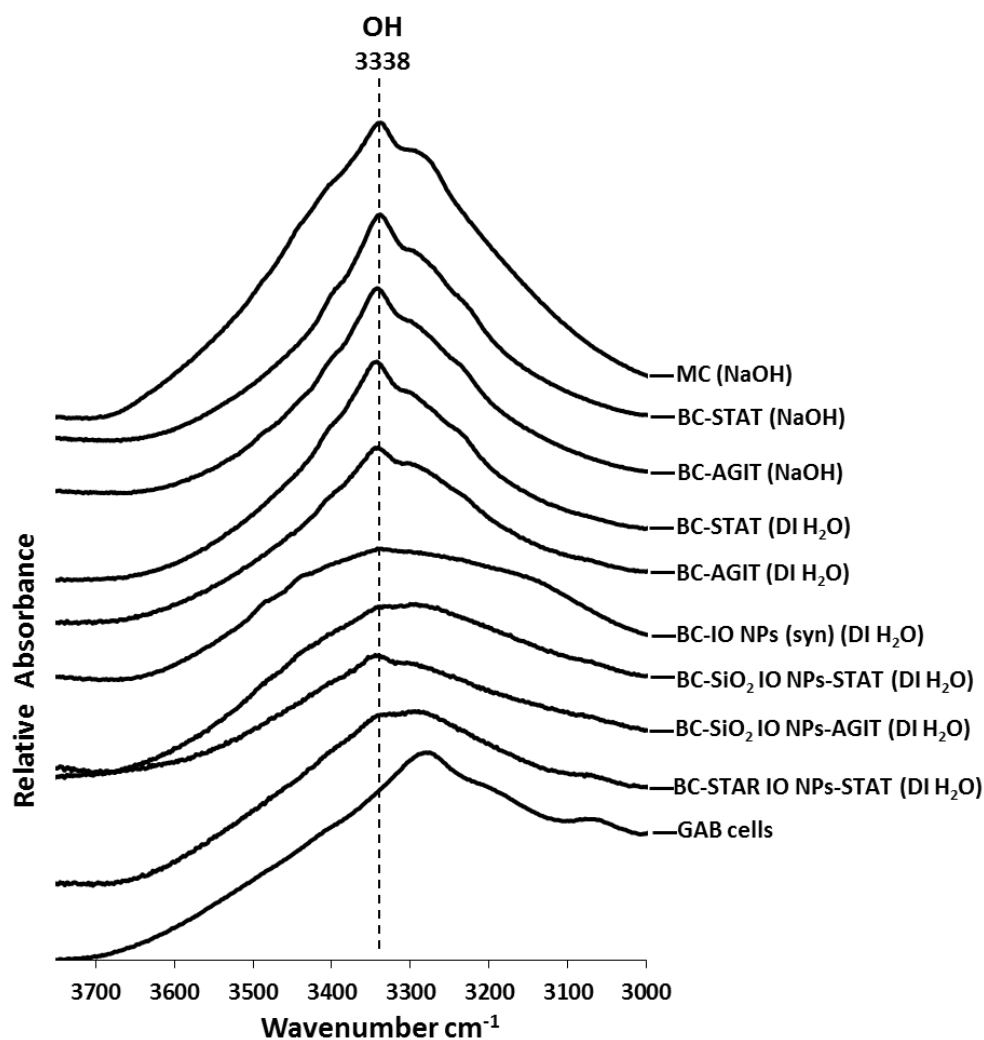
The presence of water and OH groups in the materials sampled in this study were revealed by the existence of two OH bands in the IR spectra, the OH stretching (vOH) and HOH bending (δ HOH) modes as depicted in Figure 3.20. The spectrum of water is actually characterized by three types of bands: a very strong and very broad band in the IR region 3600-3200 cm^{-1} due to the superposition of the two OH stretches, vOH (sym) and vOH (antisym), a medium-intensity broad band centered around 1640 cm^{-1} due to the HOH bending mode of adsorbed water, or the scissoring frequency, and a medium-intensity very broad band in the 700-300 cm^{-1} IR region due to the hindered rotation of water.[187] This latter band is very, very broad and appears in the lowest end of the fingerprint region as a broad swell; however, this band will not be discussed further as it occurs in the region in which distortion of the IR spectra occurs. Therefore, all spectra are examined in the 4000-650 cm^{-1} frequency range.

Several different sources contribute OH group vibrations which affect the shape of the vOH band, including the hydrogen-bonded OH groups of materials and water that incorporated into materials by being absorbed, adsorbed, or intercalated. Hydrogen bonding effects vibrational spectra significantly in several ways, and the stronger the hydrogen bond, the greater the effect. The hydrogen-bonded OH groups and water shape the vOH band, causing band broadening and curve changes depending on the modes present. Hydrogen-bonding both broadens and intensifies all OH bands—OH stretching vOH and OH bending δHOH bands.[187] An increase in the amount of water adsorbed, absorbed, or intercalated results in more interactions with the OH groups of a material; thereby increasing the height (absorbance) of the δHOH peak.

The OH stretch (vOH) is one of the characteristic bands of cellulose as the hydroxyl (OH) functional groups in cellulose macromolecules are involved in hydrogen bonding.[189,190] The cellulose molecule has OH functional groups at C2, C3, and C6 (Figures 3.23 and 3.24) which hydrogen-bond both intermolecularly and intramolecularly.[189,190] Hydrogen bonding occurs intermolecularly both at the O6H-O3 area of adjoining cellulose molecules,[191] and when OH groups of the cellulose molecule hydrogen-bond with other molecules, as in water intercalation.[192] Hydrogen bonding occurs intramolecularly at O3H-O5 and O2H-O6 and show modes in the vOH and δHOH frequency regions.[191]

Figure 3.23: The β-1,4-D-anhydroglucopyranose (cellobiose) repeating unit of cellulose schematically depicting the pyranose chair configuration and carbon atoms numbered 1-6
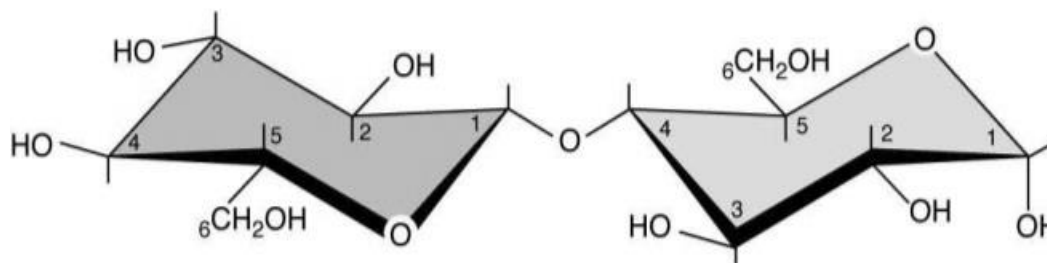
β-1,4-D-anhydroglucopyranose unit (AGU), or cellobiose

Figure 3.24: Molecular structure of cellulose showing the anhydroglucose unit (AGU) with n equaling the value of degree of polymerization (DP) and the end-groups, the non-reducing end-group to the left of the AGU and the reducing end-group to the right of the AGU
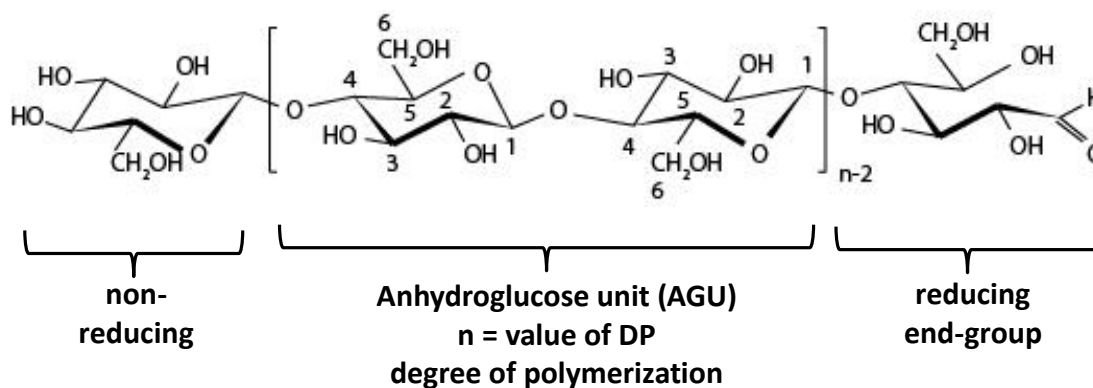
Materials contain multitudes of molecules, so the functional OH groups may each hydrogen-bond to a slightly different extent, resulting in IR absorptions at varying frequencies which causes peak broadening as the peak is the average of the various absorptions.[193] Some researchers state that the broad vOH band is due to the superposition of several types of OH stretches, both symmetric, vOH (sym), and antisymmetric, vOH (antisym).[187] The broad vOH band, or "peak," is indeed composed of several sub-peaks. Researchers mathematically analyzed IR spectral peaks of cellulose-containing materials using curve fitting software via deconvolutions or second derivations in order to identify various sub-peaks, and resolved the hydrogen-bonded vOH band, assuming the modes followed a Gaussian distribution, into three or four distinct sub-peaks or bands.[191,192,194] Even without software, multiple peaks can often be observed and assigned a peak frequency (wavenumber); for example, sub-peaks appeared either as peaks or as "shoulders" on the sides of

more distinct peaks. However, in the vOH band, only one or two sub-peaks could be visually discerned in the IR spectra of the materials in this research.

Some scientists assert that intermolecular and intramolecular hydrogen bonds cannot be distinguished by the position or the intensity of the OH stretch and others do not distinguish the OH stretch from hydrogen-bonded OH; conversely, some researchers claim that the OH stretch vibration is separate from that of the hydrogen-bonded OH.[187,194] For example, some researchers claim that in bacterial cellulose, the OH stretch occurs at 3500 cm^{-1} and hydrogen-bonded OH at 3246 cm^{-1}.[189] For cellulosic materials in general, some researchers claim that vOH occurs at 3175 cm^{-1}, at the intermolecular bond of O6H-O3 at 3230-3310 cm,[-1] and at the intramolecular bonds O3H-O5 and O2H-O6 OH at 3340-3375 cm^{-1} and 3405-3460 cm^{-1} respectively, and that the inter- and intramolecular hydrogen bonds occur separately around 3308-3486 cm^{-1}.[191] Other researchers assert that quantitative analysis of hydrogen-bonded spectra is unreliable and that qualitative analysis of the OH stretch is difficult to achieve.[187,195] In this study, it was impossible to distinguish the various modes coexisting in the vOH band, and therefore impossible to positively designate their peak frequencies.

Observable peak frequencies in the sample IR spectra were recorded in Table 1 located in the Appendix. In the vOH region, peak maxima ranged from 3342-3280 cm^{-1} for all materials sampled in this study. The vOH bands were particularly strong and sharp in the BC and MC samples; however, in the composite materials BC-IO NPs (syn), BC-SiO$_2$ IO NP-STAT, BC-SiO$_2$ IO NP-AGIT, and BC-STAR IO NPS-STAT, the bands were broader and at lower intensities. The vOH band of BC-IO NPs (syn) was the broadest of all the samples and appeared as a hump shape.

As more vibrational modes develop, the bands broaden. Broadening and multiple mode development is an indication of more disorder occurring in the vibrations of groups in the molecular structure of the materials. As a band broadened, the main peak intensity decreased, and several phenomena occurred: the underlying vibrational modes become visible in the IR spectra and appear as bumps along the sides of the dominant peak.

Only two peaks were recordable in the vOH bands of many of the samples: a dominant peak (the peak which shows the highest absorbance in the OH stretch region) occurring in the 3342-3332 cm^{-1} range, specifically around 3338 cm^{-1} in most samples, and a secondary peak on the right shoulder of the dominant peak occurring in the 3396-3388 cm^{-1} range. The dominant vOH peak and associated shoulder peak of the NaOH-purified bacterial cellulose samples BC-STAT and BC-AGIT and microcrystalline cellulose MC occur at 3338/3296 cm^{-1}, 3342/3295 cm^{-1}, and 3338/3298 cm,[-1]

respectively. The HOH bending mode occurs around 1640-1637 cm^{-1} in BC and 1640 cm^{-1} in MC. For samples containing *GAB* cells, the vOH peak location varies and the HOH bend is completely obscured by the presence of the Amide I band centered around 1642 cm.$^{-1}$ In the *GAB*-containing samples, the dominant and shoulder peaks are discernible: for BC-STAT-*GAB* (3332/3288 cm^{-1}) and BC-AGIT-*GAB* (3338/3290 cm^{-1}). However, for the sample composed entirely of *GAB*, only the dominant vOH peak appears, and at a lower frequency than all other samples—around 3280 cm.$^{-1}$ as the sample contains minimal BC residue and therefore fewer OH groups, although two bumps do appear on the right "shoulder" of this extremely broad main peak. The samples containing both *GAB* and cellulose show the secondary peak at higher wavelengths than *GAB* for they are dominated by the cellulose spectra. In BC-STAT-*GAB* and BC-AGIT-*GAB*, the dominant peak intensity decreased and the secondary peak became equal to or higher than the main peak respectively. This suggests that the group vibration causing the secondary peak became predominant.

For the iron oxide NP samples: Although we expect a very strong and broad band for adsorbed water in the wavenumber range 3450-3200 cm^{-1} on the surface of the silica-coated iron oxide nanoparticles; surprisingly, only a very weak broad band is seen around 3170 cm^{-1}, which is much lower than the cellulose vOH peak. For the SiO$_2$-coated iron oxide NPs (SiO$_2$ IO NPs), the vOH peak at 3170 cm^{-1} barely appears and is therefore insignificant. Other researchers assign bands in this range as characteristic of a Si-OH bond around 3400 cm^{-1} or as OH groups that are believed to exist on the silica surface.[97] While other researchers state that silica has a significant vibration at 3460 cm^{-1} for "water and silanol OH stretching" and that BC fibrils have free OH groups that react by hydrogen-bonding with the Si-OH groups of silica, this is not the case for the amorphous silica coating material in this research; the extremely low intensity vOH band does not provide evidence of the existence of OH groups or hydrogen-bonded water from silica, however some water was evidenced by the HOH bending peak.[189,196] The HOH bending band centered at 1625 cm^{-1} for SiO$_2$ IONPs, associated with the 1640 cm^{-1} vibration of water, is characterized by very low absorbance.

In the spectra of the nano-zero valent iron nanoparticles STAR IO NPs, neither the vOH nor the δHOH band appears. The unusual spectrum of STAR IO NP is characterized by an inclined slope of the spectrum from the lowest point at 4000 cm^{-1} and is described by researchers as resulting from reflection losses from the oxide surface of iron oxide NPs.[197]

For the synthesized iron oxide nanoparticles IO NP(syn), the OH stretch occurring in a very broad band that peaks around 3362 cm^{-1}, a little higher in frequency than in cellulose, and the HOH bending mode peaking around 1632 cm^{-1} show the presence of water molecules. [108,187] The spectrum

of the synthesized iron oxide nanoparticles reveals the strong bands characteristic of adsorbed water: the IR band centered at 3363 cm^{-1} can be assigned to the stretching modes of surface water molecules or to hydrogen-bonded surface OH groups on the IO NP. The intensity of the δHOH peak is greater in IO NPs (syn) than BC possibly because the IO NPs (syn) have more surface area than the BC nanofibers.

In the composite BC-iron oxide NP samples, the IR spectra indicate that cellulose dominates the IR spectra for the composites—the spectra exhibit few differences from BC spectrum; no peak shifting occurred and no new peaks were generated. This indicates that the interactions between BC and iron oxide NPs are mainly physical interactions and that no new chemical bonds were generated, with one exception, the BC-IO NPs (syn) composite.

For the BC-SiO$_2$ IO NP-STAT and BC-SiO$_2$ IO NPs-AGIT composite samples, the vOH band broadens and bulges around the sides of the dominant peak which remains distinct with little change around 3342 cm^{-1} which is also the peak frequency for the BC-AGIT sample.

The composite sample spectra for BC-SiO$_2$ IO NPs and BC-STAR IO NPs show little or no change in the vOH band compared to the BC spectrum; there is no evidence of OH group generation or interaction; this lack of OH change is evidence that the cellulose OH groups of the BC fibers are not hydrogen-bonding with the SiO$_2$ IO NPs. There appears to be very little or no increase in vOH group activity and the spectra are dominated by cellulose. The absence of chemical bonding is likely a result of the aggregation of the SiO$_2$ IONPs and STAR IONPs which affects any size-dependent NP properties; aggregation is known to decrease NP reactivity and result in surface passivation as well as altered surface tension; in addition, aggregation hampers oxides' ability to generate hydroxyl radicals and therefore reduces the number of OH groups.[198]

The composite made of iron oxide NPs synthesized in the purified BC matrix, BC-IO NPs (syn) STAT, exhibits a rounded, broadened vOH band that peaks around 3342-3338 cm^{-1}. Hydrogen-bonding causes broadening of OH bands; similarly, the broadened vOH band in the BC-IO NPs (syn) spectrum is evidence that the vibrations of the cellulose OH groups are affected by the presence of IONPs(syn) likely a result of hydrogen-bonding.[199] The vOH band was changed more greatly by the incorporation of IO NPs (syn) into the BC fibers for the BC-IO NPs (syn) sample than it was in all the other composite samples examined: the band was significantly broadened, and rounded, and the peak was decreased in absorption intensity, indicating disorder of the molecular structure and changes in the molecular group vibrations.

NaOH treatment, also called mercerization in industries that process cellulosic materials, is a common processing method for purifying cellulose. However, bacterial and plant cellulose are affected differently by mercerization. When the MC sample was treated with boiling 1 M (4 wt%) NaOH, the cellulose material turned a light tan color and the NaOH solution turned brown. Conversely, BC simply turned a white color of pure bacterial cellulose as all impurities such as *GAB* cells and media were removed. While researchers state that maximal cellulose dissolution occurs above 8 wt% NaOH they indicate that lower NaOH concentrations such as 4 wt% can cause plant-based cellulose fibers to swell, opening up the tightly-packed crystalline areas, which enables water to penetrate into the crystalline regions of the fiber and hydrogen-bond with the OH groups of cellulose.[200-202] Hydrogen-bond intensity is known to increase with NaOH treatment of plant cellulose.[192] In this case, mercerization intensified the hydrogen-bonded OH stretch and HOH bend peaks for MC, but had little or no effect on bacterial cellulose. The MC sample is characterized by a very strong, sharp νOH peak with an absorbance intensity higher than BC for both νOH and δHOH. BC is more resistant to NaOH at a 1 M (4 wt%) concentration than MC; therefore, higher concentrations are required to affect BC. Researchers indicate that the structure of BC is unaffected and unchanged by NaOH treatments in concentrations less than 6-9 wt% and that the fibrillar morphology and crystal structure is maintained.[203] One of the benefits of BC is that it can be cleaned with NaOH, resists alteration by NaOH treatment and maintains its crystal structure. Another benefit over plant cellulose is that BC is essentially pure cellulose and does not require the additional acid processing steps used to purify plant cellulose, so it is a more environmentally-friendly material.

3.6.3 IR Frequency Region 3000-2700 cm^{-1}: CH stretching (νCH) vibration bands (CH, CH$_2$ and CH$_3$ aliphatic groups)

Near the OH frequency band and moving to lower wavenumbers, the next absorption band, the CH stretching vibration (νCH), occurs in the frequency region 3000-2800 cm^{-1} and includes the vibrations of three aliphatic hydrocarbon (CH) groups: CH, CH$_2$, and CH$_3$. [184,187,189,192,194,204-208] The peak of the methine (CH) stretch occurs around 2885$\pm$10 cm^{-1} and four additional absorption peaks exist as two pairs of doublets in which one pair is attributed to methylene (CH$_2$)and the other pair to methyl (CH$_3$) group vibrations; specifically, the methylene symmetric and antisymmetric stretching modes: νCH$_2$ (sym) occurs near 2853$\pm$10 cm^{-1} and νCH$_2$ (antisym) occurs near 2926$\pm$10 cm^{-1}, and the methyl symmetric and antisymmetric stretching vibrations: νCH$_3$ (sym) occurs near 2872$\pm$10 cm^{-1} and νCH$_3$ (antisym) occurs near 2962$\pm$10 cm^{-1}.[184,187]

Of the samples investigated, those of pure cellulose have CH and CH_2 groups as expected for the cellulose molecule (shown in Figure 3.27), whereas those containing *GAB* have additional CH_3 groups since the major component of the *GAB* cell outer membrane is Lipopolysaccharide (LPS), which contains the functional groups CH_3, CH_2, OH, NH, and C=O, as shown in Figure 3.14.[55,183,209]

Figure 3.25: Schematic of the cellulose structure indicating the functional groups perceptible by IR spectroscopy
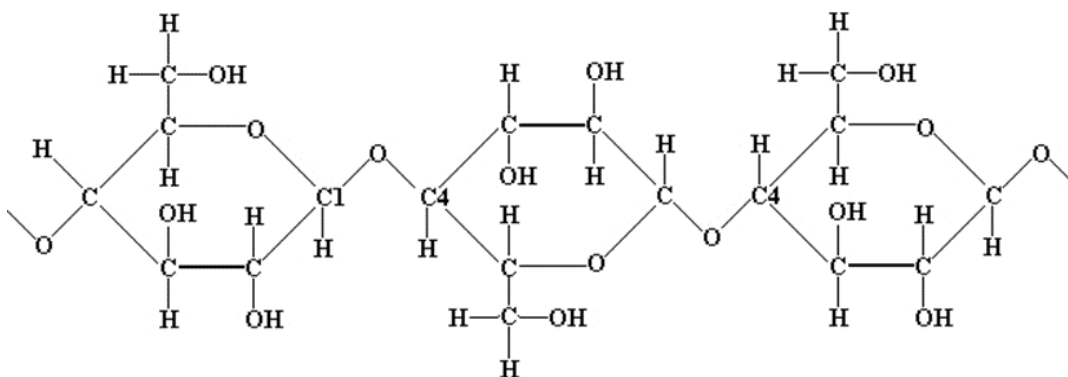
Figure 3.26: Lipopolysaccharide LPS, a major component of the outer membrane of *GAB* cells showing CH_3, CH_2, OH, NH, and C=O functional groups which appear as C-N stretching doublets which contribute to Amide I, II and III IR frequency bands. (Model adapted from an image on Todar's Online Textbook of Bacteriology: Complete structure of the Lipid A Moiety of LPS.
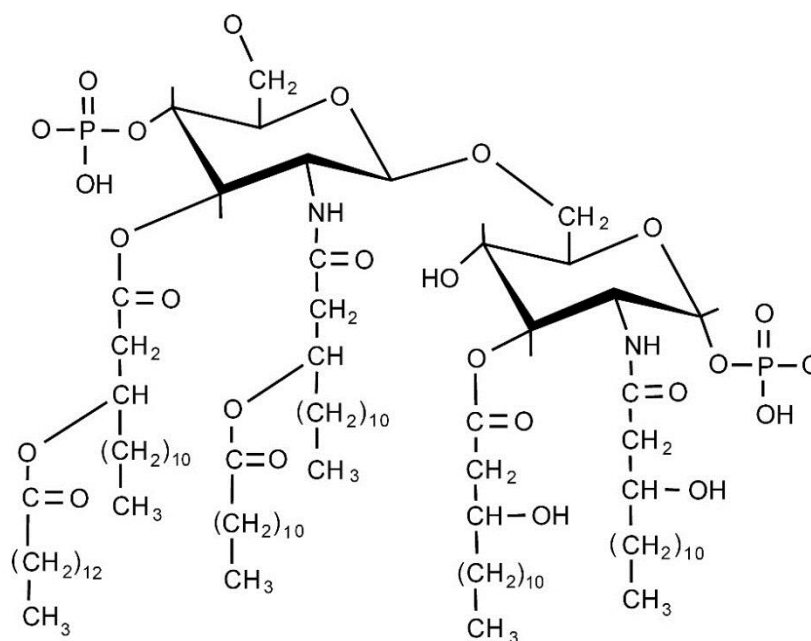
The *GAB* cell samples exhibited the most distinct vCH group vibrations of all. The *GAB* peak at 2959 cm^{-1} is attributed to vCH$_3$ (antisym), the peak at 2924-2923 cm^{-1} to vCH$_2$ (antisym), 2876-2873 cm^{-1} to vCH$_3$ (sym), and 2852 cm^{-1} to CH$_2$ (sym). The *GAB* sample vibrational modes fit into established interpretations for aliphatic hydrocarbons; thus the *GAB* IR spectrum acts as a good example of the CH$_2$ and CH$_3$ doublet pairs. The spectra of the composite sample BC-STAR-*GAB*-STAT aligns with the spectra for *GAB* cells, showing the peak around 2923 attributed to CH$_2$ (antisym).

In the BC samples of this research (and likewise in most PC cellulose samples reported in literature/MC cellulose samples), the CH stretching region is characterized by a dominant peak which has been assigned to the vCH groups; also, other vibrations occur within this region and appear as "shoulders" or bumps rounded peaks on the sides of the main peak or are indistinct, hidden under the curve of the main peak.[187] Figure 3.27 depicts the samples' IR spectra in the vCH region.

The optimal method of analysis would utilize curve fitting software after deconvolutions or conversions to the second derivative in order to resolve the various peaks for identification. For future work, this method should be employed.

Nevertheless, despite being indistinct, the peak heights of vibrational bands could be analyzed using both Omnic and Excel, and a considerable quantity of literature was reviewed to analyze and interpret the IR spectra and assign the vibrations to the materials' functional groups. In this research, the IR spectra of purified BC samples display the main vCH peak around 2896 cm^{-1} with shoulders which are actually several indistinct peaks. Two shoulders occur on the left side of the main peak and one on the right side. The main peak is assigned as CH[1] and occurs at 2897 cm^{-1} in BC-STAT, at 2895 cm^{-1} in both BC-AGIT and the composite sample BC-IO NPs (syn), and at 2901 cm^{-1} in MC. In addition, the CH vibration appears very faint in BC-SiO$_2$ IO NP-AGIT, BC-STAT-*GAB*, and BC-AGIT-*GAB* due to the dominance of the CH$_3$ vibrations associated with *GAB* cells; there is no vibration around 2897 cm^{-1} but rather at 2923 cm^{-1} for *GAB* cells. In the IR spectra of the BC samples containing *GAB* cells, the CH 2895 cm^{-1} peak occurs in addition to the two pairs of doublets attributed to CH$_2$ and CH$_3$. The BC-SiO$_2$ IO NP-AGIT composite is dominated by the BC spectra, not *GAB* or SiO$_2$ IO NPs, since the highest point of the spectra occurs at 2895 cm^{-1} due to the vCH vibration of cellulose.

The CH$_2$ (sym) vibration occurs at both 2872 cm^{-1} attributed to BC and at 2852 cm^{-1} due to *GAB* cells since this latter vibration only occurs in samples containing *GAB* cells. In the purified cellulose samples, the CH$_2$ (sym) mode does not appear as a distinct peak but rather as an indistinct bump along the shoulder of the main peak at 2872 cm^{-1} in BC-STAT and at 2873 cm^{-1} in BC-AGIT and

MC. All cellulose samples have two indistinct shoulder peaks, the one at 2942 cm^{-1} is assigned to CH_2 (antisym) and the peak at 2967 cm^{-1} is most likely assignable to vCH.

Figure 3.27: IR absorption bands in the frequency region 3000-2800 cm^{-1} attributed to the CH stretching vibration (vCH) which includes the vibrational bands of three aliphatic hydrocarbon (CH) groups CH, CH_2, and CH_3
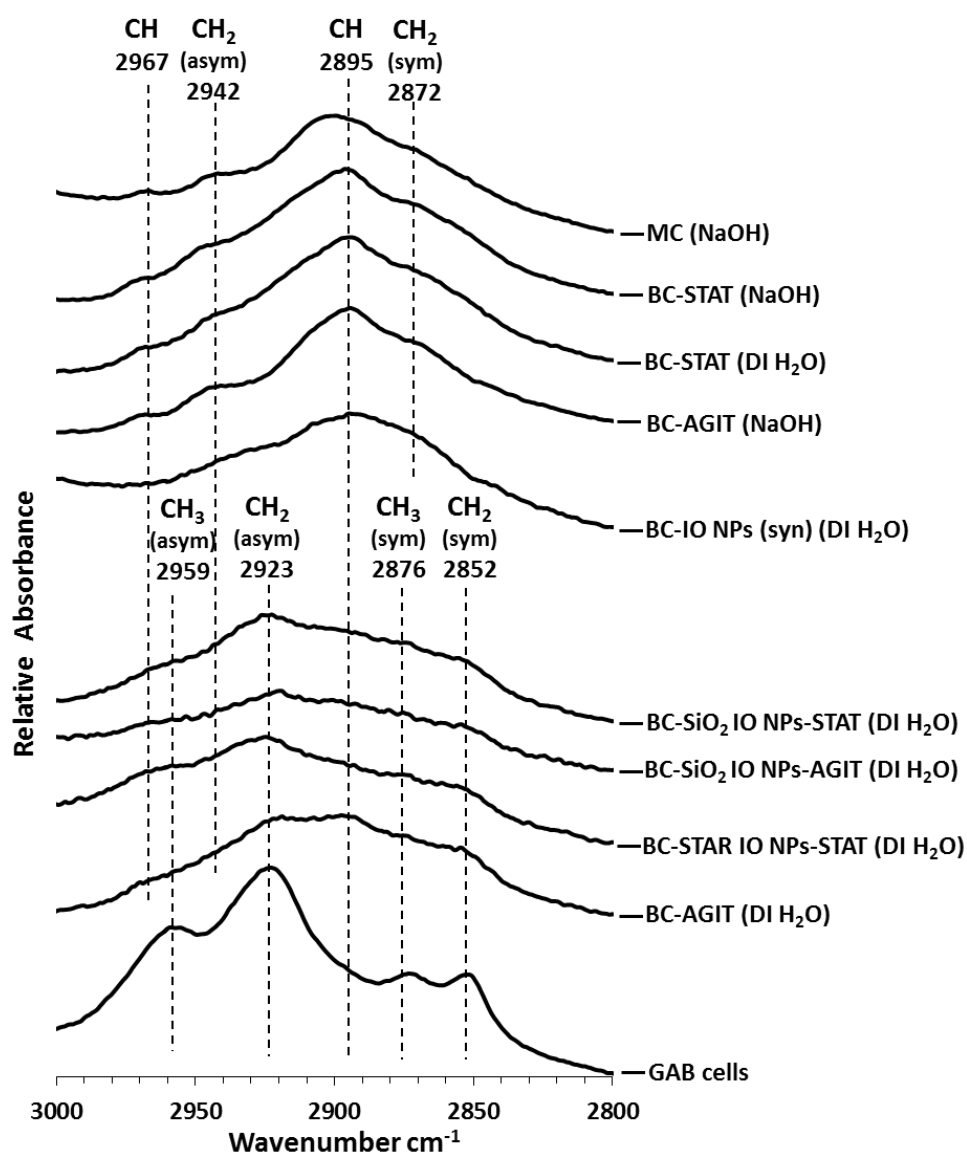
Interpretation of the shoulder peaks around the main peak at 2896 cm^{-1} is not as easy as in the case of *GAB* cell samples since there are no CH_3 groups present in samples either containing or dominated by cellulose. However, the doublet pair for vCH_2 did exist, so two of the three shoulder modes were assignable. The mode at 2941 cm^{-1} in BC-STAT and BC-AGIT and at 2942 cm^{-1} in MC

2942 cm^{-1} was assigned to vCH$_2$ (antisym), and the mode at 2872 cm^{-1} was assigned to vCH$_2$ (sym), both of which occurred at a slightly higher frequency than the standards reported at 2926±10 cm^{-1} for vCH$_2$ (antisym) and 2853±10 cm^{-1} for vCH$_2$ (sym).[184] This shift to higher frequencies from the standard ranges appears in all samples absent of *GAB*. The spectra for the composite BC- SiO$_2$ IO NPs-STAT sample closely resembles the purified BC and MC spectra. The composite BC- SiO$_2$ IO NPs-STAT peaks around 2895 cm^{-1}, any other modes do not appear and are indiscernible. The composite sample BC-SiO$_2$ NPs-AGIT is dominated by the cellulose spectra in addition to *GAB* as it displays the peak at 2852 cm^{-1} for CH$_2$ (sym); however, is difficult to clearly distinguish peaks.

There is an interesting hypothetical interpretation of this frequency shift. Recall that the standard vibration peak ranges are assigned to aliphatic hydrocarbons CH$_2$ and CH$_3$. Aliphatic compounds are joined together in straight chains, branched chains, or non-aromatic rings.[210] In *GAB* cells, the vibration peaks are indeed associated with the linear chained aliphatic groups of LPS as shown in Figure 3.26; whereas in cellulose the CH groups are located around the pyranose ring, where the carbon and hydrogen atoms occupy different positions and alignments along the undulating chair formation (as shown in Figure 3.28) which may cause the slight shift to higher frequencies in the samples containing cellulose. In addition, the indistinct shoulder mode centered around 2967 cm^{-1} and the distinct main peak which absorbs at 2897-2895 cm^{-1} are both attributed to vCH groups. The variations of the CH group placement along the pyranose ring may also cause the vCH groups to vibrate at different frequencies, such that vCH occurs at both 2967 cm^{-1} and 2895 cm.$^{-1}$

Figure 3.28: 3-D models of the structure of cellulose, (a) the anhydroglucose (cellobiose) repeating unit of cellulose with its 3-D undulating chair configuration as appears in the molecule, and (b) a simplified schematic of a single cellulose chain of two cellobiose units joined, showing the carbon (black), oxygen (dark gray) and hydrogen (white) atoms.
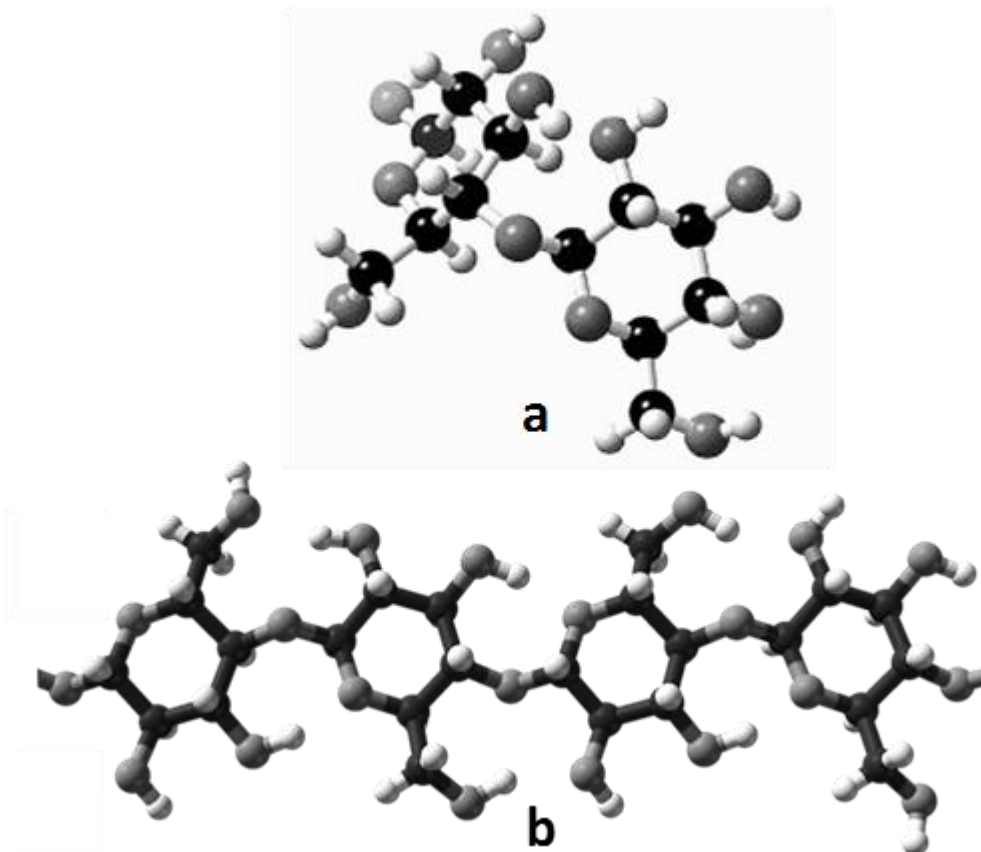
3.6.4 IR Frequency Region 1700-1200 cm^{-1}: Amide I (vC=O), II (δNH), & III (vC-N) bands

One of the most notable aspects of the sample IR spectra in the 1750-1200 cm^{-1} frequency region (Figure 3.29) is the difference between samples that contain *GAB* cells (which exhibit very strong prominent bands attributed to vC=O, δNH, and vCN of the Amide I, II, and III bands respectively) and all others which do not, and instead show a weak peak of the bending mode of absorbed water, δHOH. Samples cleaned of *GAB* cellular debris and other impurities using NaOH exhibit only δHOH and cellulose characteristic bands. As a result, ATR-FTIR can be employed to determine whether BC samples have been cleaned of *GAB* cells or not based on the absence or presence, respectively, of the secondary amide peaks, especially the very large peaks at 1636 cm^{-1} (Amide I, vC=O) and 1528 cm^{-1} (Amide II, δNH). In this region, the IR spectra of samples containing *GAB* cells and bacterial cellulose (BC-*GAB*) are characterized by group frequencies for both amides

and cellulose. This verifies that the composite materials made by growing cellulose in nanoparticle-modified media contain *GAB* cells. The samples containing cellulose do display characteristic peaks attributed to the various CH bending modes (δCH) which will be discussed in more detail in the next section.

The most distinctive bands for all samples containing *GAB* cells are those of the amides; in particular, the very strong double bands of the secondary amides (2nd) which appear in the 1650-1525 cm^{-1} frequency region. In purified *GAB* cell samples, these secondary amide bands occur at 1636 cm^{-1} and 1528 cm^{-1} whereas a shift to higher frequency occurs in bacterial cellulose (BC) samples containing *GAB* cells as the modes appear in the range of 1649-1640 cm^{-1} and 1544-1534 cm^{-1}. The very strong mode occurring at about 1636 cm^{-1} for *GAB* cells and ranging from 1649 cm^{-1} to 1640 cm^{-1} for samples containing both BC and *GAB* cells is assigned as the carbonyl bending (v C=O) vibration of the Amide I band of secondary amides reported by various sources to occur in the regions 1680-1630 cm^{-1}, [186] 1652-1637 cm^{-1}, [211-213] or 1650-1640 cm^{-1}.[187] The HOH bending vibration δ HOH was obscured by Amide I of the secondary amide.

The second very strong mode occurring at 1544 cm^{-1} for agitated samples containing BC plus *GAB* cells and at 1528 cm^{-1} for *GAB* cells is attributed to the NH deformation of the Amide II band of secondary amides reported in the frequency regions 1565-1475 cm^{-1},[186,214] and 1550-1540. [211,213,215]

Secondary amides (such as the peptide link which occurs in proteins and polypeptides) are ubiquitous and thus important in spectroscopy.[187] The Amide II band of secondary amides has also been reported differently as a mixture of C-N stretching (vC-N) and NH in-plane bending (δNH) which interact to produce two bands, the distinct Amide II δNH band at approximately 1550 cm^{-1} and the medium-intensity vC-N Amide III band of primary amides in the region 1300-1220 cm^{-1}, where the latter is further described as the low-frequency component of Amide II occurring near 1300 cm^{-1} but deemed of little use as a group frequency.[187] Although the *GAB* cell samples exhibit a δNH vibration at 1528 cm^{-1} , not 1550 cm^{-1} (this may be close enough), the "mode-mixing" interpretation might be applicable to the samples containing *GAB* cells because they exhibit a medium intensity mode occurring at 1229 cm^{-1} which most certainly cannot be attributed to the strong intensity modes of the amines reported at 1280-1180 cm^{-1} and 1230-1100 cm^{-1} as the majority of bands in the 1200-1300 region exhibit strong, not medium, intensities.[186,214] This mode at 1229 cm^{-1} could be the shifted vC-N Amide III band as reported; for while the C-N stretch normally occurs at 1420-1400 cm^{-1}, in samples with *GAB* cells, no mode appears in that frequency range.[186,187,214]

All samples containing *GAB* cells show the Amide I and II peaks as two separate peaks including *GAB*, BC-STAT-*GAB*, BC-AGIT-*GAB*, and BC-SiO$_2$ IO NPs-STAT, BC-SiO$_2$ IO NPs-AGIT, and BC-STAR IO NPs (STAT); whereas only some show the Amide III peak which seems to validate the claim that Amide III is not a useful group frequency for it is usually indistinct or indiscernible.[187]

The next mode at 1389 cm^{-1} is also medium-intensity and most likely is the medium-intensity C-N stretch (vC-N) of the Amide III band reported in the 1400-1420 cm^{-1} region that has shifted to a lower frequency. If this is the case, the "mode-mixing" interpretation of the medium-intensity peaks at 1528 and 1229 cm^{-1} is appropriate, and vC-N vibrates at both peak regions. The 1389 cm^{-1} mode in *GAB* cell samples is nearly imperceptible in BC-STAT-*GAB* where it seems to be shifted and merged with the cellulose doublet bands located around 1371-1361 cm^{-1} discussed in Part 2. BC-STAR IO NPs contains *GAB* cells and the very broad indistinct band peaking around 1390-1384 cm^{-1} is associated with the vC-N Amide III band of *GAB* cells.

The next band associated with *GAB* cells is a very broad medium-intensity mode occurring at 1229 cm^{-1} attributed to the vC-N Amide III band as mentioned previously as it is not possible that this medium intensity band could be the strong C-O stretch (v C-O) of alcohols reported in the 1065-1015 cm^{-1} region.[187]

All bands in the *GAB* spectrum are broad, for although the sample was washed three times with centrifugation, impurities persisted such as HS media and cellulose residue. Impurities and the *GAB* cells themselves made the material was more amorphous and interfered with IR absorption; therefore, the structure more disordered, the effect of which is band broadening.[216]

Figure 3.29: 1700-1200 cm^{-1} IR Frequency Region showing Amide I (γC=O), II (δNH), and III (γC-N) bands and C-H bending (δCH) modes δCH$_2$ (sym) and δCH$_3$ (sym).
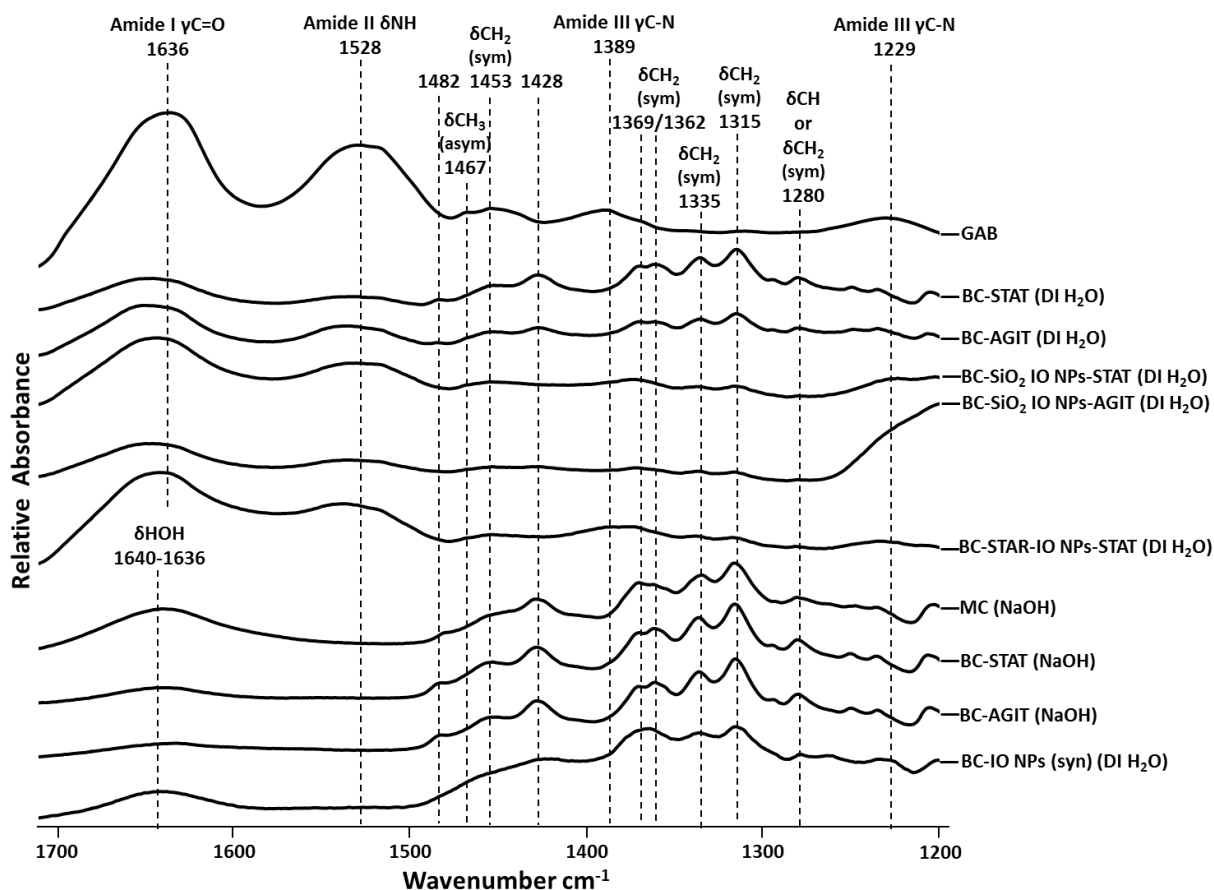
3.6.5 IR Frequency Region 1500-1250 cm^{-1}: CH bending δCH$_2$ (sym) & δCH$_3$ (sym)

In this region, for the composite samples produced in NP-modified growth media BC- SiO$_2$ IO NPs-STAT, BC- SiO$_2$ IO NPs-AGIT, and BC-STAR IO NPs-STAT, all of the peaks were broadened and diminished in absorption intensity with respect to the cellulose samples MC, BC-STAT, BC-AGIT, BC-STAT-*GAB*, and BC-AGIT-*GAB*. This may be due to the IO NPs or the *GAB* in these samples which could be interfering with the IR vibrations of cellulose.

The first group of cellulose IR modes in the 1500-1250 cm^{-1} frequency region (Figure 3.29) appears in the 1500-1400 cm^{-1} range and is characterized by three peaks which are visible in purified BC samples from both static and agitated cultures, but which are less distinct in MC. Two modes, at 1482 cm^{-1} and 1453 cm^{-1} in BC, and at 1479 cm^{-1} and 1453 cm^{-1} in MC, appear on the shoulder of the mode at 1428 cm^{-1} for pure BC and MC samples and at 1426 cm^{-1} for BC-AGIT-*GAB*. The 1428 cm^{-1} mode is attributed to symmetric bending of the CH$_2$ group at C6, or δCH$_2$ (sym) at C6 adjacent to C=O

on the β-(1,4)-D-glucopyranose unit of the cellulose molecule.[192] Other researchers reported δCH$_2$ (sym) at C6 in the 1470-1440 cm^{-1} range and at 1460 cm^{-1}.[186,189]

GAB samples exhibit two vibrational modes in a slightly different location than those of BC, and the BC-*GAB* samples exhibit a combination of the modes of *GAB* and BC. *GAB* and BC -STAT-*GAB* do not have modes at 1485 cm^{-1} and 1428 cm^{-1} whereas BC-AGIT-*GAB* does. The *GAB* cell, BC-AGIT-*GAB*, and BC-STAT-*GAB* samples show a band at 1467 cm^{-1} (barely visible in the latter two) which appears on the shoulder of a larger band at 1455, 1453, and 1449 cm^{-1}, respectively. Since the mode at 1467 cm^{-1} is not found in purified BC and MC, this vibrational band is assigned to the antisymmetric CH$_3$ deformation, δCH$_3$ (antisym), associated with samples containing *GAB* cells which have CH$_3$ groups and reported to occur around 1470-1440 cm^{-1} or 1460 cm^{-1}.[186,187] Even though the larger band occurs around the same frequency associated with the middle of the cellulose "triplet" peaks at 1453 cm^{-1}, this band around 1455-1449 cm^{-1} is unique to the *GAB*-containing samples for it is stronger than the 1453 cm^{-1} mode which is considerably and consistently less intense in the cellulose-containing samples. Furthermore, it appears "peak to peak" alongside the cellulose 1428 cm^{-1} mode, or at just a little higher intensity, as seen in the BC-AGIT-*GAB* spectra. The medium-intensity mode around 1454 cm^{-1} exhibited by samples with *GAB* cells is assigned as the symmetric CH$_2$ bending vibration, δCH$_2$ (sym) of the vibrations of the CH$_2$ groups in *GAB* samples around 1455-1459 cm^{-1} since BC also vibrates at 1453 cm^{-1} indicates that the peak region can be assigned as δCH$_2$ (sym).

The peak at 1428 cm^{-1} assigned to δCH$_2$ (sym) at C6 of the cellulose molecule is found in the samples BC-STAT, BC-AGIT, and MC.[192] This peak occurs at 1426 cm^{-1} for BC-AGIT-*GAB*. BC- SiO$_2$ IO NPs-STAT, BC- SiO$_2$ IO NPs-AGIT, and BC-STAR IO NPs-STAT; the composites' peaks are lower and less pronounced. The 1428 cm^{-1} peak occurs at a lower frequency than reported for δCH$_2$ (sym), 1480-1440 cm^{-1}.[186 1450,187] However, other researchers have reported the 1428 cm^{-1} peak in BC or other cellulosic materials at 1430-1420 cm^{-1},[186] 1431-1419 cm^{-1},[194,217-220] 1426 cm^{-1},[221,222] and 1425 cm^{-1}.[223] In the BC-STAT-*GAB* sample, the 1429 cm^{-1} peak is nearly completely obscured by the broadened 1453 cm^{-1} peak, but barely perceptible at 1429 cm^{-1}; it is likely that this also occurs in the *GAB* sample as well since the low point between the peaks of δCH$_2$ (sym) at 1453 cm^{-1} and Amide III vC-N at 1389 cm^{-1} is likely high enough to obscure the 1429 cm^{-1} peak. In purified *GAB* cell samples, the 1454 cm^{-1} mode appears solely as its own peak as the 1427 cm^{-1} mode is obscured.

The cellulose doublet around 1371-1361 cm^{-1} is assigned to C-H bending (δ CH) [208,219] or δCH$_2$.[189] In all cellulose-containing samples, modes attributed to δCH$_2$ (sym) occur as a doublet at

1369/1361 cm^{-1} for BC-STAT and BC-AGIT, at 1369/1362 cm^{-1} for MC and BC-AGIT-*GAB*, and at 1370/1362 cm^{-1} for BC- SiO$_2$ IONPs-AGIT. The first peak of BC-STAT-*GAB* appears at 1370 cm^{-1} but the second disappeared, perhaps due to *GAB* cells dominating the spectra, and in the composite BC-IO NPs (syn) the doublets merge into one curve with a peak at 1363 cm^{-1} and broaden.

The last three δCH$_2$ (sym) vibrations appear in all cellulosic samples as they are modes characteristic of cellulose. The first occurs at 1336 cm^{-1} for BC-STAT-*GAB*, at 1335 cm^{-1} for BC-STAT, BC-AGIT, MC, BC-STAT-*GAB* and the composites BC- SiO$_2$ IO NPs-AGIT, BC- SiO$_2$ IO NPs-STAT, and BC-IO NPs (syn), and at 1336 cm^{-1} for BC-AGIT-*GAB* . The next vibration is at 1315 cm^{-1} for BC-STAT, BC-AGIT, MC, BC-AGIT-*GAB*, and the composites BC- SiO$_2$ IO NPs-AGIT and BC-IO NPs (syn), and at 1314 cm^{-1} for BC-STAT-*GAB*. The last δCH$_2$ (sym) mode occurs at 1281 cm^{-1} in BC-STAT and the composite BC- SiO$_2$ IONPs-AGIT, at 1280 cm^{-1} in BC-AGIT and MC, at 1279 cm^{-1} in the composite BC-IO NPs (syn), and at 1278 cm^{-1} in BC-STAT-*GAB*. The δCH$_2$ (sym) modes appear almost imperceptibly in the *GAB* sample at 1343 and 1309 cm^{-1} and this indicates that the *GAB* sample contains traces of cellulose that remained with the *GAB* cells when they were collected from the blended BC pellicle via filtration because these modes are associated with cellulose.

For the composite sample BC-IO NPs (syn) in this region, the most noticeable changes occurred in the three peaks in the range 1490-1410 cm^{-1} as well as the doublet in the range 1350-1390 cm^{-1} which were merged and broadened such that only one peak was recordable at 1423 cm^{-1} and 1363 cm^{-1}, respectively.

Figure 3.30: IR frequency region 1250-650 cm^{-1} with COH bending (δCOH), COC stretching (γCOC), C-O stretching (γC-O), δ Fe-OH (bending) , and Si-O stretching modes.
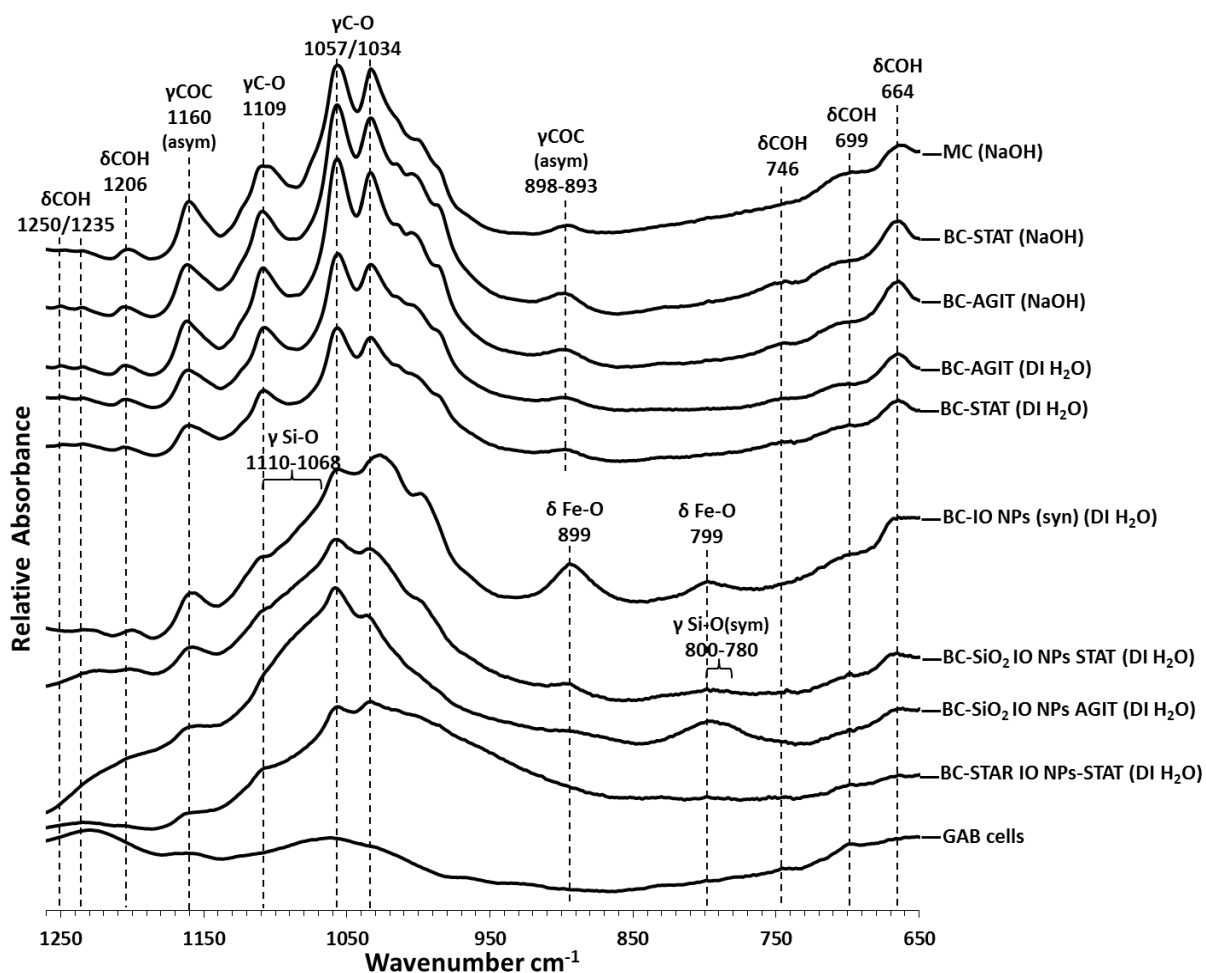
3.6.6 IR Frequency Region 1255-650 cm^{-1}: COH bending (δCOH), COC stretching (vCOC) CO stretching (vCO), and Si-OH, Si-O, Fe-O, and Fe-O-Fe

All the cellulosic samples, including the various BC samples, MC, and BC composites (BC-SiO$_2$ IO NPs, BC-IO NPs (syn), and BC-STAR IO NPs) exhibit the same characteristic cellulose IR spectra in the 1255-650 cm^{-1} region presented in Figure 3.30. All of the frequencies in the cellulose spectra in this region are associated with carbohydrates.

One of the vibrations of the cellulosic samples in this region is the C-OH bending mode (δCOH) associated with in-plane bending at C6[219,220] of the cellulose molecule which first occurs as two weak modes side-by-side, one mode in the range 1250-1247 cm^{-1} with the exception of BC-IO NPs (syn) composite where it vibrates at a slightly higher frequency of 1263 cm^{-1}, and another mode

in the range 1235-1232 cm^{-1}. The peak at 1263 cm^{-1} is more pronounced in BC-IO NPs (syn) compared to the cellulose samples where it is imperceptible in BC and only very faintly perceptible in MC and BC-AGIT-*GAB* at 1264 cm^{-1}. The peak at 1263 cm^{-1} is likely associated with the δCOH vibration occurring at the lower wavelength of 1250 cm^{-1} for researchers state that treating celluloses with NaOH causes the band at 1263 cm^{-1} to be decreased in frequency[192]. The next instance of the δCOH in-plane mode is a little stronger, in the range 1206-1200 cm^{-1} for the samples examined. The final three δCOH bands occur in the range 750-650 cm^{-1}; specifically, with weak peaks ranging from 746-663 cm.[-1]

The cellulose IR spectrum is characterized by a group of very strong to medium intensity bands in the 1130-850 cm^{-1} region caused by the antisymmetric COC stretching (νCOC (antisym) and C-O stretching (νC-O) vibrations. The C-O stretching vibration features three prominent peaks—a doublet and a single peak at the side with additional indistinct modes along the shoulders. The distinct νC-O peak at 1109 cm^{-1} is assigned to the C2O2 group[199,221]. The first peak of the doublet occurs around 1057 cm^{-1}, the second around 1034 cm^{-1}; the vibrations are attributed to the C-O stretch at C3O3H and C6H$_2$O6, respectively.

The strong and sharp peak in the 1162-1159 cm^{-1} region is attributed to the antisymmetric stretch vibration of the C1OC4 groups at the β-1,4 glycosidic linkages in the cellulose molecule which join two glucose molecules of cellulose to form the anhydroglucose unit (AGU), or cellobiose unit, which in turn forms the extended ribbon conformation of the cellulose polysaccharide. The COC stretch of the glycosidic link also occurs as a medium intensity peak around 898-893 cm^{-1}

Note the two most insignificant spectra belong to two samples, BC-STAR IO NPs and *GAB*. In the BC-STAR IO NPs composite sample, all peaks normally occurring in the region 1170-850 cm^{-1} are merged into one broad peak, and the only other mode weakly appears at 790 cm^{-1} which is likely associated with the δFe-O mode normally found at 799 cm^{-1}.[188] The *GAB* sample displays weak broad modes around 1163 cm^{-1}, 1150 cm^{-1}, 1061 cm^{-1}, and 891 cm^{-1} which are due to cellulose impurities remaining in the sample as these bands are characteristic of the spectra of the cellulose molecule.

The IR spectrum for the silica-coated iron oxide nanoparticle aggregates, SiO$_2$ IO NPs, displays vibrations characteristic of silica (SiO$_2$) for there exists a very strong yet very broad band centered around 1067 cm^{-1} which aligns with the IR vibrations reported for SiO$_2$ in the 1100-1000 cm^{-1} wavenumber range[224] and is attributed to either the Si-O stretch[187] or the Si-O-Si antisymmetric stretch.[186]

The 1067 cm^{-1} vibration has been attributed to the Si-O-Si vibration of the three-dimensional siloxane bond formation following the Fe-O-Si linkage in the process of silica-coating maghemite (γ-Fe$_2$O$_3$). Liu, 1998 #82} On the higher wavenumber side of this broad 1067 cm^{-1} peak there is a shoulder around 1250-1125 cm^{-1}. On the lower wavenumber side of this broad peak that spans from approximately 1257-910 cm^{-1}, there exist several shoulders which are due to unresolved underlying vibrational bands, one of which occurs around 950 cm^{-1} which was reported as the Si-OH stretching band designated at 949 cm^{-1}[189], another occurs around 881 cm^{-1}. Around 843 cm^{-1}, the broad 1068 cm^{-1} peak appears to merge with the base of another fairly high-intensity peak that centers at 795 cm^{-1}; this second largest peak can be attributed to the Si-O-Si symmetric stretching found at 804 cm^{-1}.[189] The band centered around 795 cm^{-1} has also been attributed to the Si-O stretch which occurs around 800 cm^{-1}.[187,224] The peaks at 557 cm^{-1} and 414 cm^{-1} correspond to the two vibrations characteristic of SiO$_2$ occurring in the fingerprint region in the 500-350 cm^{-1} range; in fact, SiO$_2$ is known for a very strong peak, greater in intensity than the one around 1100-1000 cm^{-1}, centered around 470 cm^{-1}.[187,224]

The strong bands at 1067 cm^{-1} and 793 cm^{-1} which are characteristic of the SiO$_2$ IO NPs can be observed in the spectrum of the BC-SiO$_2$ IO NPs composites. However, the composite spectra are dominated by the cellulose spectra. Unfortunately, both silica and iron oxide vibrational frequencies overlap with many of the cellulose peaks making it impossible to determine the interactions and effects between the materials. In BC-SiO$_2$ IO NPs composites, the silica peak at 1067 cm^{-1} overlaps with the most prominent band in cellulose, νC-O around 1080-970 cm^{-1} which broadens the band and in some instances shows the shoulder bumps associated with SiO$_2$ IO NPs shown in Figure 3.21.

The BC-IO NPs (syn) composites prepared by synthesizing iron oxide NPs into the cellulose fiber matrix show a distinct band at 899 cm^{-1} corresponding the bending mode of Fe-O-H (δFe-O-H) which is associated with iron oxides, magnetite in particular. The characteristic iron oxide fingerprint modes in the region 600-400 cm^{-1} are observed in the BC-IO nanocomposites as the absorbance intensity greatly increases in the region 500-400 cm^{-1} when compared to the pure bacterial cellulose spectrum.

The BC-IO NPs (syn) IR spectrum shows hints of the modes centered at 899 cm^{-1} and 799 cm^{-1} which are due to Fe-O bending vibrations.[188] The barely perceptible band centered at 799 cm^{-1} is most likely the same one that occurs around 700-750 cm^{-1} in magnetite.[224] This same vibration is also observable in the BC-IO NP (syn) nanocomposite. A strong band centered at 547 cm^{-1} on iron oxide nanoparticle spectrum corresponds to the Fe-O or Fe-O-Fe stretching vibration reported in the

wavelength range around 600-500 cm^{-1} for magnetite and maghemites[187,197,224] and for magnetite nanoparticles in particular.[225-227] Another fingerprint mode occurs around 407 cm^{-1} and is assigned as the Fe-O stretch v(Fe-O) reported around 400 cm^{-1} as corresponding to the tetrahedral iron atoms.[108,224]

3.6.7 Spectral Subtraction Strategy to Study NPs -BC Interactions in Composites

One strategy for examining the possible types of chemical bonding that might exist between the iron oxide nanoparticles and cellulose is to use the region of the composite materials between 1500-1110 cm^{-1}, a region where the Si-O and Fe-O bands are absent and where water, SiO_2, Fe_3O_4 , and Fe_2O_3 do not absorb, and perform spectral subtraction in OMNIC, and then examine the group frequency region above 1500 cm^{-1} for any possible evidence of chemical bonding. When subtracting the spectrum of the reference material of purified bacterial cellulose from that of the BC-IO NP (syn) and BC-SiO$_2$ IONP composites, this might reveal changes that may occur due to molecular interactions of the components in the composite or differences in relative concentrations of components.

This strategy of spectral subtraction showed evidence of chemical bonding in the OH frequency region of the spectrum for the BC-IO NP (syn) composite. The spectral subtraction result in Figure3.31 demonstrated increased IR absorbance in the region related to hydrogen bonding of cellulose OH functional groups, at 3486 cm^{-1} and 3137 cm.$^{-1}$This result supports the hypothesis that Fe^{2+} and Fe^{3+} ions in the aqueous iron salt solution are carried by water into the interchain and intersheet zones of the cellulose structure prior to being chemically reacted into Fe_3O_4 or Fe_2O_3. A wide band with two main peaks attributed to the Fe-OH bending mode (δFe-OH) occurs in the IR range 980-650 cm^{-1}.

On the other hand, the spectral subtraction result for the BC-SiO$_2$ IO NP composite did not show any evidence of chemical bonding over the entire spectrum; in fact, the resulting subtraction spectrum in Figure 3.32 displayed negative peaks below zero on the absorbance scale. Therefore, no hydrogen bonding resulted from spectral subtraction of the composite material made by producing cellulose from the bacteria in the presence of silica-coated iron oxide nanoparticles. This result lends credence to the idea that the silica-coated nanoparticles were physically trapped, or embedded, in the cellulose matrix as the bacteria exuded cellulose.
A band of various peaks attributed to the δFe-OH, vSi-O, and/or δSi-O-Si modes occurs in the IR range 950-650 cm^{-1}.

Figure 3.31: Results of spectral subtraction of the purified bacterial cellulose reference material spectrum from that of the BC-IO NP (syn) composite spectrum.
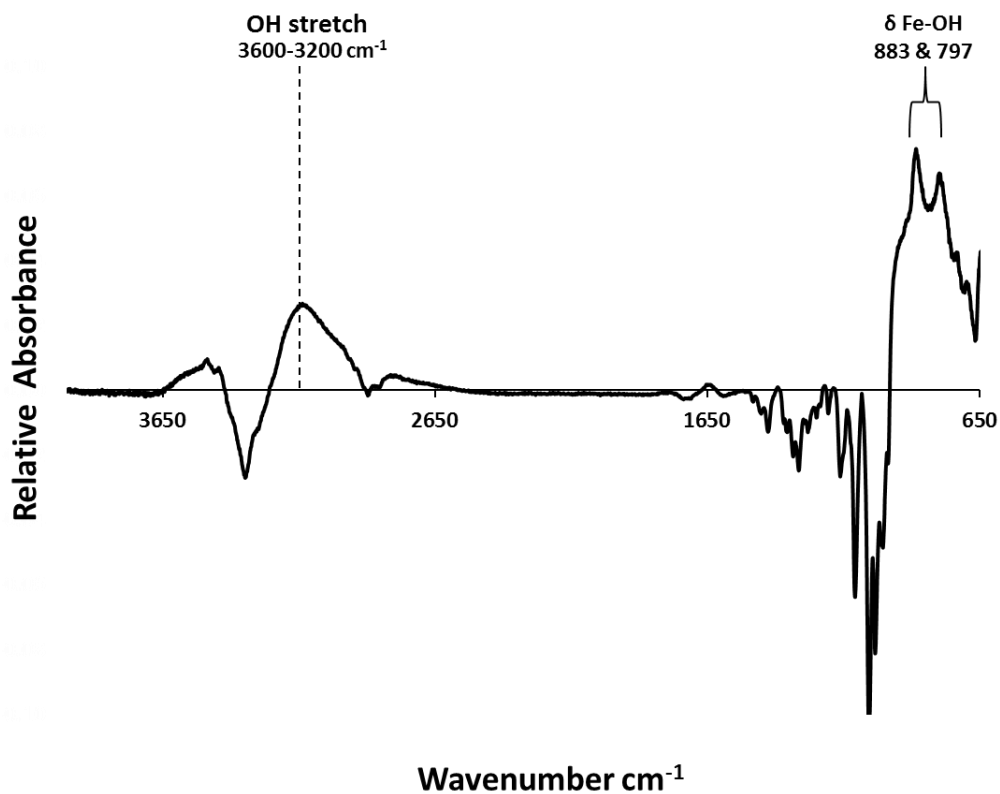
Figure 3.32: Results of spectral subtraction of the purified bacterial cellulose reference material spectrum from that of the BC-SiO$_2$ IO NPs composite spectrum.
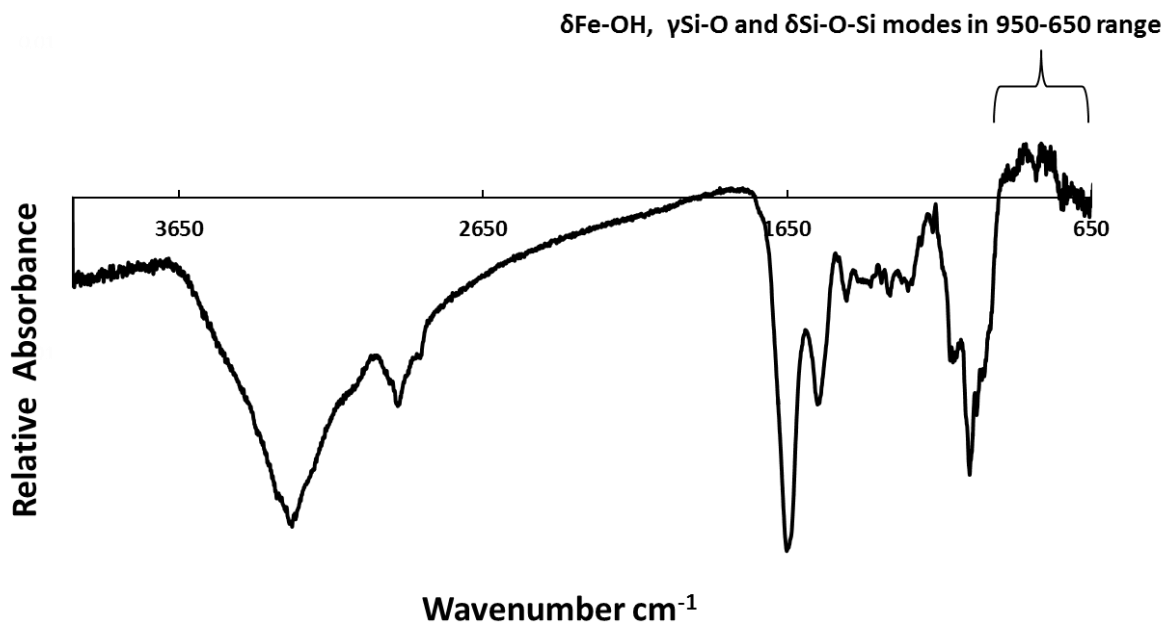
3.6.8 Challenges to ATR-FTIR Analysis and Interpretation of BC-NP Interactions in Composites: Problem of IR Vibrations Co-occurring in the Same IR Spectral Region

Analysis and interpretation of the IR spectra of the materials investigated in this research is complicated by fact that the spectral vibrations overlap, occurring at similar frequencies, or IR spectral regions. The co-occurrence or overlapping of bands makes investigating the interactions between the bacterial cellulose nanostructure and the iron oxide nanomaterials difficult. Nevertheless, the main band of interest for determining interaction between iron oxide and cellulose is the OH group vibration in the cellulose molecule which does not have overlapping.

Functional groups of the materials examined in this research, for example, cellulose, iron oxides, silica, and *Gluconacetobacter*, vibrate around the same frequency ranges of which complicates the reading of the IR spectra shown in Figures 3.20, 3.21, and 3.30. The largest peak for silica, the Si-O stretch (νSi-O), occurs around 1075-1068 cm^{-1} in the samples-reported to occur around 1110-1068 cm^{-1} [189,228] and is obscured beneath the C-O stretch around 1027-1061 cm^{-1}. The Fe-OH bending mode (δ Fe-O-H) at 899 cm^{-1} coincides with the νCOC (antisym) stretching vibration of cellulose which occurred at 898-893 cm^{-1} in the samples. The next Si-O symmetric stretch around 796-793 cm^{-1} in the samples (reported around 800-780 cm^{-1} [228]) or Si-O-Si stretch reported at around 804 cm^{-1} [228] coincide with the bending mode of Fe-O-H at 799 cm^{-1}.[188]

4. CONCLUSIONS AND FUTURE WORK

Composites of BC nanofibers and iron oxide NPs were produced and analyzed to determine the interactions of the materials. The composition, structure, and morphology of the composites was engineered by combining BC with iron oxide NPs of various types and concentrations using two methods: in the first, the culture medium of *Gluconacetobacter hansenii* was augmented with silica-coated Nanofer 25 and STAR iron oxide nanoparticles and cellulose biosynthesis was attempted, and in the second, the purified BC material was used as a matrix into which iron oxide NPs were deposited on the BC nanofibers by co-precipitation synthesis. Two co-precipitation methods were conducted, reverse co-precipitation and NH$_3$ gas-enhanced co-precipitation.

Producing BC-IO NP composites in static and agitated culture media inoculated with *GAB* cells augmented with iron oxide NPs was problematic, for several reasons. Most notably, cellulose production by *GAB* was suppressed or stopped in some static and agitated samples. In addition, dispersion of iron oxide NPs in the growth media was poor. If the augmented growth media method for producing BC-iron oxide composites will be used in the future, it is important to control the dispersion of NPs so that that nanocomposites can be homogeneous and the processes reproducible. Methods for preventing aggregation and evenly distributing the NPs needs to be implemented to achieve nanomaterials. Other researchers have developed methods for dispersing NPs such as sonication during BC biogenesis, which can be problematic as sonication can affect *GAB* cells; other methods for obtaining colloidal stability of NPs in aqueous solutions include dispersion materials or molecules. Another drawback of producing BC-IO NPs composites during BC biosynthesis in the culture media is the presence of *GAB* cells, by-products, and the HS media which would need to be removed in order to have a product that contains only BC and iron oxide NPs. Removal of the *GAB* cells and other impurities is impossible to accomplish without damaging the iron oxide NPs. Currently, no method exists for removing impurities from the BC-IO NPs composites produced during BC biosynthesis in the culture media.

Therefore, the best method for making BC-IO NPs composites is using the purified BC material as a matrix and coating the BC nanofibers with iron oxide NPs by co-precipitation synthesis. Two co-precipitation methods were used, reverse co-precipitation and NH$_3$ gas-enhanced co-precipitation; the former produced Fe$_3$O$_4$ and γ-Fe$_2$O$_3$, whereas the latter produced γ-Fe$_2$O$_3$, α-Fe$_2$O$_3$ and FeO(OH). To obtain Fe$_3$O$_4$ and eliminate the formation of other iron oxides, in future experiments the co-precipitation synthesis reactions will be conducted in a nitrogen environment.

Reverse co-precipitation with concentrated NH_3 affected the BC, causing it to become more crystalline, and possibly more brittle, therefore the use of NH_3 gas, which might be gentler on the BC crystal structure, should be studied in more depth. The NH_3 gas-enhanced co-precipitation method should be improved before comparing to reverse co-precipitation: NH_3 gas should be applied from a tank with a flow meter. In future work, the reverse co-precipitation method and the NH_3 gas-enhanced in situ co-precipitation should be compared to determine the best method for synthesizing Fe_3O_4 in the BC matrix.

Augmentation of NPs (SiO_2 IO NP and STAR IO NP) in the bacterial culture medium produced nanocomposites in which the nanoparticles were physically trapped in the nanocellulose matrix as evidenced by FESEM. ATR-FTIR results indicate that SiO_2 IO NP and STAR IO NP were likely physically trapped in the nanocellulose fibers because IR spectra provided no evidence of hydrogen bonding. Furthermore, covalent bonds did not occur between nanoparticles and nanocellulose.

In BC-IO NP (syn) composites, ATR-FTIR results revealed OH band broadening indicative of increased hydrogen bonding which implied that the IO NPs (syn) coated on the BC fibers interact on a molecular level with the hydroxyl (OH) functional groups of the cellulose polymer, joining via hydrogen bonding of the OH groups on the surface of the NPs. In BC-IO NPs (syn), varying the concentrations of Fe^{2+} and Fe^{3+}, the iron ion precursors for Fe_3O_4 production, resulted in BC-IO NPs (syn) composites with different concentrations of Fe_3O_4 incorporated onto the bacterial nanocellulose fibers. These variations illustrated that composites of BC and iron oxide nanoparticles were engineered. This research demonstrated that BC is an excellent template for synthesizing iron oxide NPs and yields a composite with iron oxide NPs integrated with the cellulose fibers.

In summary, for future work on BC-IO NPs composites:

- Methods to disperse nanoparticles and prevent aggregation should be implemented in future production of BC-IO NPs composites during BC biosynthesis in altered culture media.

- Co-precipitation synthesis reaction will be conducted under nitrogen to obtain Fe_3O_4, and the results of reverse co-precipitation and NH_3 gas-enhanced in situ co-precipitation compared.

- The NH_3 gas-enhanced in situ co-precipitation method will be modified with a NH_3 gas tank supplied through a flow meter.

- Thermogravimetric analysis (TGA) will be conducted on samples to analyze the composition—the amounts of BC and iron oxide NPs in the BC-IO NPs composites (to study mass loading).

- Vibrating sample magnetometry (VSM) should be conducted to analyze the magnetic properties of the BC-IO NPs composites.

REFERENCES

1.   Jonas, R.; Farah, L. F. Production and Application of Microbial Cellulose. *Polym. Degrad. Stab.* 1998, *59*, (1–3), 101-106.

2.   Brown, R. M., Jr. Bacterial Cellulose. In *Cellulose: Structural and Functional Aspects*; Kennedy, J. F.; Phillips, G. O.; Williams, P. A., Eds.; Ellis Horwood: Chichester, 1989; pp 145-151.

3.   Bielecki, S., et al. Bacterial Cellulose. In *Biotechnology of Biopolymers: From Synthesis to Patents*; Steinbuechel, A.; Doi, Y., Eds.; Wiley-VCH Verlag: Weinheim, 2005; pp 381-434.

4.   Kondo, T. Nematic Ordered Cellulose Templates. In *Bacterial Nanocellulose: A Sophisticated Multifunctional Material*; Gama, M.; Gatenholm, P.; Klemm, D., Eds.; Taylor and Francis Group, LLC: Boca Raton, 2012; pp 113-142.

5.   White, D. G.; Brown, R. M. J. Prospects for the Commercialization of the Biosynthesis of Microbial Cellulose. In *Cellulose and Wood Chemistry and Technology*; Schuerech, C., Ed. John Wiley & Sons: New York, 1989; pp 573-590.

6.   Park, S. U., et al. The Possibility of Microbial Cellulose for Dressing and Scaffold Materials. *Int. Wound J.* 2012, 1-10.

7.   Klemm, D., et al. Cellulose: Fascinating Biopolymer and Sustainable Raw Material. *Angewandte Chem. Int. Ed.* 2005, *44*, (22), 3358–3393.

8.   Eichhorn, S. J., et al. Current International Research into Cellulose Nanofibres and Nanocomposites. *J. Mater. Sci.* 2010, *45*, 1–33.

9.   Hsieh, Y. Chemical Structure and Properties of Cotton. In *Cotton: Science and Technology*; Gordon, S.; Hsieh, Y., Eds.; Woodhead Publishing Ltd.: Cambridge, UK, 2007; pp 3-34.

10.   Hornung, M., et al. Optimizing the Production of Bacterial Cellulose in Surface Culture: Evaluation of Substrate Mass Transfer Influences on the Bioreaction (Part 1). *Eng. Life Sci.* 2006, *6*, (6), 537–545.

11.   Himmel, M. E., et al. Biomass Recalcitrance: Engineering Plants and Enzymes for Biofuels Production. *Science* 2007, *315*, 804-807.

12.   Bajpai, P. Biological Bleaching of Chemical Pulps. *Crit. Rev. Biotechnol.* 2004, *24*, 1-58.

13.   Kalia, S., et al. Cellulose-Based Bio- and Nanocomposites: A Review. *Int. J. Polym. Sci.* 2011, *2011*, 1-35.

14.   Jahn, A., et al. Characterization of Alkali Treated Flax Fibers by Means of FT Raman Spectroscopy and Environmental Scanning Electron Microscopy. *Spectrochim. Acta A* 2002, *58*, (10), 2271-2279.

15.   Battista, O. A. Molecular Weight of Cellulose Measurement of Average Degree of Polymerization. *Ind. Eng. Chem. Anal. Ed.* 1944, *16*, (6), 351-354.

16.   Watanabe, K., et al. Structural Features and Properties of Bacterial Cellulose Produced in Agitated Culture. *Cellulose* 1998, *5*, (3), 187-200.

17.   Vandamme, E. J., et al. Improved Production of Bacterial Cellulose and its Application Potential. *J. Polym. Degrad. Stabil.* 1998, *59*, 93-99.

18.   Keten, S., et al. Geometric Confinement Governs the Rupture Strength of H-bond Assemblies at a Critical Length Scale *Nano Lett.* 2008, *8*, (2), 743-748.

19.   Gindl, W.; Keckes, J. All-Cellulose Nanocomposite. *Polymer* 2005, *46*, (23), 10221-10225

20.   Liu, Y. Recent Progress in Fourier Transform Infrared (FTIR) Spectroscopy Study of Compositional, Structural, and Physical Attributes of Developmental Cotton Fibers. *Materials* 2013, *6*, 299-313.

21.   Nishino, T., et al. Elastic Modulus of the Crystalline Regions of Cellulose Polymorphs. *J. Polym. Sci. Part B: Polym. Phys.* 1995, *33*, (11), 1647-1651.

22.   Azizi-Samir, A. S., et al. Tangling Effect in Fibrillated Cellulose Reinforced Nanocomposites. *Macromolecules* 2004, *37*, 4313-4316.

23.   Hsieh, Y. C., et al. An Estimation of the Young's Modulus of Bacterial Cellulose Filaments. *Cellulose* 2008, *15*, (4), 507-513.

24.   Guhados, G., et al. Measurement of the Elastic Modulus of Single Bacterial Cellulose Fibers using Atomic Force Microscopy. *Langmuir* 2005, *21*, (14), 6642-6646.

25.   Ross, P., et al. Cellulose Biosynthesis and Function in Bacteria. *Microbiol. Rev.* 1991, *55*, 35-58.

26.   Yamanaka, S., et al. The Structure and Mechanical Properties of Sheets Prepared from Bacterial Cellulose. *J. Mater. Sci.* 1989, *24*, (9), 3141-3145.

27.   Page, D. H.; Elhosseiny, F. The Mechanical Properties of Single Wood Pulp Fibers. *J. Pulp Pap.-Can.* 1983, *84*, 99-100.

28.   Saito, T., et al. An Ultrastrong Nanofibrillar Biomaterial: the Strength of Single Cellulose Nanofibrils Revealed via Sonication-Induced Fragmentation. *Biomacromolecules* 2013, *14*, 248-253.

29.   Iwamoto, S., et al. Elastic Modulus of Single Cellulose Microfibrils from Tunicate Measured by Atomic Force Microscopy. *Biomacromolecules* 2009, *10*, 2571–2576

30.   Iwamoto, S., et al. The Effect of Hemicelluloses on Wood Pulp Nanofibrillation and Nanofiber Network Characteristics. *Biomacromolecules* 2008, *9*, 1022-1026.

31.   Sakurada, I., et al. Experimental Determination of the Elastic Modulus of Crystalline Regions in Oriented Polymers. *J. Polym. Sci.* 1962, *57*, (165), 651-660.

32.   Nishino, T.; Arimoto, N. All-Cellulose Composite Prepared by Selective Dissolving of Fiber Surface. *Biomacromolecules* 2007, *8*, 2712-2716.

33.   Walther, A., et al. Multifunctional High-Performance Biofibers Based on Wet-Extrusion of Renewable Native Cellulose Nanofibrils. *Advanced Materials* 2011, *23*, (26), 2924-2928.

34.   Henriksson, M., et al. Cellulose Nanopaper Structures of High Toughness *Biomacromolecules* 2008, *9*, 1579-1585.

35.   Eichhorn, S. J.; Young, R. J. The Young's Modulus of a Microcrystalline Cellulose. *Cellulose* 2001, *8*, 197-207.

36.   Nishi, Y., et al. The Structure and Mechanical Properties of Sheets Prepared from Bacterial Cellulose. *J. Mat. Sci.* 1990, *25*, (6), 2997-3001.

37.   Yano, H., et al. Optically Transparent Composites Reinforced with Networks of Bacterial Nanofibers. *Adv. Mater.* 2005, *17*, (2), 153-155.

38.   Nakagaito, A. N., et al. Bacterial Cellulose: the Ultimate Nano-scalar Cellulose Morphology for the Production of High-strength Composites. *Appl. Phys. A Mater. Sci. Process* 2005, *80*, 93-97.

39.   Soykeabkaew, N. All-cellulose Composites. PhD, University of London, London, 2007.

40.   Röder, T., et al. Crystallinity Determination of Native Cellulose-Comparison of Analytical Methods. *Lenzinger Ber.* 2006, *86*, 85-89.

41.   Aulin, C., et al. Nanoscale Cellulose Films with Different Crystallinities and Mesostructures-Their Surface Properties and Interaction with Water. *Langmuir* 2009, *25*, (13), 7675-7685.

42.   Czaja, W., et al. Structural Investigations of Microbial Cellulose Produced in Stationary and Agitated Culture. *Cellulose* 2004, *11*, 403-411.

43.   Terinte, N., et al. Overview on Native Cellulose and Microcrystalline Cellulose I Structure Studied by X-Ray Diffraction (WAXD): Comparison Between Measurement Techniques. *Lenzinger Ber.* 2011, *89*, 118-131.

44.   Lina, F., et al. Bacterial Cellulose for Skin Repair Materials. In *Biomedical Engineering: Frontiers and Challenges*; Fazel-Rezai, R., Ed. In-Tech: 2011.

45.   Krieger, J. Bacterial Cellulose Near Commercialization. *Chem. Eng.News* 1990, *68*, (21), 35-37.

46.   Schrecker, S. T.; Gostomski, P. A. Determining the Water Holding Capacity of Microbial Cellulose. *Biotechnol. Lett.* 2005, *27*, 1435-1438.

47. Costa, L. M. M., et al. Bacterial Cellulose Towards Functional Green Composite Materials. *J. Bionanosci.* 2011, *5*, (2), 167-172.

48. Kondo, T. Nematic Ordered Cellulose: Its Structure and Properties. In *Cellulose: Molecular and Structural Biology*; Brown, R. M. J.; Saxena, I. M., Eds.; Springer: New York, 2007; pp 285-305.

49. Hesse, S.; Kondo, T. Behavior of Cellulose Production of Acetobacter xylinum in ^{13}C- Enriched Cultivation Media Including Movements on Nematic Ordered Cellulose Templates. *Carbohydr. Polym.* 2005, *60*, 457-465.

50. Kondo, T., et al. Biodirected Epitaxial Nanodeposition of Polymers on Oriented Macromolecular Templates. *P. Natl. Acad. Sci. USA* 2002, *99*, (22), 14008-14013.

51. Czaja, W. K., et al. The Future Prospects of Microbial Cellulose in Biomedical Applications. *Biomacromolecules* 2007, *8*, (1), 1-12.

52. Shah, J.; Brown, M. Towards Electronic Paper Displays Made From Microbial Cellulose. *Appl. Microbiol. Biotechnol.* 2005, *66*, (4), 352–355.

53. Yang, Z. H., et al. Flexible Luminescent CdSe/Bacterial Cellulose Nanocomoposite Membranes. *Carbohydr. Polym.* 2012, *88*, (1), 173-178.

54. Sai, H., et al. Flexible Aerogels Based on Interpenetrating Network of Bacterial Cellulose and Silica by a Non-Supercritical Drying Process. *J. Mater. Chem. A* 2013, *1*, 7963-7970.

55. Iguchi, M., et al. Bacterial Cellulose–A Masterpiece of Nature's Arts. *J. Mater. Sci.* 2000, *35*, (2), 261-270.

56. Nata, I. F., et al. One-Pot Preparation of Amine-Rich Magnetite/Bacterial Cellulose Nanocomposite and its Application for Arsenate Removal. *Rsc. Adv.* 2011, *1*, (4), 625-631.

57. Food & Fertilizer Technology Center for the Asian and Pacific Region. Fermentation of Monascus Purpureus on Agri By-products to Make Colorful and Functional Bacterial Cellulose (Nata). www.agnet.org/library.php?func=view&id=20110716164214 (accessed 05/23/13).

58. Wikipedia. Nata de coco. en.wikipedia.org/wiki/Nata_de_coco (accessed 05/23/13).

59. Amazon. Coconut Gel (Nata de Coco)-12 oz by Laguna. www.amazon.com/Coconut-Gel-Nata-Coco-Laguna/dp/B00886ERWU (accessed 05/23/13).

60. Food & Fertilizer Technology Center for the Asian and Pacific Region. Processing of Nata de Pina. www.agnet.org/library.php?func=view&id=20110716235334 (accessed 05/23/13).

61. Barud, H. S., et al. Optically Transparent Membrane Based on Bacterial Cellulose/polycaprolactone. *Polímeros* 2013, *23*, (1), 135-138.

62.   Ifuku, S., et al. Surface Modification of Bacterial Cellulose Nanofibers for Property Enhancement of Optically Transparent Composites: Dependence on Acetyl-group DS. *Biomacromolecules* 2007, *8*, (6), 1973-1978.

63.   Nakamura, K. Antibacterial Mask Comprising Bacterial Cellulose and Silver Compounds, Antibacterial Filter for Mask, and Disinfection Method. 2011,

64.   Zhong, C. Y. Method for Manufacturing Air-filtering Bacterial Cellulose Face Mask. 2011167226, 2011.

65.   Surma-Slusarska, B., et al. Properties of Composites of Unbeaten Birch and Pine Sulphate Pulps with Bacterial Cellulose. *Fibres Text. East. Eur.* 2008, *16*, (6), 127-129.

66.   Cellulose Solutions, L.L.C. Dermafill™ Xylinum Cellulose: Advanced Science for Wound Management http://www.dermafill.com (accessed 06/23/12).

67.   Innovatec. Nanoskin®: Bacterial Cellulose Produced by Innovatec´s Biotechnology Research and Development http://www.innovatecs.com/index.html (accessed 06/03/12).

68.   Bielecki, S., et al. Improvements of *Gluconacetobacter xylinus* Nanocellulose Production Process. Presented at 239th ACS National Meeting, San Francisco,CA, March 21-25, 2010.

69.   CP Kelco. CELLULON® PX Microfibrous Cellulose. http://www.cpkelco.com/market_household/prod-cellulon.html (accessed 05/23/13).

70.   Alvarez, O. M., et al. Effectiveness of a Biocellulose Wound Dressing for the Treatment of Chronic Venous Leg Ulcers: Results of a Single Center Randomized Study Involving 24 Patients. *Wounds* 2004, *16*, (7), 224–233.

71.   Torres, F. G., et al. Biocompatibility of Bacterial Cellulose Based Biomaterials. *J. Funct. Biomater.* 2012, *3*, 864-878.

72.   Siró, I.; Plackett, D. Microfibrillated Cellulose and New Nanocomposite Materials: A Review. *Cellulose* 2010, *17*, (3), 459-494.

73.   Pecoraro, E., et al. Bacterial Cellulose from Glucanacetobacter xylinus: Preparation, Properties, and Applications In *Monomers, Polymers and Composites from Renewable Resources*; Gandini, A.; Balgacem, M. N., Eds.; Elsevier Science: 2009; pp 369–384.

74.   de Olyveira, G. M., et al. Bacterial Nanocellulose for Medicine Regenerative. *J. Nanotechnol. Eng. Med.* 2012, *2*, (3), 1-8.

75.   Petersen, N.; Gatenholm, P. Bacterial Cellulose-based Materials and Medical Devices: Current State and Perspectives. *Appl. Microbiol. Biotechnol.* 2011, *91*, 1277-1286.

76.   Gatenholm, P., et al. Effect of Cultivation Conditions on the Structure and Morphological Properties of BNC Biomaterials with a Focus on Vascular Grafts. In *Bacterial Nanocellulose: A Sophisticated Multifunctional Material*; Gama, M.; Gatenholm, P.; Dieter, K., Eds.; Taylor and Francis Group: Boca Raton, 2013; pp 19-42.

77.   Klemm, D., et al. Bacterial Synthesized Cellulose - Artificial Blood Vessels for Microsurgery. *Prog. Polym. Sci.* 2001, *26*, (9), 1561-1603.

78.   Fu, L., et al. Present Status and Applications of Bacterial Cellulose-based Materials for Skin Tissue Repair. *Carbohydr. Polym.* 2013, *92*, (2), 1432-1442.

79.   Fontana, J. D., et al. *Acetobacter* Cellulose Pellicle as a Temporary Skin Substitute. *Appl. Biochem. Biotechnol.* 1990, *24-25*, 253-264.

80.   Zaborowska, M., et al. Microporous Bacterial Cellulose as a Potential Scaffold for Bone Regeneration. *Acta. Biomater.* 2010, *6*, (7), 2540-2547.

81.   Svensson, A., et al. Bacterial Cellulose as a Potential Scaffold for Tissue Engineering of Cartilage. *Biomaterials.* 2005, *26*, (4), 419-431.

82.   Watanabe, K., et al. A New Bacterial Cellulose Substrate for Mammalian Cell Culture. *Cytotechnology* 1993, *13*, (2), 107-114.

83.   Millon, L. E.; Wan, W. K. The Polyvinyl Alcohol-bacterial Cellulose System as a New Nanocomposite for Biomedical Applications. *J. Biomed. Mater. Res. B* 2006, *79*, (2), 245-253.

84.   Portal, O., et al. Microbial Cellulose Wound Dressing in the Treatment of Non-healing Lower Extremity Ulcers. *Wounds* 2009, *21*, (1), 1-3.

85.   Solway, D. R., et al. A Parallel Open-label Trial to Evaluate Microbial Cellulose Wound Dressing in the Treatment of Diabetic Foot Ulcers. *Int. Wound J.* 2011, *8*, (1), 69-73.

86.   Solway, D. R., et al. Microbial Cellulose Wound Dressing in the Treatment of Skin Tears in the Frail Elderly. *Wounds* 2010, *22*, (1), 17-19.

87.   Maneerung, T., et al. Impregnation of Silver Nanoparticles into Bacterial Cellulose for Antimicrobial Wound Dressing. *Carbohydr. Polym.* 2008, *72*, (1), 43-51.

88.   Ricci, E. B., et al. Microcrystalline Cellulose Membrane for Re-epithelisation of Chronic Leg Wounds: A Prospective Open Study. *Int. Wound J.* 2010, *7*, 438–447.

89.   Czaja, W., et al. Microbial Cellulose—the Natural Power to Heal Wounds. *Biomaterials* 2006, *27*, (2), 145–151.

90.   Cook, J. R. Amine Functionalization of Bacterial Cellulose for Targeted Delivery Applications. University of Western Ontario, London, Ontario, Canada, 2013.

91.   Müller, A., et al. The Biopolymer Bacterial Nanocellulose as Drug Delivery System: Investigation of Drug Loading and Release Using the Model Protein Albumin. *J. Pharm. Sci.* 2013, *102*, (2), 579-592.

92.   Almeida, I. F., et al. Bacterial Cellulose Membranes as Drug Delivery Systems: an In Vivo Skin Compatibility Study. *Eur. J. Pharm. Biopharm.* 2013, *available online 20 August 2013 http://www.sciencedirect.com/science/article/pii/S0939641113002877*,

93. Mohd Amin, M. C., et al. Stimuli-responsive Bacterial Cellulose-g-poly (acrylic acid-co-acrylamide) Hydrogels for Oral Controlled Release Drug Delivery. *Drug Dev. Ind. Pharm.* 2013, 1-10.

94. Trovatti, E., et al. Biocellulose Membranes as Supports for Dermal Release of Lidocaine. *Biomacromolecules* 2011, *12*, 4162-4168.

95. Costa, L. M. M., et al. Nanopores Structure in Electrospun Bacterial Cellulose *J. Biomater. Nanobiotech.* 2012, *3*, 92-96.

96. Vitta, S., et al. Magnetically Responsive Bacterial Cellulose: Synthesis and Magnetic Studies. *J. Appl. Phys.* 2010, *108*, (5),

97. Johnson, A., et al. Highly Hydrated Poly(allylamine)/Silica Magnetic Resin. *J. Nanoparticle. Res.* 2011, *10*, (1), 4881-4895.

98. Fernandes, S. C., et al. Bioinspired Antimicrobial and Biocompatible Bacterial Cellulose Membranes Obtained by Surface Functionalization with Aminoalkyl Groups. *ACS Appl. Mater. Interfaces.* 2013, *5*, (8), 3290-3297.

99. Johnson, A. K., et al. Novel Method for Immobilization of Enzymes to Magnetic Nanoparticles. *J. Nanopart. Res.* 2008, *10*, (6), 1009-1025.

100. Tartaj, P., et al. Advances in Magnetic Nanoparticles for Biotechnology Applications. *J. Magn. Magn. Mater.* 2005, *290*, 28-34.

101. Zhu, H., et al. Biosynthesis of Spherical Fe_3O_4/Bacterial Cellulose Nanocomposites as Adsorbents for Heavy Metal Ions. *Carbohydr. Polym.* 2011, *86*, 1558-1564.

102. Katepetch, C.; Rujiravanit, R. Synthesis of Magnetic Nanoparticle into Bacterial Cellulose Matrix by Ammonia Gas-enhancing In Situ Co-precipitation Method. *Carbohydr.Polym.* 2011, *86*, (1), 162-170.

103. Chesworth, W., Ed. Iron Oxides. In *Encyclopedia of Soil Science*; Springer: New York, 2008; pp 363-368.

104. NANOIRON, s.r.o. Contaminants. http://www.nanoiron.cz/en/contaminants (accessed Jun 23, 2012).

105. Han, H., et al. Silica Coated Magnetic Nanoparticles for Separation of Nuclear Acidic Waste. *J. Appl. Phys.* 2010, *107*, 09B520.

106. NANOIRON, s.r.o. Production and Application of Nanoscale Zero-Valent Iron (nZVI) http://www.nanoiron.cz (accessed Jun 23, 2012).

107. Oshima, T., et al. Preparation of Phosphorylated Bacterial Cellulose as an Adsorbent for Metal Ions. *React. Funct. Polym.* 2008, *68*, (1), 376-383.

108.   Predoi, D., et al. Synthesis and Characterization of Bio-compatible Maghemite Nanoparticles. *Dig. J. Nanomater. Bios.* 2010, *5*, (3), 779-786.

109.   Luo, X., et al. In Situ Synthesis of Fe_3O_4/Cellulose Microspheres with Magnetic-induced Protein Delivery. *J. Mater. Chem. A* 2009, *19*, 3538-3545.

110.   Ito, R., et al. Magnetic Granules: a Novel System for Specific Drug Delivery to Esophageal Mucosa in Oral Administration. *Int. J. Pharm.* 1990, *61*, (1-2), 109-117.

111.   Fragouli, D., et al. Superparamagnetic Cellulose Fiber Networks Via Nanocomposite Functionalization. *J. Mater. Chem.* 2012, *22*, 1662-1666.

112.   Wu, W., et al. Preparation and Properties of Magnetic Cellulose Fiber Composites. *BioResources* 2011, *6*, (3), 3396-3409.

113.   Park, M., et al. Electromagnetic Nanocomposite of Bacterial Cellulose Using Magnetite Nanoclusters and Polyaniline. *Colloids Surf. B* 2013, *102*, 238-242.

114.   Olsson, R. T., et al. Extraction of Microfibrils from Bacterial Cellulose Networks for Electrospinning of Anisotropic Biohybrid Fiber Yarns. *Macromolecules* 2010, *43*, (9), 4201-4209.

115.   Yamada, Y. Taxonomy of Acetic Acid Bacteria Utilized for Vinegar Fermentation. Presented at First International Symposium on Insight into the World of Indigenous Fermented Foods for Technology Development and Food Safety, Bangkok, Thailand, August 13-17, 2003.

116.   Andrés-Barrao, C., et al. Genome Sequences of the High-acetic Acid-resistant Bacteria *Gluconacetobacter europaeus* LMG 18890T and *G. europaeus* LMG 18494 (reference strains), *G. europaeus* 5P3, and *Gluconacetobacter oboediens* 174Bp2 (Isolated from Vinegar). *J. Bacteriol.* 2011, *193*, (10), 2670–2671.

117.   Hungund, B. S.; Gupta, S. G. Improved Production of Bacterial Cellulose From *Gluconacetobacter persimmonis* GH-2. *Microbial. Biochem. Technol.* 2010, *2*, 127-133.

118.   Cleenwerck, I., et al. Phylogeny and Differentiation of Species of the Genus *Gluconacetobacter* and Related Taxa Based on Multilocus Sequence Analyses of Housekeeping Genes and Reclassification of *Acetobacter xylinus* subsp. *sucrofermentans* as *Gluconacetobacter sucrofermentans* (Toyosaki et al.1996) sp. nov., comb. nov. *Int. J. Syst. Evol. Microbiol.* 2010, *60*, 2277-2283.

119.   LPSN. Genus *Gluconacetobacter*. http://www.bacterio.net/*gluconacetobacter*.html (accessed May 23,2012).

120.   Saxena, I.; Brown, J. R. M. Biosynthesis of Bacterial Cellulose. In *Bacterial Nanocellulose*; Gama, M.; Gatenholm, P.; Klemm, D., Eds.; CRC Press: Boca Raton, 2012.

121.   ATCC. *Gluconacetobacter hansenii* (Gossele et al.) Yamada et al. (ATCC® 23769™). http://www.atcc.org/Products/Cells_and_Microorganisms/Bacteria/Alphanumeric_Genus__Species/23769.aspx (accessed May 23, 2012).

122.   ATCC. *Gluconacetobacter hansenii* (Gossele et al.) Yamada et al. (ATCC® 53582™) http://www.atcc.org/Products/Cells_and_Microorganisms/Bacteria/Alphanumeric_Genus__ Species/23769.aspx (accessed May 23, 2012).

123.   Trovatti, E. Bacterial Cellulose. In *Biopolymer Nanocomposites: Processing, Properties, and Applications*; Dufresne, A.; Thomas, S.; Pothan, L. A., Eds.; John Wiley & Sons: New Jersey, 2013; pp 339-366.

124.   Cousins, S. K.; Brown, R. M., Jr. Cellulose I Microfibril Assembly-Computational Molecular Mechanics Energy Analysis Favours Bonding by Van der Waals Forces as the Initial Step in Crystallization. *Polymer* 1995, *36*, 3885–3888.

125.   Ring, G. J. F. Study of Polymerization Kinetics of Bacterial Cellulose through Gel Permeation Chromatography. In *Cellulose and Other Natural Polymer Systems: Biogenesis, Structure, and Degradation*; Brown, R. M. J., Ed. Plenum: New York, 1982; pp 299-325.

126.   Hestrin, S., et al. Synthesis of Cellulose by Resting Cells of *Acetobacter xylinum*. *Nature* 1947, *159*, (64), 64-65.

127.   Hestrin, S.; Mager, J. Colour Test for Identification of Glucose. *Analyt. Chem.* 1947, *19*, 1032-1035.

128.   Schramm, M., et al. Synthesis of Cellulose by *Acetobacter xylinum*. 3. Substrates and Inhibitors. *Biochem. J.* 1957, *67*, (4), 669–679.

129.   Schramm, M.; Hestrin, S. Synthesis of Cellulose by Acetobacter xylinum. 2. Preparation of Freeze-dried Cells Capable of Polymerizing Glucose to Cellulose. *Biochem. J.* 1954, *58*, (2), 345–352.

130.   Frantz, E.; Schiebold, E. Beitraege zur Struktur der Bakterien Cellulose. *J. Makromol. Chem.* 1943, *1*, (3), 4-16.

131.   Muhlethaler, K. The Structure of Bacterial Cellulose. *Biochim. Biophys. Acta* 1949, *3*, (4), 527-535.

132.   Masaoka, S., et al. Production of Cellulose from Glucose by Acetobacter xylinum. *J. Ferment. Bioeng.* 1993, *75*, (1), 18–22.

133.   Kralisch, D.; Hessler, N. Large-Scale Production of BNC: State and Challenges. In *Bacterial NanoCellulose: A Sophisticated Multifunctional Material* Gama, M.; Gatenholm, P.; Klemm, D., Eds.; CRC Group Boca Raton, 2012; pp 43-71

134.   Costeron, J. W. The Role of Bacterial Cellulose Exopolysaccharides in Nature and Disease. *J. Ind. Microbiol. Biotechnol.* 1999, *22*, 551-563.

135.   Williams, W. S.; Cannon, R. E. Alternative Environmental Roles for Cellulose Produced by Acetobacter xylinum. *Appl. Environ. Microbiol.* 1989, *55*, 2448-2452.

136. Cook, K.; Colvin, R. J. Evidence for a Beneficial Influence of Cellulose Production on Growth of *Acetobacter xylinum* in Liquid Medium. *Curr. Microbiol.* 1980, *3*, 203-205.

137. Schramm, M.; Hestrin, S. Factors Affecting Production of Cellulose at the Air/Liquid Interface of a Culture of *Acetobacter xylinum*. *J. Gen. Microbiol.* 1954, *11*, (123),

138. Valla, S.; Kjosbakken, J. K. Cellulose-negative Mutants of Acetobacter xylinum. *J. Gen. Microbiol.* 1982, *128*, 1401-1408.

139. Okamoto, T.; Yamano, S. Cloning of the Acetobacter xylinum Cellulase Gene and its Expression in Escherichia coli and Zymomonas mobilis. *Appl. Biochem. Biotechnol.* 1994, *42*, (4), 563-568.

140. Yoshinaga, F., et al. Research Progress in Production of Bacterial Cellulose by Aeration and Agitation Culture and its Application as a New Industrial Material. *Biosci. Biotechnol. Biochem.* 1997, *61*, (2), 219-224.

141. Krystynowicz, A., et al. Factors Affecting the Yield and Properties of Bacterial Cellulose. *J. Ind. Microbiol. Biotechnol.* 2002, *29*, (4), 189-195.

142. Kouda, T., et al. Effect of Agitator Configuration on Bacterial Cellulose Productivity in Aerated and Agitated Culture. *J. Ferment. Bioeng.* 1997, *83*, (4), 371-376.

143. Chao, Y., et al. Bacterial Cellulose Production Under Oxygen-enriched Air at Different Fructose Concentrations in a 50-liter, Internal-loop Airlift Reactor. *Appl. Microbiol. Biotechnol.* 2001, *55*, 673–679.

144. Hu, Y.; Catchmark, J. M. Formation and Characterization of Spherelike Bacterial Cellulose Particles Produced by Acetobacter xylinum JCM 9730 Strain. *Biomacromolecules* 2010, *11*, (7), 1727-1734.

145. Chao, Y., et al. Bacterial Cellulose Production by Acetobacter xylinum in a 50-L Internal-Loop Airlift Reactor. *Biotechnol. Bioeng.* 2000, *68*, (3), 345-352.

146. Naritomi, T., et al. Effect of Lactate on Bacterial Cellulose Production from Fructose in Continuous Culture. *J. Ferment. Bioeng.* 1998, *85*, 89–95.

147. Kouda, T., et al. Effect of Agitator Configuration on the Productivity of Bacterial Cellulose Production. *J. Ferment. Bioeng.* 1997, *83*, 371–376.

148. Kouda, T., et al. Characterization of Non-Newtonian Behavior During Mixing of Bacterial Cellulose in a Bioreactor. *J. Ferment. Bioeng.* 1996, *82*, 382–386.

149. Sakairi, N., et al. A Method for Direct Harvest of Bacterial Cellulose Filaments During Continuous Cultivation of Acetobacter xylinum. *Carbohydr. Polym.* 1998, *35*, 223–227.

150. Büchs, J. Introduction to Advantages and Problems of Shaken Cultures. *Biochem. Eng. J.* 2001, *7*, (2), 91-98.

151.   Ruka, D. R., et al. Altering the Growth Conditions of *Gluconacetobacter xylinus* to Maximize the Yield of Bacterial Cellulose. *Carbohydr. Polym.* 2012, *89*, (2), 613-622.

152.   Chao, Y. P., et al. Bacterial Cellulose Production by Acetobacter xylinum in a 50-L Internal-Loop Airlift Reactor. *Biotechnology and Bioengineering* 2000, *68*, (3), 345-352.

153.   Thompson, D. N.; Hamilton, M. A. Production of Bacterial Cellulose From Alternate Feedstocks. *Appl. Biochem. Biotechnol.* 2001, *93*, 503-513.

154.   Cavka, A., et al. Production of Bacterial Cellulose and Enzyme from Waste Fiber Sludge. *Biotechnol. for Biofuels* 2013, *6*, 25-35.

155.   Sutanto, A. Pineapple Liquid Waste as Nata de Pina Raw Material. *Makara Teknologi* 2012, *16*, (1), 63-67.

156.   Wu, J. M.; Liu, R. H. Cost-effective Production of Bacterial Cellulose in Static Cultures Using Distillery Wastewater. *J. Biosci. Bioeng.* 2013, *115*, (3), 284-290.

157.   Nobles, D. R. J.; Brown, R. M. J. Transgenic Expression of *Gluconacetobacter xylinus* Strain ATCC 53582 Cellulose Synthase Genes in the Cyanobacterium *Synechococcus leopoliensis* Strain UTCC 100. *Cellulose* 2008, *15*, 691-701.

158.   Brown, R. M. J. In *What We Have Learned About Cellulose Biosynthesis from Acetobacter xylinum (Gluconacetobacter xylinus): A Brief History and Future Prospects*, 245th National Meeting and Exposition of the American Chemical Society: The First International Symposium on Bacterial Nanocellulose Division of Cellulose and Renewable Materials, New Orleans, LA, 2013; American Chemical Society: New Orleans, LA, 2013.

159.   NANOIRON, s.r.o. NANOFER STAR: Air-Stable nZVI Powder. http://www.nanoiron.cz/en/nanofer-star (accessed Jun 23, 2012).

160.   Slunský, J. Production of Zero-Valent Iron Nanoparticles (nZVI) for In-Situ Groundwater Remediation Including Recent Field Scale Application and Remediation Experience. Presented at Innovative Environmental Assessment and Remediation Technology, Kennesaw, GA, September 12-13, 2012.

161.   Liu, Q., et al. A Novel Two-Step Silica-Coating Process for Engineering Magnetic Nanocomposites. *Chem. Mater.* 1998, *10*, 3936-3940.

162.   NANOIRON, s.r.o. NANOFER 25 MSDS, 2010. NANOFER 25 slurry. http://www.nanoiron.cz/images/stories/msds_nanofer_25.pdf (accessed Jun 23, 2012).

163.   NANOIRON, s.r.o. NANOFER 25 Product Ageing (nZVI Degradation). http://www.nanoiron.cz/en/product-ageing (accessed Jun 23, 2012).

164.   NANOIRON, s.r.o. NANOFER 25 Slurry. http://www.nanoiron.cz/en/nanofer-25 (accessed Jun 23, 2012).

165. NANOIRON, s.r.o. Zero-Valent Iron Nanoparticles (nZVI) in the Norm of Dry Powder and Water Slurry Products. http://www.nanoiron.cz/en/products (accessed Jun 23, 2012).

166. Kazemzadeh, H., et al. Synthesis of Magnetite Nano-particles by Reverse Co-precipitation. *Int. J. Mod. Phys. Conf. Ser.* 2012, *5* 160-167.

167. Alibeigi, S.; Vaezi, M. R. Phase Transformation of Iron Oxide Nanoparticles by Varying the Molar Ratio of Fe2+:Fe3+. *Chem. Eng. Technol.* 2008, *31*, (11), 1591-1596.

168. Mahmed, N., et al. Room Temperature Synthesis of Magnetite (Fe3–δO4) Nanoparticles by a Simple Reverse Co-Precipitation Method. *IOP Conf. Series: Mater. Sci. Eng.* 2011, *18*, 1-4.

169. Liu, S., et al. Magnetic Responsive Cellulose Nanocomposites and Their Applications. In *Cellulose – Medical, Pharmaceutical and Electronic Applications*; Intech: 2013.

170. Sourty, E., et al. Characterization of Magnetic Membranes Based on Bacterial and Man-Made Cellulose. *Cellulose* 1998, *5*, (1), 5-17.

171. Eivari, H. A.; Rahdar, A. Some Properties of Iron Oxide Nanoparticles Synthesized in Different Conditions. *A.World Applied Programming* 2013, *3*, (2), 52-55.

172. Eivari, H. A., et al. Preparation of Super Paramagnetic Iron Oxide Nanoparticles and Investigation Their Magnetic Properties. *Int. J. Sci. Eng. Inv.* 2012, *1*, (3), 70-72.

173. Mizutani, N., et al. Effect of Ferrous/Ferric Ions Molar Ratio on Reaction Mechanism for Hydrothermal Synthesis of Magnetite Nanoparticles. *Bull. Mater. Sci.* 2008, *31*, (5), 713-717.

174. Varma, M. V. K.; Amareshwar, P. Preparation and Characterization of Superparamagnetic Magnetite (Fe3o4) Nanoparticles *Curr. Pharma Res.* 2011, *1*, (4), 300-305.

175. Reed, S. J. B. *Electron Microbe Analysis and Scanning Electron Microscopy in Geology*. Cambridge University Press: Cambridge 1996; pp 43-53.

176. Thygesen, A., et al. On the Determination of Crystallinity and Cellulose Content in Plant Fibres. *Cellulose* 2005, *12*, 563-576.

177. Rabek, J. F. *Experimental Methods in Polymer Chemistry*. Wiley-Interscience: Chichester, 1980; p 505.

178. Saleh, N., et al. Surface Modifications Enhance Nanoiron Transport and NAPL Targeting in Saturated Porous Media. *Environ. Sci. Technol.* 2007, *24*, 45–57.

179. Phenrat, T., et al. Aggregation and Sedimentation of Aqueous Nanoscale Zerovalent Iron Dispersions. *Environ. Sci. Technol.* 2007, *41*, 284–290.

180. Elliott, D. W.; Zhang, W. X. Field Assessment of Nanoscale BimetallicParticles for Groundwater Treatment. *Environ.Sci.Technol.* 2001, *35*, 4922-4926.

181.   Cundy, A. B., et al. Use of Iron-Based Technologies in Contaminated Land and Groundwater Remediation: a Review. *Sci. Total. Environ.* 2008, *400*, 42-51.

182.   Geng, B., et al. Preparation of Chitosan-stabilized Fe0 Nanoparticles for Removal of Hexavalent Chromium in Water. *Sci. Total. Environ.* 2009, *407*, 4994–5000.

183.   Chawla, P. R., et al. Microbial Cellulose: Fermentative Production and Applications. *Food Technol. Biotechnol.* 2009, *47*, (2), 107-124.

184.   Schrader, B. *Infrared and Raman Spectroscopy: Methods and Applications*. VCH: Weinheim, 1995; pp 7-62.

185.   Socrates, G. *Infrared and Raman Characteristic Group Frequencies: Tables and Charts*. Wiley: New York, 2004; pp 1-366.

186.   Chalmers, J.; Griffiths, P. *Handbook of Vibrational Spectroscopy: Sample Characterization and Spectral Data Processing*. John Wiley & Sons, Ltd: West Sussex, 2002; Vol. 3.

187.   Mayo, D., et al. *Course Notes on the Interpretation of Infrared and Raman Spectra*. John Wiley and Sons, Inc.: Hoboken, 2004.

188.   Gotic, M.; Music, S. Mossbauer, FT-IR and FESEM Investigation of Iron Oxides Precipitated from $FeSO_4$ Solutions. *J. Mol. Struct.* 2007, *834*, 445–453.

189.   Ashori, A., et al. Bacterial Cellulose/Silica Nanocomposites: Preparation and Characterization. *Carbohyd. Polym.* 2012, *90*, (1), 413-418.

190.   Kalia, S., et al. Pretreatments of Natural Fibers and their Application as Reinforcing Material in Polymer Composites. *Polym. Eng. Sci.* 2009, *49*, (7), 1253-1272.

191.   Fan, M., et al. Fourier Transform Infrared Spectroscopy for Natural Fibres. In *Fourier Transform-Materials Analysis* [Online]; Salih, M., Ed.; InTech: New York 2012; www.interchopen.com/books/fourier-transform-materials-analysis/fourier-transform-infrared-spectroscopy-for-natural-fibres (accessed July 11, 2013).

192.   Oh, S., et al. Crystalline Structure Analysis of Cellulose Treated with Sodium Hydroxide and Carbon Dioxide by Means of X-ray Diffraction and FTIR Spectroscopy. *Carbohydr. Res.* 2005, *340*, 2376-2391.

193.   Merlic, C.A. Introduction to IR Spectra, 2000. Web Spectra: Probems in NMR and IR Spectroscopy. http://www.chem.ucla.edu/~webspectra/irintro.html (accessed May 7, 2013).

194.   Kondo, T.; Sawatari, C. A Fourier Transform Infra-red Spectroscopic Analysis of the Character of Hydrogen Bonds in Amorphous Cellulose. *Polymer* 1996, *37*, (3), 393-399.

195.   Unger, K. Surface Structure of Amorphous and Crystalline Porous Silicas: Status and Prospects In *The Colloid Chemistry of Silica*; Bergna, H., Ed. American Chemical Society: Washington, 1994; Vol. 234, pp 165-181.

196.   Ji, L.; Zhang, X. Ultrafine Polyacrylonitrile/Silica Composite Fibers via Electrospinning. *Mater. Lett.* 2008, *62*, 2161-2164.

197.   Jubb, A. M.; Allen, H. C. Vibrational Spectroscopic Characterization of Hematite, Maghemite, and Magnetite Thin Films Produced by Vapor Deposition. *ACS Appl. Mater. Interfaces* 2010, *2*, (10), 2804-2812.

198.   Jassby, D. Impact of Particle Aggregation on Nanoparticle Reactivity. PhD, Duke University, Durham, NC, 2011.

199.   Feng, Y. Y., et al. A Mechanically Strong, Flexible and Conductive Film Based on Bacterial Bellulose/Graphene Nanocomposite. *Carbohydr.Polym.* 2012, *87*, (1), 644-649.

200.   Wang, Y. Cellulose Fiber Dissolution in Sodium Hydroxide Solution at Low Temperature: Dissolution Kinetics and Solubility Improvement. PhD, Georgia Institute of Technology, Atlanta, GA, 2008.

201.   Isogai, A.; Atalla, R. H. Dissolution of Cellulose in Aqueous NaOH Solutions. *Cellulose* 1998, *5*, 309-319.

202.   Fike, G. MadSci Network, Boston, MA. Personal communication, 2009.

203.   Shibazaki, H., et al. Mercerization and Acid Hydrolysis of Bacterial Cellulose. *Cellulose.* 1997, *4*, 75-87.

204.   Wanichapichart, P., et al. Chain Scission and Anti-fungal Effect of Electron Beam on Cellulose Membrane. *Rad. Phys. Chem.* 2012, *81*, 949–953.

205.   Dias, C. R., et al. Structure of Water in Asymmetric Cellulose Ester Membranes - an ATR-FTIR study. *J. Membr. Sci.* 1998, *138*, (2), 259-267.

206.   Garside, P.; Wyeth, P. Identification of Cellulosic Fibers by FTIR Spectroscopy: Thread and Single Fibre Analysis by Attenuated Total Reflectance. *Studies in Conserv.* 2003, *48*, (4), 269-275.

207.   Yang, H., et al. Films Prepared from Electrosterically Stabilized Nanocrystalline Cellulose. *Langmuir* 2012, *28*, (20), 7834-7842.

208.   Schwanninger, M., et al. Effects of Short-time Vibratory Ball Milling on the Shape of FT-IR Spectra of Wood and Cellulose. *Vib. Spectrosc.* 2004, *36*, 23–40.

209.   Todar, K. Glycobiology Analysis Manual: Bacterial Endotoxin. *Todar's Online Textbook of Bacteriology* [Online] 2012, http://www.textbookofbacteriology.net (accessed June 4, 2013).

210.   McNaught, A. D.; Wilkinson, A. International Union of Pure and Applied Chemistry: Compendium of Chemical Terminology. http://goldbook.iupac.org (accessed 08/19/2012).

211. Sockalingum, G. D., et al. ATR-FTIR Spectroscopic Investigation of Imipenem-susceptible and -Resistant Pseudomonas Aeruginosa Isogenic Strains. *Biochem. Biophys. Res. Commun.* 1997, *232*, (1), 240-246.

212. Nivens, D. E., et al. Multichannel ATR/FT-IR Spectrometer for On-line Examination of Microbial Biofilms. *Appl. Spectrosc.* 1993, *47*, 668–671.

213. Jiang, W., et al. Elucidation of Functional Groups on Gram-positive and Gram-negative Bacterial Surfaces using Infrared Spectroscopy. *Langmuir* 2004, *20*, (26), 11433-11442.

214. Lambert, J. B., et al. *Introduction to Organic Spectroscopy*. Macmillan: New York, 1987.

215. Brandenburg, K.; Seydel, U. Fourier Transform Infrared Spectroscopy of Cell Surface Polysaccharides. In *Infrared Spectroscopy of Biomolecules*; Mantsch, H. H.; Chapman, D., Eds.; John Wiley and Sons New York, 1996; pp 203-237.

216. O'Connor, R. T., et al. Applications of Infrared Absorption Spectroscopy to Investigations of Cotton and Modified Cottons. Part I: Physical and Crystalline Modifications and Oxidation *Textile Res. J.* 1958, *28*, 382–392.

217. Nelson, M. L., et al. Relation of Certain Infrared Bands to Cellulose Crystallinity and Crystal Lattice Type. Part II. A New Infrared Ratio for Estimation of Crystallinity in Celluloses I and II. *J. Appl. Polym. Sci.* 1964, *8*, (3), 1325–1341.

218. Ruan, D. Z., L.N.; Mao, Y.; Zeng, M.; Li, X.B. Microporous Membranes Prepared from Cellulose in NaOH/thiourea Aqueous Solution. *J. Membr.Sci.* 2004, *241*, (2), 265–274.

219. Colom, X.; Carrillo, F. Crystallinity, Crystallinity Changes in Lyocell and Viscose-type Fibres by Caustic Treatment. *Eur. Polym. J.* 2002, *11*, 2225–2230.

220. Cael, J. J., et al. Infrared and Raman Spectroscopy of Carbohydrates. Normal Coordinate Analysis of Cellulose I. *J. Chem. Phys.* 1975, *62*, 1145-1153.

221. Kacurakova, M., et al. Molecular Interactions in Bacterial Cellulose Composites Studied by 1D FT-IR and Dynamic 2D FT-IR Spectroscopy. *Carbohydr. Res.* 2002, *337*, (12), 1145-1153.

222. Grande, C. J., et al. Development of Self-assembled Bacterial Cellulose-starch Nanocomposites. *Mat. Sci. Eng .C-Bio. S* 2009, *29*, (4), 1098-1104.

223. Kirwan, L. J., et al. In Situ FTIR-ATR Examination of Poly(acrylic acid) Adsorbed onto Hematite at Low pH *Langmuir* 2003, *19*, 5802–5807.

224. Nyquist, R.; Kagel, R. *Handbook of Infrared and Raman Spectra of Inorganic Compounds and Organic Salts: Infrared Spectra of Inorganic Compounds* Academic Press, Inc.: San Diego, 1997; Vol. 4, p 495.

225. Cornell, R. M.; Schwertmann, U. *The Iron Oxides: Structure, Properties, Reactions, Occurrences and Uses*. Wiley-VCH Verlag: Weinheim, 2003.

226. Daniel-da-Silva, A., et al. In Situ Synthesis of Magnetite Nanoparticles in Carrageenan Gels *Biomacromolecules* 2007, *8*, 2350-2357.

227. Theppaleak, T., et al. Synthesis of Water Dispersible Magnetite Nanoparticles in the Presence of Hydrophilic Polymers. *Polym. Bull.* 2009, *63*, 79–90.

228. Saikia, B., et al. Fourier Transform Infrared Spectroscopic Estimation of Crystallinity in SiO(2) Based Rocks. *B. Mater. Sci.* 2008, *31*, (5), 775-779.

APPENDIX

Table 1:

Table of infrared spectroscopy absorption frequencies and assignments for all materials produced including bacterial cellulose (NaOH-treated BC-STAT and BC-AGIT samples, and BC-STAT and BC-AGIT samples treated with DI H_2O sonication), NaOH-treated microcrystalline cellulose (MC), synthesized iron oxide nanoparticles (IO NPs (syn)), silica-coated iron oxide nanoparticles (SiO_2 IO NPs), iron oxide-coated zero-valent iron nanoparticles (STAR IO NPs), and bacterial cellulose-iron oxide nanoparticle composite samples BC-SiO_2 IO NPs-STAT, BC-SiO_2 IO NPs-AGIT, BC-STAR IO NPs,and BC-IO NPs (syn).

Table 1: Infrared spectroscopy absorption frequencies and assignments for all materials produced including bacterial cellulose (NaOH-treated BC-STAT and BC-AGIT samples, and BC-STAT and BC-AGIT samples treated with DI H_2O sonication), NaOH-treated microcrystalline cellulose (MC), synthesized iron oxide nanoparticles (IO NPs (syn)), silica-coated iron oxide nanoparticles (SiO$_2$ IO NPs), iron oxide-coated zero-valent iron nanoparticles (STAR IO NPs), and bacterial cellulose-iron oxide nanoparticle composite samples BC-SiO$_2$ IO NPs-STAT, BC-SiO$_2$ IO NPs-AGIT, BC-STAR IO NPs, and BC-IO NPs (syn).

Key to symbols and abbreviations: 2nd: secondary; band intensity: s,m,w = strong, medium, weak band width b, sh = broad, sharp ; v = very

Wavenumber (W) in cm^{-1} of absorption frequency or frequency range						
BC-STAT (a) BC-AGIT (b) MC (c)	*GAB* (f) BC-STAT-*GAB* (d) BC-AGIT-*GAB* (e)	SiO$_2$IONP (g) STAR nZVI (h) IONP$_{(syn)}$ (i)	BC-SiO$_2$IONP-A outside=out inside=in	BC-IONP$_{(syn)}$	Assignment	References W (cm^{-1})range
3342/3295 b 3338/3296 a 3338/3298 c	3332/3288 e 3338/3290 d 3280 f	3342/3297 g 3362 i	3342-40/3302	3342/3302	vOH (OH stretch) Hydrogen-bonded	3600-3200[176] 3500-3200[179; 184; 194-197]
2967 a, b, c 2941 a, b, c 2901 c 2897 a 2895 b 2873 a, b, c	2973e/2959 df vCH$_3$(antisym) 2925de/2923f vCH$_2$ (antisym) 2897de v CH vCH$_3$ (sym) 2876df/2874e vCH$_3$ (sym) 2857e/2852df vCH$_2$ (sym)		2897	2930 vCH$_2$ (antisym) *** 2895 vCH$_3$ (sym) *** 2843 vCH$_2$ (sym)	vCH (CH stretching modes): vCH$_3$ (antisym) antisymmetrical vCH$_2$ (antisym) antisymmetrical, vCH vCH$_3$ (sym)symmetrical, vCH$_2$ (sym)symmetrical	BC: CH, CH$_2$ *GAB*: CH$_3$ & CH$_2$ 2990-2850[176; 204] 3100-2700[176] vCH :[174; 177; 179; 182; 195; 198-200] 2894[182; 184; 195; 201] CH: 2885[174]

Wavenumber (W) in cm^{-1} of absorption frequency or frequency range (Table 1 continued)						
1640 c 1636 a, b	obscured by Amide I	1625 1632 i	1647 out 1630 in	1641	δHOH (scissor) H$_2$O intercalation, ab/adsorption	1650[179], 1640[177]
	1649 e 1636 f 1634 d		1650	1650	vC=O Amide I secondary (2nd) amide carbonyl	1680-1630[176] 1652-1637[189; 205-207] 1650-1640[177]
	1544 e 1528 d 1527 f		1537	1534	δNH Amide II (2nd)	1565-1475[176; 204] 1550-1540[205 ; 207; 208] 1550[177]
1482 a, b 1479 c 1453 a, b, c 1428 a, b, c	1485 e 1467 d-f 1455-9 f 1453 e 1449 d 1426 e		1486 1452 1426	all indistinct 1423	δCH (CH deformation, or bending): δCH$_2$ (sym) scissor or δ CH$_2$ (sym) at C6 δCH$_3$(antisym) antisymmetric deformation	δCH$_2$ (sym): 1480-1440[176],1450[177] δCH$_2$ (sym)at C6 1430-1420[176], 1431-1419[184; 197; 210-212] 1426[196; 213], 1425[214] δCH$_3$(antisym) 1470-1440[176], 1460[177]

Wavenumber (W) in cm^{-1} of absorption frequency or frequency range (Table 1 continued)						
1369 a, c	1389 f		1370	1363	δC-H	δCH₃(sym):
1362 c	1371 d		1362		bending modes:	1380-1360, 1375±10 [177; 195]
1361 a, b	1369 e			1335		
			1335		δCH₃(sym)	δC-H :
1335 a, b, c	1343 f				symmetric deformation	1376-1373[184; 211]
	1336 e		1315	1315	***	1340[179]
1315 a, b, c	1335 d				δCH₂ (sym)	1282-1278[199; 211]
			1281	1279	symmetric bending deformation	
1281 a	1315 e				***	δCH₂ (sym) wag:
1280 c	1314 d				δCH₂ (sym)	1362, 1317[213]
	1309 f				bending wag at C6	1319-1317[211; 220], 1313[196; 213]
						1305 [177]
	1280 e					δCOH at C6:
	1278 d					1337[211; 212]
1250 a	1250 e		1250	1263	δCOH	δCOH:
1247 c	1236 e		1232	1235	in-plane at C6	1236-1228[182; 211]
1235 a , c	1233 d					
1234 b						
	1229 f				vCN (C-N stretch)	1300-1220[177]
					vCN-δNH mix [177]	1240[221]
					Amide III	

Wavenumber (W) in cm⁻¹ of absorption frequency or frequency range (Table 1 continued)						
1206 a 1202 c	1207 e 1205 d		1205	1200	δCOH in-plane at C6	δCOH: 1207-1200[182; 207]
1162 a, b, 1160 c	1163 f 1161 e 1159 d		1162	1159	vCOC (antisym) antisymmetric stretch, C1-O-C4 at glycosidic linkage	vCOC (antisym): 1170-1160[179; 189; 206; 213; 222] C1-O-C4 at 1162[197; 210; 211; 222; 223]
1109 a, b, c	1108 d, e		1109	1107	vC–O stretch at C2-O2[189; 213]	vC–O :1115-984[189; 213; 224] C2-O2[189; 213]
		1068 1346 h,i	1075 in		v Si-O stretch	v Si-O : 1110-1068[179; 219]
1057 a, b, c 1034 a, b, c	1061 f 1057 d 1056 e 1034 d, e		1057 1034	1056 1027	vC–O stretching vC–O stretch at C3–O3H vC–O stretch at C6-H₂-O6	vC–O :1061-1057 C3–O3H[189; 213] vC O (sym) 1040[179] vC–O : 1040[179],1035,1032,1030[213], 1015,1000 C6-H₂-O6H[189; 213; 224] C-O stretching at 984 [196,224]
		No peak, just bulge on side				Si-OH stretching at 949 [179] need peak fitting

					Wavenumber (W) in cm^{-1} of absorption frequency or frequency range (Table 1 continued)	
				899	δ Fe-O-H	899[178] magnetite[215]
898 a 896 c			893		vCOC(antisym) antisymmetric stretch at glycosidic link δC1-H	vCOC at the β-(1,4)-glycosidic linkage[197,210,211,223]
				799	δ Fe-O-H	799[178]
		793	796 in		v Si-O (sym) v Si-O-Si (sym)	v Si-O (sym): 800-780 [219] v Si-O-Si: 804 [179]
746 a,b,c	746 d 745 f 742 e				δCOH bending	δCOH: 713[211,212]
				632	vFe-O or vFe-O-Fe stretching magnetite & maghemites NPs tetrahedral Fe atoms.	600-500[177;187;215-218] Fe-O [225] 590
699 a 697 b,c	699 f 697 d 696 e		696	696	δCOH out of plane Cellulose Iβ	δCOH[201; 226]
664 b 663 a,c	668 d 666 f 664 e		663	664	δCOH out of plane	δCOH[184]